Synthesis and Aptamer-Targeted Nanoparticle Delivery of Ruthenium(III) Theranostics

by

Saeid Farzaneh

B.Sc., Simon Fraser University, 2020

Thesis Submitted in Partial Fulfillment of the
Requirements for the Degree of
Master of Science

in the
Department of Chemistry
Faculty of Science

SIMON FRASER UNIVERSITY
Spring 2024

Declaration of Committee

Name:	**Saeid Farzaneh**
Degree:	**Master of Science (Chemistry)**
Title:	**Synthesis and Aptamer-Targeted Nanoparticle Delivery of Ruthenium(III) Theranostics**
Committee:	**Chair:** **Paul Li** Professor, Chemistry
	Charles J. Walsby Supervisor Associate Professor, Chemistry
	Jeffrey J. Warren Committee Member Associate Professor, Chemistry
	Byron D. Gates Committee Member Professor, Chemistry
	Caterina Ramogida Examiner Assistant Professor, Chemistry

Abstract

Two novel fluorescent analog of the Ru(III) compound, **NAMI**, were synthesized and characterized. Chapter 2 explored the effects of functionalization using lipophilic trifluoromethyl groups. This significantly increased the lipophilicity, cellular uptake, and *in-vitro* activity of the ruthenium complex, suggesting its potential as a potent anticancer agent. Aqueous ligand-exchange behaviour of the ruthenium complexes determined that the dissociation of a chloride ligand is favored to form active mono-aquo species. In chapter 3, nanoencapsulation of the **NAMI** analogs in aptamer-functionalized PLGA-PEG nanoparticles, showed promising results in enhancing drug transport into cells. The drug release behaviour of the nanoparticles revealed the existence of a burst-release phase, followed by a gradual and sustained leaching of drugs out of the nanoparticles. Despite achieving negligible cytotoxicity with nanoencapsulation, higher intracellular ruthenium content was observed. This work highlights the potential of nanoencapsulation strategies for improving the efficacy of ruthenium-based chemotherapeutics.

Keywords: Ru(III) anticancer compounds; PLGA-PEG nanoparticles; AS1411 aptamer; Cell uptake

To Mom, Dad and Amirali

تقدیم به مادر و پدر عزیزم که بدون حمایت آنها هیچ چیزی ممکن نبود

Acknowledgements

The completion of this thesis would not have been possible without the support I received from my supervisor, peers, friends, family, and faculty members. I'd like to thank Dr. Charles Walsby. First, thank you for giving me the opportunity to join the group as an undergrad which stoked my interest in medicinal chemistry and passion for research. Second, I want to thank you for the endless guidance and support you've provided me inside and outside of the lab, whether it was with the MSc research or my school applications. I want to thank Dr. Jeffrey Warren for providing me with research advice, helping me with the purchase of the aptamers and providing me access to instruments, and the support you showed me with my school applications. I also want to show my gratitude to Dr. Byron Gates for their helpful advice and for providing me access to particle analyzer which without, the analysis of my nanoparticles would have been virtually impossible. I also want to thank Devon Heroux at the BC cancer Institute in Dr. Marcel Bally's lab for their continued help with the in-vitro experiments. Without Devon's contributions, I wouldn't have been able to extract such impactful data for this thesis. I also want to thank Melissa Radford from the Gates group for taking time to train me on their particle analyzer, and I want to thank Leanna Karn from the Leznoff group for helping me with quantum yield measurements. Lastly, I'd like to thank Dr. Young and his group for providing me access to their mass spectrometer and lyophilizer.

I was fortunate to meet a lot of wonderful people during my time at SFU that made navigating the difficulties of graduate research bearable. I want to start by thanking Shane Harrypersad who mentored me when I first joined the Walsby group as an undergraduate volunteer. Shane laid down a lot of the groundwork for the research skills I currently have. Thank you, Shane, for always taking the initiative in the group and planning the events and outings, and always being so supportive. To Greg MacNeil, thank you for helping me not spiral into madness when my research wasn't working. Those morning coffee rants really saved me. Without your help and support, delving into nanoparticle and ruthenium chemistry would have been a lot more complicated than it needed to be. Thank you for always answering my endless questions with patience and keeping things entertaining with your dad jokes. To my good friend and lab mate Aryan Houshmand, thank you for always being so supportive inside and outside of the lab. Thanks for always keeping my ego in check and giving me reality checks when I needed

them. Looking forward to all the mountain biking and skiing adventures we'll have in the future. To Adrian and Steph, thank you for always being such great friends and always hosting me in Victoria whenever I needed to get away from the mainland and needed a break from research. To Hannah Cavanagh, thank you for being a ray of sunshine and putting up with my perpetual complaining and always making me see things through a positive lens when things were difficult. To one of my oldest friends at SFU and one of the first friends I made as an undergrad, Ana Sonea, thank you for agreeing to be my friend when I was a quiet kid in the first-year chemistry tutorial; I'm proud of how far we've both come! To Garrett Muir, thank you for always being so easy to talk to and always breaking it down to the best of your ability on the dance floor at the Cambie. To the Buckyball FC lads, Baset Hakimi, Alan Brooke, Callum Lucas, Habib Dbouk, Omar Castro-Sandoval, Kalvin Kwan, Tyler Govett, Ethan Fung, and Adam Avdic, thank you for the endless memories and entertainment on the pitch at the intramurals and finally clinching the championship. Sorry for all the red cards I received. Finally, a special thank you to the Chemistry Graduate Caucus and all the members I got to work with during my tenure.

None of the work presented in this thesis would have been remotely possible without the consistent support and backing of my family. Mom and Dad, thank you for sacrificing so much and leaving everything behind in Iran to make sure I get the best possible opportunities and education. Without your selfless actions, consistent love and support I wouldn't be where I am in life. Thank you for being such good role models to make me the person that I am today. Last but certainly not least, to my brother Amirali, thank you for always being so supportive and available whenever I needed help regardless of how much we argue and disagree.

Table of Contents

List of Tables

List of Figures

List of Acronyms

$CDCl_3$	d^6-Chloroform
CF_3	Trifluoromethyl
CI	Combination Index
CNS	Central Nervous System
DCC	N,N'-Dicyclohexylcarbodiimide
DCM	Dichloromethane
DIEA	N,N-Diisopropyl Ethylamine
DL	Drug Loading
DLS	Dynamic Light Scattering
DNA	Deoxyribonucleic Acid
DMED	Dulbecco's Modified Eagle Medium
DMF	Dimethylformamide
DMSO	Dimethyl Sulfoxide
DSC	Dansyl Chloride
EDC	1-Ethyl-3-(3-dimethylaminopropyl) carbodiimide
EE	Encapsulation Efficiency
EPR	Electron Paramagnetic Resonance
EPR	Enhanced Permeability and Retention
FDA	Food and Drug Administration Agency
HAS	Human Serum Albumin
IC	Inhibitory Concentration
ICP-MS	Inductively Coupled Plasma Mass Spectrometry
KED	Kinetic Energy Discrimination
LC	Liquid Chromatography
LCMT	Ligand Metal Charge Transfer
MS	Mass Spectrometry
MTT	3-(4,5-dimethylthiazol-2-yl)-2,5-diphenyltetrazolium bromide
NCL	Nucleolin
NHS	N-Hydroxy Succinimide
NM	Nanomaterial
NMR	Nuclear Magnetic Resonance
NP	Nanoparticle

NS-APT	Non-Specific Aptamer
PARP	Poly-(ADP-Ribose) Polymerase
PB	Phosphate Buffer
PBS	Phosphate Buffered Saline
PDI	Polydispersity Index
PEG	Polyethylene Glycol
PLGA	Poly Lactic-co-Glycolic Acid
PTA	1,3,5-Triaza-7-phosphaadamantane
PTFE	Polytetrafluoroethylene
Pyr	Pyridine
QY	Quantum Yield
RAED	Ruthenium Arene Ethylenediamine
RAPTA	Ruthenium Arene PTA
RM	Recovered Mass
RNA	Ribonucleic Acid
ROS	Reactive Oxygen Species
SOC	Standard Of Care
SSB	Single-strand Breaks
ToF	Time of Flight

Chapter 1. Introduction

1.1. Metals in Modern Medicine

Metal ions play central roles in many biological processes and have also found applications as novel therapeutics.[1] Research in inorganic medicinal chemistry has revealed the huge potential of metal complexes in medicinal applications, with a broad spectrum of approaches developed for novel diagnostics and therapeutic agents. These include examples such as technetium-based metallodrugs for radio-imaging, platinum-containing chemotherapeutics and bismuth compounds as over-the-counter gastrointestinal medicine (**Figure 1.1**).[2,3] Compared to conventional organic drugs design, utilizing metal-centers provides benefits such as: (i) providing flexibility in geometry with facile access to 3D structures, (ii) redox activity in biological environments, (iii) optimization of activity through ligand choice and design, and (iv) potential for ligand-exchange processes that modulate biological acitivity.[4,5]

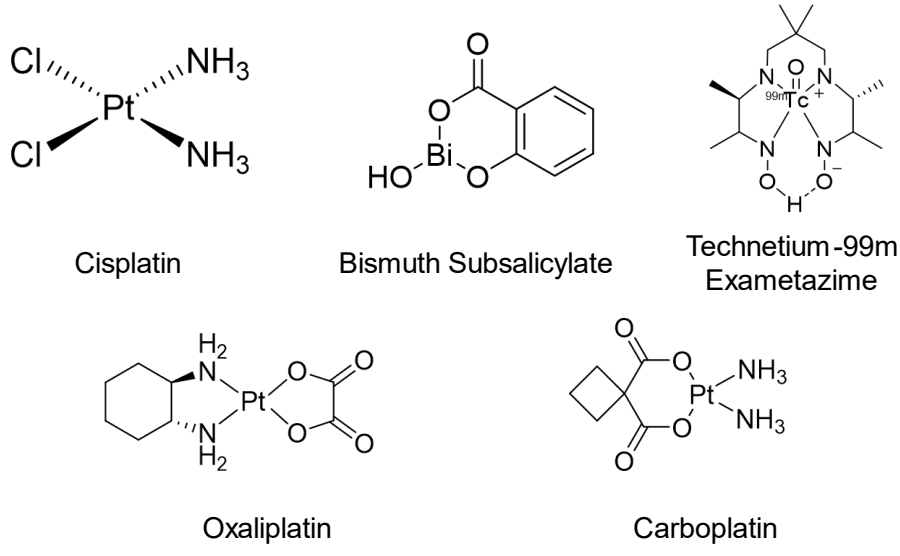

Cisplatin | Bismuth Subsalicylate | Technetium-99m Exametazime

Oxaliplatin | Carboplatin

Figure 1.1. Clinically approved inorganic pharmaceuticals.

Metal complexes are a major area of interest in the development of chemotherapeutic candidates.[2,6–10] A variety of different approaches have been applied to the design of these compounds to target specific pathways for anticancer activity. One

particularly promising method is the incorporation of biologically active molecules into the complex via functionalized ligands.[11,12] The target of these compounds include cellular proteins, membrane receptors, and DNA.[4] These biomolecules possess binding sites that can be targeted by functionalized metal-complexes, allowing the promotion or inhibition of downstream processes that result in therapeutic effects.[1] In some cases, this generates novel compounds where the metal-centre and the biological ligand both play a role in binding to or perturbing a biomolecule system.[13] An alternative approach relies on ligand-exchange, following cellular transport, to release a reactive metal species from a biological chaperone. Moreover, ligand exchange processes can generate more labile metal species, promoting interactions with biological targets.[13] Such ligand-exchange processes can be fine-tuned through the choice of metal center and ligands design.[4]

The redox activity of many metallodrugs has been implicated in their mechanism of action, particularly as a pathway to toxic reactive Oxygen species (ROS).[12,14,15] This activity is usually centered at the metal ion, and can provide additional activity to ligand moieties, helping to address development of drug resistance, which is prevalent and can be detrimental to many chemotherapies.[12,16–18] This is an issue for Tamoxifen which is widely used for the treatment for advanced breast cancer since its introduction to the market in the late 1970's.[19] Although Tamoxifen is very effective in the selective targeting of breast cancer cells, the prolonged use of the drug is associated with drug-resistance development through a variety of mechanisms.[20]

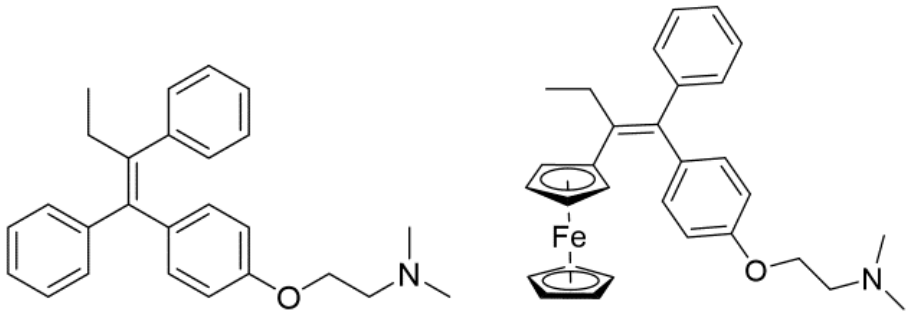

Tamoxifen Ferrocifen

Figure 1.2. Molecular structures of Tamoxifen and Ferrocifen.

A new class of organometallic compounds were introduced in the late 1980's through the incorporation of metallocene functionalities to the Tamoxifen scaffold, leading to the discovery of a Ferrocene-containing analogue, "Ferrocifen" (**Figure 1.2**).[12,21] The introduction of the ferrocene moiety to the Tamoxifen scaffold, resulted in increased antiproliferative and cytotoxic properties of the overall molecule against breast cancer cells.[11,12,14] This increased activity has been correlated to the redox activity of ferrocene, which allows for the reversible oxidation of its Fe(II) centre to Fe(III) in the physiological environment of tumor tissue. This potentially causes cell death or apoptosis through a multitude of biological mechanisms such as the generation of ROS.[12] Moreover, the synergy between the tamoxifen backbone and the ferrocene moiety potentially provides dual modes of anticancer activity, reducing the potential for acquired resistance, and can overcome drug-resistant tumors.

Since the serendipitous discovery of its antiproliferative properties in the 1960's, cisplatin has become the cornerstone of chemotherapeutics in modern day medicine.[22–24] The success of cisplatin and other platinum-based anti-cancer compounds is highlighted by their extensive use in the treatment of numerous common forms of cancer including lung, bladder, cervical, testicular, hepatic cancers, and leukemia.[6] Cisplatin is a square planar platinum (II) coordination complex that is activated by ligand-exchange processes in specific physiological environments.[2,6,25] This activation is dependent on physiological chloride concentration.[26] For instance, in the bloodstream and other extracellular tissue, the concentration of chloride is much higher (~150 mM) than in the cell (5-50 mM), hence the loss of chloride ligands and activation is uncommon.[26] However, upon cell entry cisplatin undergoes rapid ligand-exchange, one or both chloride ligands are lost and replaced by water molecules.[2] Hydrolyzed cisplatin is a potent nucleophile and will actively react with DNA and intracellular proteins, covalently binding to the N_7 site on purine bases (**Figure 1.3**).[2,26] This interaction causes irreversible DNA damage, leading to DNA lesions that interrupt DNA replication and transcription, ultimately leading to apoptosis.[2,6,26]

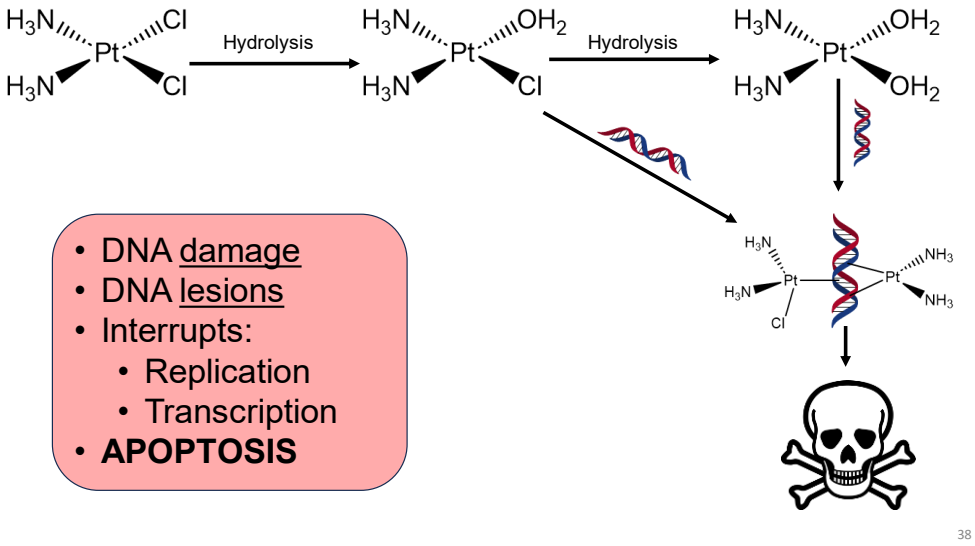

Figure 1.3. The most commonly depicted mechanisms of action of Cisplatin.[4]

Although cisplatin and other platinum-based chemotherapeutics are effective at causing cell-death in cancer tissue, it would be unwise to ignore the drawbacks associated with their use. Platinum-based anticancer agents are highly toxic and seldom selective in their mode of action; hence they cause cell death indiscriminately, affecting both cancerous and non-cancerous cells. In addition, studies show that healthy rapidly growing cells such as gastrointestinal, hair and, bone marrow are especially affected by this off-target activity.[2,25] Moreover, treatment with these pharmaceuticals is often dose-limited by their side-effects such as kidney damage, permanent hearing/balance loss, and severe nausea.[6,26] The development of drug resistance by tumor cells is a significant challenge in the application of platinum-based chemotherapeutics.[2,6] For instance, 10-15% of ovarian cancer patients receiving cisplatin experience relapse and develop chemoresistance, resulting in poor prognoses and survival rates less than a year.[27] While new strategies to overcome the issues related to side-effects and acquired resistance for Pt complexes are continuously evolving, a very promising approach is to explore alternative metal ions. Consequently, a multitude of other potential metal-containing anticancer agents containing gold, copper, gallium, titanium, osmium, rhenium, iridium, ruthenium, and many other metals have been examined in both clinical and preclinical development.[28–37]

1.2. Ruthenium Anticancer/Antimetastatic Agents

Ruthenium (Ru) complexes have become one of the leading candidates as an alternative to the traditional platinum anticancer agents.[38] Both Ru(II) and Ru(III) compounds have been studied extensively, with many exhibiting antiproliferative and antimetastatic properties.[4] Ruthenium anticancer agents frequently exhibit lower cytotoxicity than Pt compounds and are less prone to off-target activity, making them appealing as chemotherapeutics.[38] In physiological conditions, ruthenium exhibits similar water exchange rates as platinum, ranging from 10^{-3} s^{-1} to 10^{-2} s^{-1}, which falls within the time frame of cell division.[39,40] However, it should be noted that these exchange rates can differ significantly depending on the ligands attached to the metal center.[4] In addition, Ru (II) agents are typically found to be more reactive and undergo ligand-exchange processes more rapidly than Ru (III) agents, suggesting the use of Ru (III) compounds as prodrugs that are activated upon reduction in hypoxic (low oxygen) tissues found in many tumors.[39] Consequently, some ruthenium anticancer agents have also shown selectivity towards cancerous cells.[37–39,41] Furthermore, some research suggests that ruthenium can mimic iron in biological systems and interact with blood plasma proteins such as albumin and transferrin which can help facilitate their transport into tumor tissue.[39,42] However, these studies have been heavily debated. Both Ru(II) and Ru(III) anticancer agents typically exhibit distorted octahedral geometries that can accommodate up to six coordinated ligands, allowing for the modulation of steric and electronic properties of the overall complex through ligand choice.[39] In addition, this allows for the fine tuning of properties such as aqueous solubility, cytotoxic activity, and interactions with biomolecules. Interestingly, ruthenium-based chemotherapeutics exhibit a variety of mechanisms of anticancer activity, and as a result may be more effective against acquired resistance.[43]

Initially, it was proposed that the primary mechanism of ruthenium chemotherapeutics involved direct DNA interactions.[44] However, more recent studies have implicated multiple mechanisms of action are responsible for the cytotoxicity of these compounds.[45] These include: interactions with cellular proteins and cell adhesion proteins, and the generation of ROS that disrupt the cellular redox balance.[44–50] These mechanisms collectively can instigate apoptosis.[45,49] Furthermore, the selective activation of Ru anticancer complexes, has been linked to “activation by reduction”,

where Ru(III) complexes are converted to more labile Ru(II) species *in-vivo*.[46] Literature reported reduction potential values of Ru(III) NAMI-A and KP1019 are -0.220 V and -0.720 V versus normal hydrogen electrode (NHE), respectively.[51]

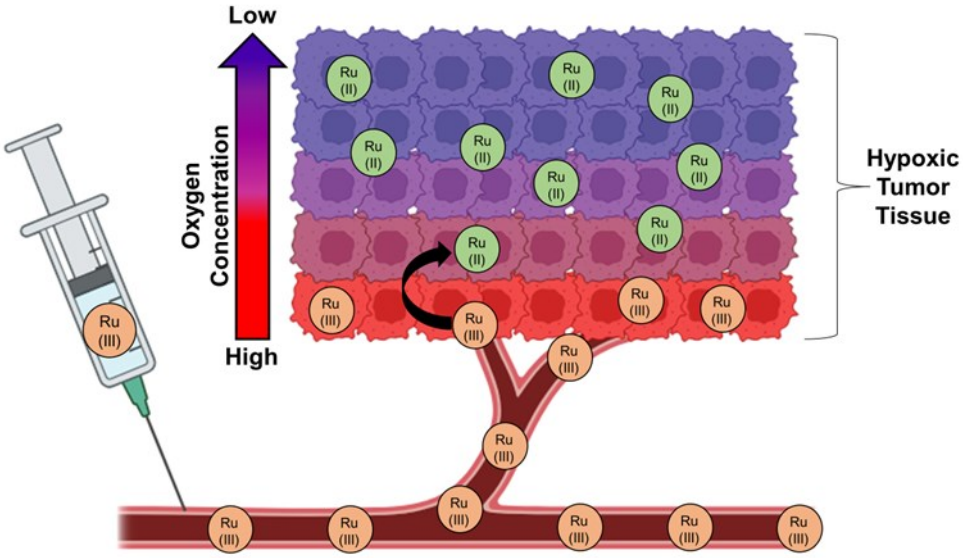

Figure 1.4. Activation of Ru (III) agents in the reducing environment of tumor tissue through reduction to Ru (II).

A common characteristic of most tumour tissues is hypoxia, which refers to a low concentration of oxygen. Due to the rapid proliferation of cancer cells and intensive growth of tumor tissue, cellular oxygen demands can exceed the supply from nearby blood vessels.[52] Furthermore, as a tumor grows, the distance between nearby blood vessels and the tumor cells increases, which severely impedes the diffusion of oxygen to these tissues.[52] Reduced oxygen concentrations induce cancer cells to switch to anaerobic respiration, producing lactic acid as a by-product.[52] This, in turn, lowers the pH in tumor tissues. In addition, the lower oxygen concentrations lead to an increased presence of the highly reducing compound glutathione (GSH).[44] The oxygen poor, reducing, and acidic physiological environment potentially allows for the reduction of the relatively inert Ru(III) species to the more labile Ru(II) species.[52] Moreover, the reduction of Ru(III) species to the active Ru(II) species potentially enables the selective targeting of malignant tissues.[46] Therefore, Ru(II) species can accumulate selectively in tumor tissue and take their therapeutic effect in the unique physiological environment of these tissue (**Figure 1.4**). The many different possible modes of anticancer activity for Ru

compounds also suggest they will be less susceptible to acquired resistance, providing another benefit over traditional platinum chemotherapeutics.

1.2.1. Ruthenium(II) Chemotherapeutics

The first Ru(II)-arene complexes were investigated by Zelonka *et al.* in early 1970's for their potential catalytic properties.[53] In the early 1990's Tocher *et al.* determined that antibiotic and cytotoxic activity in these compounds was achievable through the coordination of metronidazole, a known antibiotic, to the Ru(II)-arene scaffold.[54] This discovery, kickstarted the investigation of Ru(II)-arene "piano-stool" or "half-sandwich" complexes as potential anticancer and antimetastatic agents. Through the work of Dyson and coworkers, a new family of monodentate pseudo-octahedral Ru (II)-arene complexes with the general formula $[(\eta^6\text{-arene})RuCl_2(PTA)]$, **RAPTA** (Ruthenium Arene PTA), were developed.[55,56] This new class of compounds consisted of a Ru (II) metal center attached to an η^6-arene ring, and three monodentate ligands, usually consisting of two halide atoms and an amphiphilic PTA ligand (PTA = 1,3,5-triaza-7-phosphaadamantane) (**Figure 1.5**).

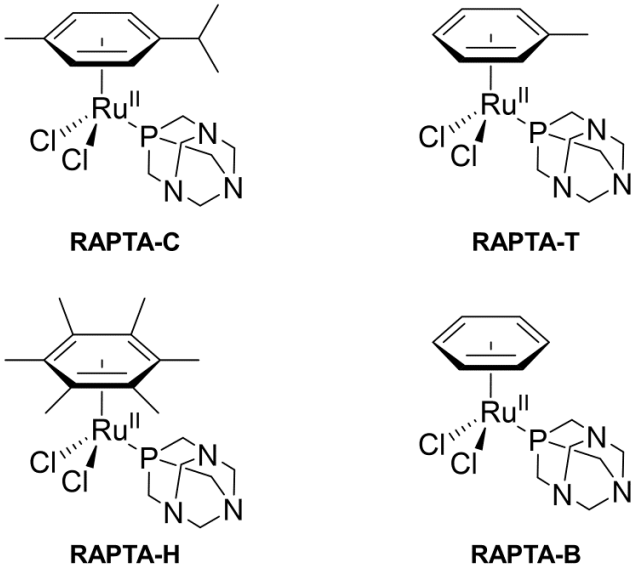

Figure 1.5. The chemical structures of RAPTA-type compounds.

The organic arene ring stabilizes Ru(II) oxidation state, and can be modified to alter the overall lipophilicity of the complex, in which modulates cellular uptake.[57] Additionally the arene ring can be decorated with biologically-active groups or targeting molecules.[39,43,55] The monodentate halide ligands generally behave as leaving groups through exchange processes (similar to that of cisplatin). The choice of these ligands can influence the water-exchange rates and cellular uptake, and consequently the reactivity of the complex.[55] Finally, the monodentate PTA ligand plays a role in uptake and water solubility of the complex[58]. It was found that the modification of the arene group with hydrophilic hydrogen bonding substituents led to decreased activity towards cancer cells, which was attributed to decreased cellular uptake.[55] Conversely, the modification of the arene ring with bulky hydrophobic groups increased cytotoxicity but lowered selectivity towards cancer cells when compared to **RAPTA-C** (the parent compound with p-cymene ring).[55] To introduce cytotoxicity to **RAPTA** complexes, various studies were conducted through the modification of the chloride ligands with other halogens, the modification of the PTA ligand and the arene ring however, no significant improvements in cytotoxic activity were achieved.[55–57,59] **RAPTA** complexes were found to take their physiological effects through interactions with cellular proteins that are responsible for maintaining the redox balance of the cell such as glutathione transferase, lysosomes, cathepsin B, and TrxR.[58] Some studies suggest that Ru(II)-arene complexes can interact with DNA through direct intercalation of the planar arene ligand between the major and minor grooves of the DNA.[4]

Dyson and coworkers tested **RAPTA-T** and **RAPTA-C** against the TS/A metastatic mouse adenocarcinoma cell line and found that the complexes exhibit mild cytotoxicity (IC_{50} >300 μM).[59] Although both compounds were inactive against primary cancer cells, they were effective at reducing lung cancer metastasis.[59] These findings established **RAPTA** complexes as a viable candidate as potential antimetastatic agents. Another prominent class of Ru(II)-arene complexes, **RAED** (Ruthenium Arene Ethylenediamine), were developed by Sadler and coworkers through the utilization of bidentate chelating ligands such as ethylenediamine (**Figure 1.6**). The effects of modification of the halide ligand, chelating ligand, and the arene ring on the overall cytotoxicity of the complex against A2780 cell line (human ovarian cancer) were studied and some complexes showed notable activity.[60] Among these complexes were the benzene analog of **RAED** (**Figure 1.6, 2**) which showed a 17 μM IC_{50} (one order of

magnitude less than cisplatin, IC_{50} of 0.5 μM) and the biphenyl analog of **RAED** (**Figure 1.6, 3**) which showed a similar IC_{50} to carboplatin (6 μM).[60] In addition to the similar activity of these complexes to platinum-based anticancer agents, **RAED** compounds were also found to form adducts with N_7 site of guanine residues.[61]

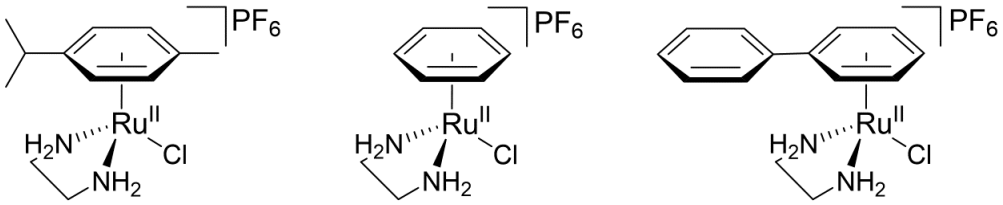

1. RAED-C **2. RAED-B** **3. RAED-BP**

Figure 1.6. The chemical structures of RAED family of Ru(II) complexes.

1.2.2. Ruthenium(III) Chemotherapeutics

Ruthenium(III) complexes are another family of promising alternatives to the platinum anticancer agents which currently dominate the field of metal-based chemotherapeutics. The development of Ru(III) anticancer agents was largely initiated in early 1980s by Durig and coworkers who explored the growth inhibiting properties of Ru(III) chloroamine complexes like *cis*-[$Ru^{III}Cl_3(NH_3)_3$] against *E. coli*.[62,63] Although these compounds showed promise initially, they were unsuitable for clinical studies due to their poor aqueous solubility.[38] A major breakthrough came in the late 1980's when the Keppler group established the anti-tumoral activity of **KP418**, a Ru(III) trans-*bis*-imidazole compound with four axial chloride ligands.[50] The anticancer activity of **KP418** was comparable to cisplatin and it was found to be effective at the growth-inhibition of colorectal adenocarcinoma in rats.[50] **KP418** was found to have a poor overall toxicity profile in mouse models and the focus was shifted to examine it's indazole containing analog.[48] Following the studies of **KP418**, two Ru(III) compounds, **NAMI-A** and **KP1019** and their analogs (**Figure 1.7**), gained significant attention due to their success in preclinical studies.[47,49] Moreover, **NAMI-A** (imidazolium *trans*-[tetrachloro (dimethylsulfoxi- de) (1H-imidazole) ruthenate (III)]) and **KP1019** (indazolium *trans*-

[tetrachlorobis (1H-indazole) ruthenate (III)]) have been investigated as promising chemotherapeutics in clinical trials.[64,65]

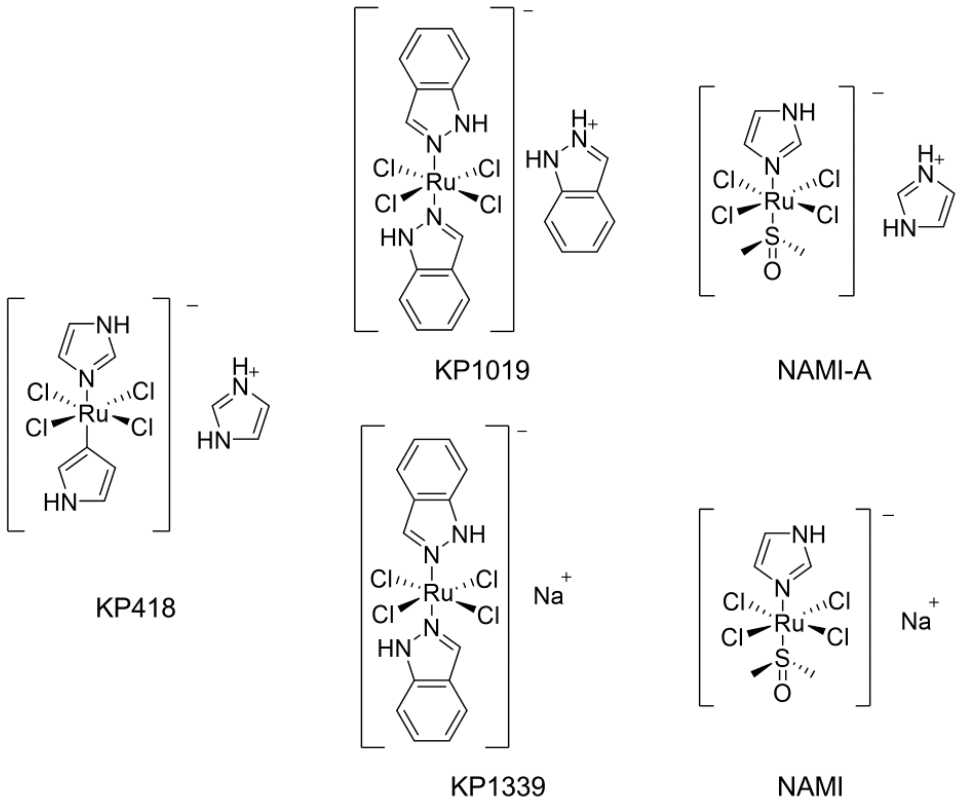

Figure 1.7. Chemical structures of Ru(III) anticancer/antimetastatic agents.

NAMI-A, **KP1019**, and their sodium compensated analogs (**NAMI** and **KP1339**) (**Figure 1.7**) have well established and facile synthetic procedures, acceptable solubility in aqueous media, and exhibit stability in the solid state.[49] Despite their structural similarities, **NAMI-A** and **KP1019** show different properties *in-vitro* and *in-vivo*.[39] Both **NAMI-A** and **KP1019** exhibit DNA binding abilities, although their mechanisms of action differ from cisplatin. **NAMI-A** demonstrates faster binding rates than cisplatin and **KP1019**, thanks to its higher kinetic reactivity in aqueous media.[44] It can form interstrand adducts that disrupt DNA processes, whereas **KP1019**'s capability to form these adducts is comparatively lower. Notably, the DNA damage and cytotoxic activity induced by these drugs are found to be less than that caused by cisplatin due to the smaller conformational changes they induce.[44] This can be deemed advantageous, as the

reduced cytotoxicity of these drugs has the potential to lead to fewer dose-limiting side effects. Although both compounds have the capability to create adducts with DNA, **NAMI-A** exhibits faster binding rates when compared to cisplatin due to its rapid water-exchange behaviour, while KP1019 shows slightly slower DNA binding rates than cisplatin.[49] Despite its stability in the solid state, **NAMI-A** undergoes rapid stepwise water-exchange in media. The process involves the pH dependent dissociation of the chloro ligands, or the loss of the axial DMSO ligand.[44] Similarly, **KP1019** undergoes dissociation of chloro ligands with water to give aqua or hydroxo groups.[47]

The development of **KP1019** (**Figure 1.7**), the indazole analog of **KP418**, marked a significant advancement in ruthenium cancer research. The introduction of indazole ligands led to a remarkable ten-fold improvement in the complex's cellular uptake as compared to the imidazole complex.[38] This was linked to the influence of the axial ligands on the complex's interactions with blood plasma proteins such as Human Serum Albumin (HSA) and transferrin.[38] The uptake of **KP1019** via serum proteins is mediated by transferrin receptors, leading to cellular internalization via endosomes and its intracellular release.[38] Moreover, It's hypothesized that this process leads to the subsequent release of the complex within the cell, facilitated by the lower pH environment within the endosomes.[38] Initial studies indicated **KP1019**'s activity against a variety of cell lines, notably, colorectal carcinomas.[50] Preclinical studies investigating the *in-vivo* properties of **KP1019** also had promising results. Treatment of mouse models with chemically induced colon cancer using **KP1019** resulted in an impressive 95% reduction in tumor size without inducing any mortality.[66] These results marked **KP1019** as a superior anticancer agent compared to 5-fluorouracil, which was the standard anticancer agent for colon cancer treatment at the time.[38] This paved the way for further investigations into the potential of **KP1019** in preclinical studies. While **KP1019**'s activity justified further investigation in clinical trials, limitations in aqueous solubility hindered its progression. However, **KP1339**, the sodium salt analog of **KP1019**, exhibited promising water-solubility, along with comparable cellular uptake and antiproliferative properties.[66] Consequently, it has emerged as the leading ruthenium-based anticancer agent currently under investigation in phase-IIb clinical trials by BOLD Therapeutics under the name **BOLD-100**.[67,68]

In contrast to **KP1019**, *in-vitro* screening of **NAMI-A** demonstrated low cytotoxic activity against a variety of cell lines at biologically relevant concentrations, with 1000

times lower cytotoxicity than cisplatin.[44,49,50] In contrast, cell growth inhibition properties were demonstrated against certain leukemia cell lines even at extremely low concentrations.[44] However, the general lack of activity has been attributed to **NAMI-A**'s rapid transformation in the extracellular matrix, enabling interactions with extracellular components and serum proteins, and the prevention of its internalization by cancer cells.[49] While **NAMI-A** may not have exhibited direct inhibitory activity against cancer cells, this did not diminish its potential as a viable chemotherapeutic.[46] At lower physiologically relevant concentrations (1-10μM), **NAMI-A** displayed notable antimetastatic properties towards primary tumors.[69] Preclinical studies revealed that **NAMI-A** interacts with the components of the extracellular matrix such as cell-adhesion proteins.[44] These interactions result in reduced cell motility and increased cell adhesion, effectively preventing the detachment of cells from primary tumors and metastasis.[49] Additionally, **NAMI-A** proved effective in inhibiting the growth and migration of endothelial cells which is a crucial factor in impeding angiogenesis and the spread of cancer.[49] While the antiproliferative and antimetastatic properties of **KP1019, NAMI-A**, and their analogs are well established in literature, their exact mechanism of action remains an ongoing area of investigation.

1.3. Nanomaterials and their applications

The field of nanotechnology is rapidly advancing with applications across various industries including electronics, agriculture, energy, and medicine.[70] In electronics, nanotechnology allows for the manufacturing of more energy-efficient devices. In agriculture, it aids in maximizing crop yields and improving energy efficiency.[70] Moreover, the utilization of nanomaterials (NMs) in the energy sector has allowed for the manufacturing of more efficient energy storage devices.[70] Notably, nanoparticles have revolutionized the field of medicine by enabling the targeted delivery of pharmaceuticals.[71] The first reported synthesis of nanoparticles occurred in 1857 when Michael Faraday synthesized a colloidal gold NP solution.[72]

Today, nanotechnology is regarded as one of the most promising areas of research, driven by the versatility of nanomaterials with tunable characteristics like electrical and thermal conductivity, melting point, light absorption, and hydrophilicity.[72] This technological versatility highlights nanotechnology's crucial role in advancing various industries. Nanomaterials can be broadly categorized into four groups (**Figure**

1.8): carbon-based NMs like carbon nanotubes, inorganic NMs such as gold or silver nanoparticles, organic NMs including liposomes and polymeric nanoparticles, and composite NMs formed by combining two or more distinct types of nanomaterials.[72] Moreover, nanomaterials are a fascinating and rapidly developing area of interest in medicine. The utilization of nanoparticles in medicine has the potential to revolutionize diagnostics, drug delivery, vaccines, and therapeutic approaches.[73] For example, nanoparticles are employed in clinical practice for *in-vivo* optical imaging and MRI to enhance the contrast of images of lymph nodes, liver, and bone marrow, and to aid in detection of cancer.[74,75]

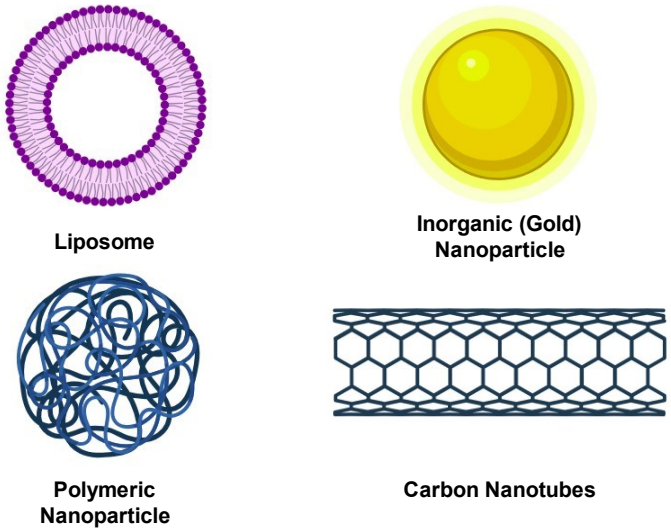

Figure 1.8. The most notable categories of nanoparticles used in modern application.

1.3.1. Nanoparticles as Drug Delivery Vehicles

Initially conceptualized by Dr. Richard Feynman in the late 1950's, nanotechnology has influenced the field of medicine and how diseases are treated.[76] For example, researchers have utilized nanomaterial in the delivery of anticancer agents to cancer cells or to treat cardiovascular complications through engaging in blood vessel repair by behaving as artificial platelets.[73] One of the most common applications of NMs in medicine is their use as drug delivery vessels to deliver pharmaceuticals to specific cells or tissues throughout the body.[73] The use of nanoparticles for drug delivery is

reported extensively in literature. In immunology, lipid nanoparticles and liposomes serve as effective carriers for delivering antibodies, either inside or on the surface of the nanoparticles.[71] In HIV/AIDS therapy, polymeric nanoparticles are utilized to solubilize drugs that are otherwise water-insoluble, enhancing their efficacy.[77] In the treatment of respiratory diseases, nanoparticles are employed to lower the inflammatory response in the respiratory tract.[78] Furthermore, in cancer therapy, polymeric nanoparticles and liposomes are used for a variety of reasons such as targeted drug delivery through surface modification, improving solubility of drugs, and extending drug release time *in-vivo*.[18,79,80] The use of nanoparticles can help address the most significant challenges in pharmaceutical drug delivery, specifically poor pharmacokinetics, bioavailability, and inadequate aqueous solubility.[70] These are all factors limiting the absorption and retention of drugs within the relevant target tissue resulting in a lower therapeutic response.[70]

As outlined above, drug delivery using nanoparticles offers significant advantages. The surface of nanoparticles can be decorated with antibodies, or short chain peptides called 'aptamers', allowing for targeting of specific cell surface receptors or organelles and enabling selective drug delivery.[81,82] Structural modifications of nanoparticles allow for controlled drug release based on the nanoparticle's breakdown rate, enabling a controlled release of the drug within the target tissue, thus allowing for prolonged therapeutic effects.[83,84] Furthermore, nanoparticles can be used with kinetically unstable and labile pharmaceuticals that can prematurely activate in non-diseased tissues, leading to reduced therapeutic effects, lower absorption, poor pharmacokinetics, and unwanted side effects. Nanoparticle encapsulation of such drugs can overcome this issue by providing a 'protective shell' that can breakdown to release the payload in the desire tissue. The effectiveness of nanoparticle encapsulation of chemotherapeutics can be increased by the Enhanced Permeability and Retention (EPR) effect which describes the tendency of macromolecules and particles in the size range of 10-300 nm to accumulate in tumors due to the leaky vasculature and poor lymphatic drainage associated with these tissues.[85]

1.3.2. NP's and Metal-based Chemotherapeutics

The first reported use of nanomaterials in the delivery of metal-based anticancer agents was the work of Matsumura and co-workers using micelle encapsulation of

cisplatin.[86] A major limitation to the clinical use of cisplatin is the dose-limiting side effects such as nephrotoxicity and neurotoxicity.[86] In an effort to overcome this challenge, Matsumura and colleagues used polymeric micelles to encapsulate cisplatin and tested the *in-vivo* release profile of the drug, antitumoral activity, and the associated reduction of nephrotoxicity in rat models.[86] Studies comparing the intravenous administration of free cisplatin versus its nanoparticle delivery revealed that the tissue concentration of platinum in the kidneys was reduced by 3.1-fold when the drug was encapsulated in micelles.[86] On the other hand, the use of NPs increased the accumulation of platinum in the liver and the spleen by 4.6- and 24.4 fold respectively, indicating alternate metabolism of the encapsulated drug.[86] In addition, the NP encapsulated drug resulted in an increase in the blood circulation time of the drug, allowing for a prolonged therapeutic effect. However, no major differences in tumor volume reduction was observed between the groups administered free complex versus the groups administered NP encapsulated cisplatin.[86]

The *in-vivo* properties of **PLGA-PEG** NPs containing another platinum based chemotherapeutic, mitaplatin, and its effects on the biodistribution of the drug in rat models was investigated by the Lippard group.[87] It was found that in the first 30 minutes after the administration of free mitaplatin, approximately 85% of the injected drug was removed from the bloodstream. Conversely, only 33% of the administered mitaplatin was removed from circulation when the drug was encapsulated in NPs.[87] Similar to the findings of Matsumura *et al*., no significant improvement in tumor size reduction was observed from the nanoencapsulation of the drug.[87] However, the biodistribution of the drug was shifted, resulting in the accumulation of platinum in the liver rather than the kidneys, hinting at a possible solution to overcome the dose-limiting nephrotoxicity associated with the use of platinum-based anticancer drugs.[87] In addition, nanoparticle encapsulation of platinum-based anticancer agents can reduce their lability, which can lead to sustained circulation of the drug in the bloodstream.[79,80,86–88]

In addition to platinum anticancer agents, the incorporation of ruthenium-based antitumoral agents into nanoparticle delivery systems has been investigated.[89–91] Keppler and co-workers reported the first study of the nanoparticle delivery of Ru(III) drug candidate KP1019.[89] The initial study showed promising improvements in the *in-vitro* activity of **KP1019**.[89] Additionally, other studies show that rapid hydrolysis of **KP1019** in aqueous media can be circumvented nanoparticle encapuslation.[91]

Furthermore, in an extensive cytotoxicity study using multiple cell lines, Heffeter *et. al.* examined the activity of micelle-encapsulated **KP1019** versus free **KP1019** and observed an improved cytotoxicity for the encapsulated complexes due to increased cellular uptake.[91] Notably, an eight-fold (MCF-7 cell line) and twenty three-fold (SW1573 cell line) improvement in the cytotoxic activity of **KP1019** was observed when incorporating the complex into micelle delivery systems (IC_{50} values: 105 μM to 34 μM, and 770 μM to 34 μM respectively) versus free complex.[91] As noted above, **NAMI-A** type compounds exhibit little antitumoral activity, suffer from rapid water-exchange processes, and tend not to enter cells due to their interactions with extracellular components.[49] Thus, the use of nanoparticle systems to deliver Ru(III) complexes in the **NAMI-A** family of drug candidates is particularly promising.

1.4. Aptamers and Their Use in Medicine

Traditional drug delivery systems often suffer from off-target activity, poor solubility and bioavailability, and poor specificity. Nanoparticles provide an alternative route for efficient drug delivery. While nanoparticles exhibit passive ac through the EPR effect, they typically lack active targeting capabilities.[92] The surface modification of nanoparticles with biomolecules, can address this pitfall, and potentially introduce a high degree of specificity for the delivery of drugs to targeted tissues.[93,94] Particularly promising for this approach are aptamers, which are short synthetic, single-stranded DNA or RNA sequences capable of folding into tertiary and quaternary structures.[93] These biomolecules exhibit excellent physiological stability and biocompatibility, and have the potential to recognize and bind to a variety of targets including viruses, bacteria, proteins, cell-surface receptors, enzymes, and other cellular components.[93–95]

The versatility of aptamers makes them a formidable option as targeting molecules and biomarkers. Moreover, aptamers offer distinct advantages, such as high sensitivity, small size, minimal immunological response, low cost, simple large scale chemical production, and thermal stability.[93] A highly selective process known as Systematic Evolution of Ligands by Exponential Enrichment (SELEX) is used to generate aptamers.[96,97] This involves the creation of a diverse nucleic acid library, followed by multiple rounds of selection, during which the sequences that bind to a target molecule are retained, amplified, and cloned.[96] Consequently, the resulting sequences will be designed to have high specificity for a specific cellular target.

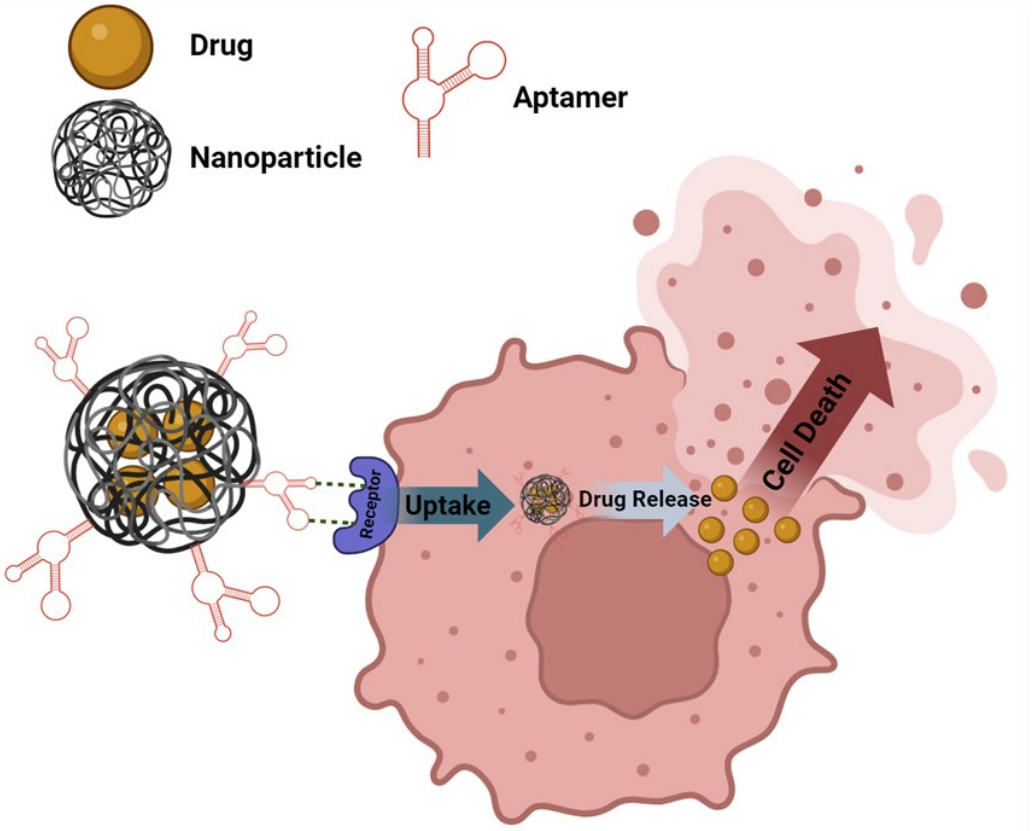

Figure 1.9. Aptamer-assisted nanoparticle delivery of pharmaceuticals leading to cell death.

The use of aptamers for targeting of various types of NP formulations has been extensively reported in the literature (**Figure 1.9**).[98–100] For example, aptamer-gold NPs (Apt-AuNP) have served as a valuable tool for the detection of malaria and Zika virus.[101] A distinctive colorimetric shift occurs in the presence of the target molecule, attributed to the binding of the aptamer gold-NPs to the target.[101] Aptamers can be modified with terminal groups for facile attachment to the surface of nanoparticles. For example, Lippard and co-workers demonstrated the decoration of carboxylic acid terminated PLGA-PEG nanoparticles with amine-terminated prostate-specific membrane targeting aptamers, through a well-established amide coupling reaction called the NHS/EDC.[88] These NPs were used to deliver cisplatin. The combination of nanoparticle encapsulated metal-based anticancer compounds, and the decoration of these delivery systems with targeting molecules like aptamers has the potential to enhance both efficacy and selectivity. This approach is developed in this thesis for **NAMI**-type Ru(III) complexes. More generally, this investigation aims to provide insight into the viability of these

delivery systems in addressing the challenges associated with Ru(III) anticancer and antimetastatic agents.

1.5. Thesis Overview

The research presented in this thesis is focused on designing and functionalizing biologically active analogs of the Ru(III) antimetastatic agent **NAMI** and using aptamer-functionalized nanoparticles as a delivery system. **Chapter 2** explores the syntheses of two novel analogs of **NAMI** through the incorporation of a fluorescent functional group, dansyl, into the organic ligand. A fluorinated analog of the ligand was also synthesized. The cytotoxic properties, aqueous ligand exchange behaviour, fluorescence quantum yields, and the aqueous solubility and stability of the two novel **NAMI** analogs are investigated. **Chapter 3** reports the synthesis and optimization of polymeric PLGA-PEG nanoparticle formulations. The **NAMI** analogs produced in **chapter 2** are encapsulated in the optimal NP formulations. The physical and chemical properties of the nanoparticle formulations such as surface charge, particle diameter, and drug release profile are investigated. The effects of aptamer-functionalization of drug-containing NPs on cell uptake and cytotoxic activity are explored. **Chapter 4** summarizes the work conducted, highlights the important findings and ideas of this thesis, and provides suggestions for future work.

Chapter 2. Novel Fluorescent Analogs of the Ru(III) Chemotherapeutic NAMI

2.1. Introduction

One of the most promising Ru(III) chemotherapeutics, **NAMI-A**, has been investigated extensively due to its promising antimetastatic properties (**Figure 2.1**). **NAMI-A** was the first Ru(III) complex to enter clinical trials. Unlike cisplatin, **NAMI-A** was completely non-cytotoxic *in-vitro* and *in-vivo* (mouse models), however in pre-clinical studies, it showed antimetastatic properties through the inhibition of tumor-cell detachment and motility.[102,103] Although the exact underlying mechanisms responsible for its anticancer activity are still under investigation, multiple hypotheses have been proposed.[39,43,46,49] The proposed mechanisms generally implicate coordinate and non-coordinate interactions of the complex with cellular and extracellular components. For example, interaction of **NAMI-A** with extracellular proteins and the extracellular matrix has been suggested as the source of its antimetastatic activity.[49]

The ligand exchange processes of **NAMI-A** involve the pH dependent hydrolysis of the chloride and/or the DMSO ligands.[104] However, the dissociation of the chloride ligand is more favorable at neutral pH.[104] This process then allows for direct interaction of the complex with proteins and DNA; however, the exact mechanism of action is still not well understood. Another highly controversial and debated hypothesis discusses the activation of the stable Ru(III) complex through its reduction to the more labile Ru(II) form in reducing physiological environments.[65,105]

Following promising preclinical findings, phase II clinical trials were conducted to determine the toxicity profile of **NAMI-A** in combination with Gemcitabine, which is a commonly used anticancer agent. During the phase II clinical trials, 32 patients with varying solid tumors were treated.[102] To further expand the trials, one patient needed to show partial remission. Unfortunately, this was not observed and as a result, further clinical trials with **NAMI-A** were not pursued. Although the clinical trials failed to allow for further investigation of **NAMI-A**, we believe that **NAMI-A** and **NAMI**-type Ru(III) complexes are worth further investigation for their potential as chemotherapeutic imaging compounds. In this chapter, the syntheses of novel fluorescent analogs of **NAMI**, the sodium compensated analog of **NAMI-A**, are described. The aim of this work

was to create analogs of **NAMI** (**Figure 2.1**) that can be used as imaging agents to reveal information about the behaviour of this class of Ru(III) compounds in physiological environments. The fluorescent analogs of **NAMI** incorporate a known fluorescent dye, dansyl, into the organic ligand of the classic **NAMI-A** complex. It is important to mention that we favored the sodium compensated salt **NAMI,** over **NAMI-A,** to eliminate any fluorescence contribution from the counterion and obtain a quantum yield that reflects only the contribution from the metal complex anion.

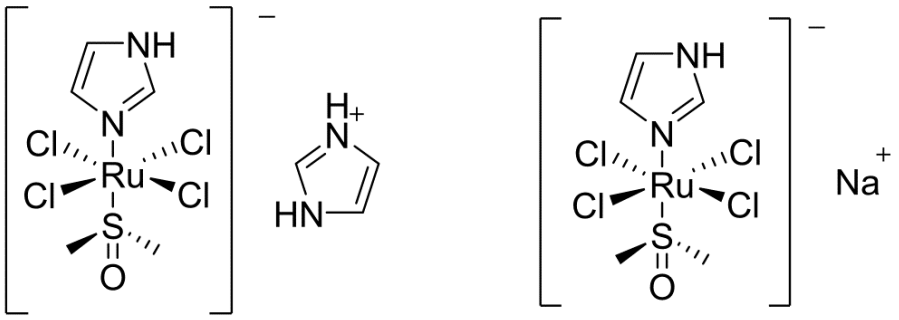

Figure 2.1. Chemical Structures of NAMI-A (left) and its sodium compensated analog NAMI (right).

Dansyl-based dyes are commonly used fluorophores in various biological applications such as cell imaging and protein sequencing. This family of dyes (**Figure 2.2**) display strong fluorescence in the presence of cellular proteins and DNA and have high quantum yields and large stokes shifts making them suitable for imaging of cellular components.[106] In addition, these molecules have good aqueous solubility and are found to permeate cell-membranes, potentially increasing cell uptake. Furthermore, dansyl dyes are relatively stable under physiological conditions. Moreover, appending of dansyl dyes to organic backbones can readily be achieved via amide coupling reactions through readily available starting material to provide an easy synthetic route for ligand synthesis (**Figure 2.2**).

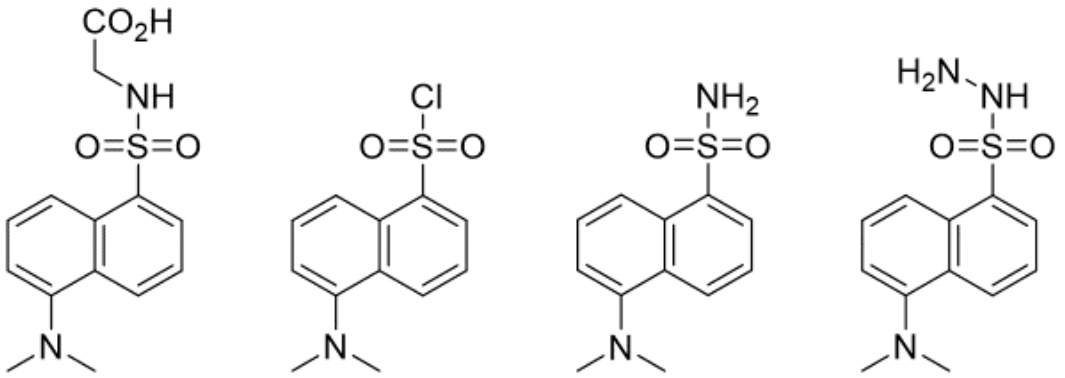

Figure 2.2. Chemical structures of Dansyl dyes. From left to right: Dansyl Glycine, Dansyl Chloride, Dansyl Amide, Dansylhydrazine.

Another approach to labeling biologically active molecules is by the inclusion of fluorine atoms. Functionalization of drugs with fluorine substituents can influence their physiochemical properties, pharmacokinetic profile, and biological activity.[107–109] This includes the alteration of the intra- and intermolecular interactions that lead to binding to biological targets, as well as the distribution, clearance, and the metabolism of drugs.[109] This has been shown for drugs that act on the central nervous system (CNS) where CF_3 substituents enhance their ability to permeate the blood-brain barrier, increasing their physiological activity and improving their pharmacokinetic profile.[107] Fluorine is also found to increase the metabolic stability of many drugs, increasing their circulation time and increasing their therapeutic window.[107,109,110] As a result, fluorination of chemotherapeutics, has been widely utilized in a number of pharmaceuticals.[111–113] Fluorine also serves as an excellent spectroscopic handle, notably for NMR studies. The most abundant isotope of fluorine, ^{19}F, has a 100% natural abundance with I = 1/2, and an overall sensitivity 83% of ^{1}H NMR.[114] This makes it ideal for NMR and Magnetic Resonance Imaging (MRI) studies in biological systems. Furthermore, fluorine is not naturally found in biological tissues, minimizing background signals and making spectra from ^{19}F labeled probes simple to interpret.[114]

In this chapter, a novel dansyl-based analog of **NAMI** and its fluorine-functionalized counterpart are synthesized with the aim of examining the effects of this functionalization on the overall physiological and chemical properties of the molecules.

The addition of this CF_3 group adds a second spectroscopic handle, allowing for analysis through ^{19}F NMR. Moreover, previous work by the Walsby research group shows that functionalization of Ru(III) anticancer complexes with fluorinated groups can increase the overall lipophilicity and cytotoxic activity.[115] Lipophilicity is known to play an important role in the uptake and clearance of successful drugs.[116] For instance, increasing lipophilicity is associated with lower clearance of drugs through the renal system.[117] In addition, since cell membranes are composed of a phospholipid bilayer, passive diffusion of molecules across the cell membranes depends on many factors including lipophilicity.[110,116,118]

The overall molecule design (**Figure 2.3**) retains the classic **NAMI** Ru(III) scaffold. This portion of the complex includes the exchangeable chloride and DMSO ligands that create vacant sites for protein/DNA interactions upon hydrolysis in physiological environments. The fluorescent dansyl functionality is attached to the Ru(III) centre via a pyridine linker (**Figure 2.3**). This pyridine linker has been widely used in the Walsby research group and its physiological stability and synthetic reliability have been established.[115] Pyridine linkers have been used previously in the Walsby research group because they provide synthetically accessible and stable connections between Ru centres and a wide range of functionalities. Moreover, the pyridine linker can be further modified at the secondary amine to tune its lipophilicity or hydrophilicity, such as through the introduction of the CF_3 moiety (**Figure 2.3**).

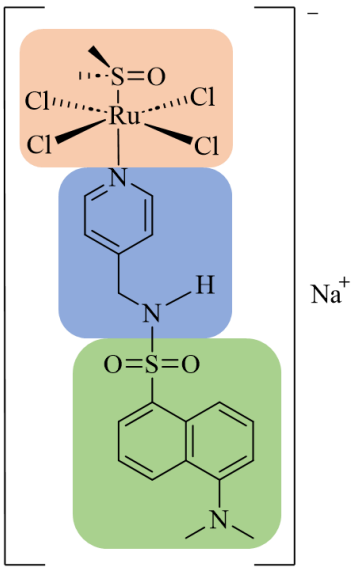

Figure 2.3. Molecular structure of the NAMI analog. Ruthenium Scaffold (Orange), Pyridine Linker (blue), Dansyl Fluorophore (Green).

2.2. Experimental

2.2.1. Materials and Instrumentation

Ruthenium(III) trichloride hydrate was purchased from Ambeed Inc., Dansyl chloride and 4-(Trifluoromethyl) benzyl bromide were purchased from Oakwood Chemical, 4-(aminomethyl) pyridine was purchased from Combi Blocks Inc. and all other reagents and materials were purchased from Sigma-Aldrich. ^{1}H, ^{13}C, and ^{19}F NMR spectra for all compounds were collected on a Bruker 500 MHz AVANCE III HD NMR spectrometer. Mass spectrometry data were collected using an Agilent Technologies 6210 ToF LC/MS system. Quantum yield measurements were collected using an Edinburgh FS5 spectrophotometer. UV-Vis measurements were collected using a PerkinElmer Lambda 850 UV/Vis Spectrophotometer and a 700 µL quartz cuvette with a pathlength of 10 mm. All NMR, MS and UV-Vis spectra can be found in **Appendix A**.

2.2.2. Synthesis

$H(DMSO)_2[trans\text{-}RuCl_4(DMSO)_2]$, **2-1**. Synthesis followed literature procedures.[15,36] In a 100 mL round bottom flask, Ru(III) trichloride monohydrate (1.0 g, 3.8 mmol) was suspended in 30 mL of ethanol and refluxed for 3 h to obtain a dark green solution. The solution was filtered to removed undissolved solids. The solution was concentrated to ~3 mL on rotary evaporator. Concentrated hydrochloric acid (37%, 1 mL) and DMSO (2 mL) were added and the solution was stirred at 80 °C for 15 min to obtain a bright orange solution. The solution was cooled to room temperature followed by the addition of acetone (10 mL). The final product was obtained by the dropwise addition of cold diethyl ether and filtration. The product was used without further purification to synthesize **2-2**.

$Na[trans\text{-}RuCl_4(DMSO)_2]$, **2-2**. Synthesis followed literature procedures.[119] In a 100 mL round bottom flask, ethanol (50 mL) and water (700 µL) were used to dissolve **2-1** (1.10 g, 2 mmol). NaCl (0.17 g, 3 mmol) was dissolved in water (500 µL) and added to the mixture. Upon the addition of NaCl, bright orange solids precipitated. The solution was stirred for 15 mins. Precipitates were washed with cold ethanol and cold ether and dried. The product, a bright orange powder, was used in subsequent syntheses without further purification.

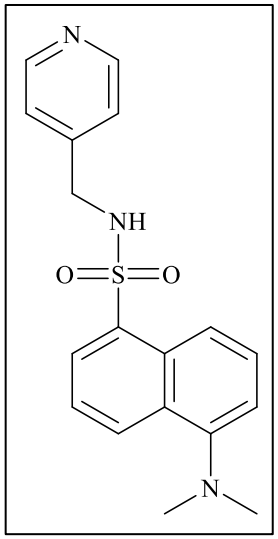

5-(dimethylamino)-N-(pyridin-4-ylmethyl) naphthalene-1-sulfonamide, 2-3 (**DSC-Pyr**). Synthesis followed literature procedures.[106] In a 50 mL round bottom flask, dansyl chloride (0.3 g, 1 mmol) was dissolved in dry DCM (10 mL). 4-(aminomethyl) pyridine (0.34 mL, 3 mmol) was added to the solution. The mixture was stirred at room temperature overnight. The solution was diluted with water (20 mL). The mixture was extracted with DCM (3 x 20 mL) and dried over Na_2SO_4 and concentrated. The crude product was purified by column chromatography on silica gel by eluting with methanol/hexane/ethyl acetate (1:3:6, v/v/v) to yield the pure final product, a white powder. Yield: 81%. $C_{18}H_{19}N_3O_2S$ Calculated C, 63.38; H, 5.61; N, 12.32. Found C, 63.10; H, 5.56; N, 12.55. MS: Calculated $[M+H]^+$: 342.127 *m/z*, Observed $[M+H]^+$: 342.123 *m/z*. ^1H NMR (500 MHz, $CDCl_3$) δ 8.48 (d, J = 8.6 Hz, 1H), 8.30 (d, J = 8.7 Hz, 2H), 8.24 (d, J = 6.1 Hz, 2H), 8.20 – 8.13 (m, 1H), 7.44 (dt, J = 11.9, 8.0 Hz, 4H), 7.14 (d, J = 7.5 Hz, 2H), 6.98 (d, J = 6.2 Hz, 2H), 6.77 (t, J = 6.5 Hz, 2H), 4.07 (d, J = 6.0 Hz, 3H), 2.86 (s, 11H).

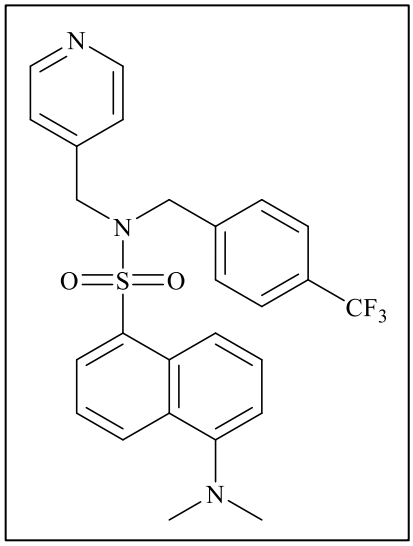

5-(dimethylamino)-N-(pyridin-4-ylmethyl)-N-(4-(trifluoromethyl) benzyl) naphthalene-1-sulfonamide, 2-4 (**Benzyl-CF_3-DSC-Pyr**). Synthesis followed modified literature procedures.[120] In a 50 mL round bottom flask, **2-3** (0.2 g, 0.6 mmol) was dissolved in DMF (5 mL). To the solution four molar equivalence of K_2CO_3 (0.3 g, 2 mmol) was added. The mixture was stirred at room temperature for 30 min. 4-(Trifluoromethyl) benzyl bromide (0.14 g, 2 mmol) was dissolved in DMF (1 mL) and added to the mixture and the solution was stirred at room temperature overnight. The resulting solution was diluted with 50 mL of DCM and DMF was removed through extractions with water (3 x 300 mL) and brine (3 x 300 mL). The organic layer was dried with Na_2SO_4 and concentrated. The crude product, a light brown oil was purified by column chromatography on silica gel by eluting with methanol/hexane/ethyl acetate (1:2:7, v/v/v) to yield the pure final product, a colorless oil. Yield: 51%. $C_{26}H_{24}F_3N_3O_2S$ Calculated C, 62.51; H, 4.84; N, 8.41. Found C, 62.58; H, 4.99; N, 8.60. MS: Calculated

$[M+H]^+$: 500.161 *m/z*, Observed $[M+H]^+$: 500.158 *m/z*. ^1H NMR (500 MHz, $CDCl_3$): δ 8.58 (d, J = 8.5 Hz, 0H), 8.42 – 8.38 (m, 0H), 8.29 (t, J = 8.0 Hz, 0H), 7.59 (dd, J = 8.7, 7.6 Hz, 0H), 7.50 (dd, J = 8.5, 7.3 Hz, 0H), 7.40 (d, J = 8.0 Hz, 0H), 7.24 (d, J = 7.6 Hz, 0H), 7.04 (d, J = 8.1 Hz, 0H), 6.89 (d, J = 6.1 Hz, 0H), 4.45 (s, 0H), 4.39 (s, 0H), 2.92 (s, 1H). ^{19}F NMR (376 MHz, $CDCl_3$): δ -62.70.

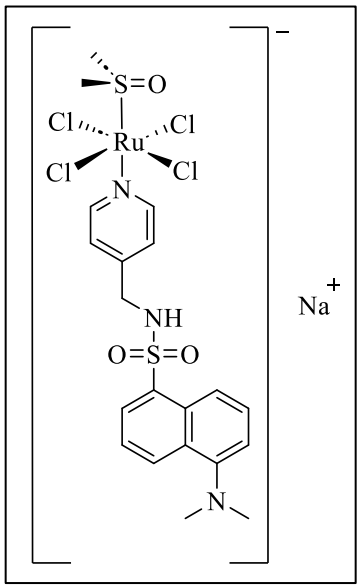

Na[trans-RuCl$_3$(DSC-Pyr)(DMSO)], **2-5**. Synthesis followed modified literature procedures.[35,36,119,121] In a 50 mL round bottom flask, **2-2** (100 mg, 0.24 mmol) was suspended in dry acetone (10 mL). **2-3** (100 mg, 0.29 mmol) was dissolved in dry acetone (3 mL) and was added dropwise to the solution. The mixture was stirred at room temperature for 3 h. The solution was reduced under pressure to ~5 mL. Cold ether was added slowly to precipitate the crude product. The crude product, mustard yellow oil, was purified by column chromatography on silica gel by eluting with ethyl acetate/hexane/methanol (5:4:1, v/v/v) to yield the pure product, a dark orange powder. Yield: 82%. MS: Calculated $[M+NH_4+H]^+$: 681.952 *m/z*, Observed $[M]^-$: 681.932 *m/z*. Observed [M]-: 662.946 m/z. Calculated [M]-: 662.912 m/z. ^1H NMR (500 MHz, $CDCl_3$): δ 8.17, 7.06, 6.93, 5.11, 4.06, 2.78, 1.98, 1.20, 0.83, -0.90, -2.23, -13.34.

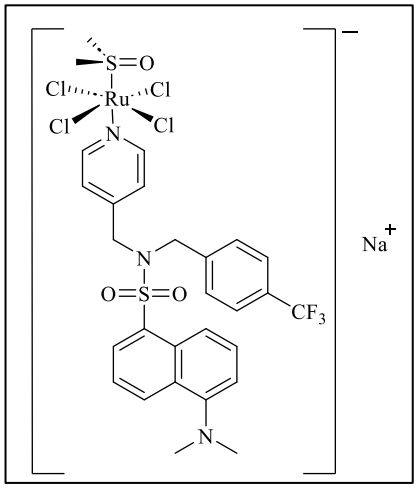

Na[trans-RuCl$_3$(BCF$_3$-DSC-Pyr)(DMSO)], **2-6**. Synthesis followed modified literature procedures.[35,36,119,121] In a 50 mL round-bottom flask, **2-2** (100 mg. 0.28 mmol) was suspended in dry acetone (10 mL). **2-4** (140 mg, 0.28 mmol) was dissolved in dry acetone (3 mL) and was added dropwise to the solution. The mixture was stirred at room temperature for 3 h. The solution volume was reduced under vacuum to ~5 mL and cold ether was added slowly to precipitate the crude product. The crude product, a brown oil, was purified by column chromatography by eluting with ethyl acetate/hexane/methanol (6:3:1 ,v/v/v) to yield the pure final product, bright orange powder. Yield: 50%. MS: Calculated $[M+NH_4+H]^+$: 839.986 *m/z*, Observed $[M+NH_4+H]^+$:

839.957 *m/z*. Observed $[M]^-$: 820.984 m/z, calculated $[M]^-$: 820.945 m/z. ^{1}H NMR (500 MHz, $CDCl_3$): δ 8.42, 7.45, 7.16, 6.49, 6.16, 2.98, 1.21, 0.82, -0.59, -2.36, -13.15. ^{19}F NMR (376 MHz, $CDCl_3$): δ= -62.24.

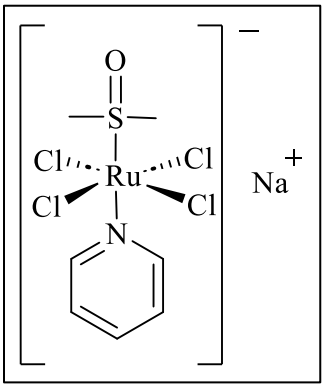

Na[trans-RuCl$_3$(Pyr)(DMSO)], 2-7. Synthesis followed literature procedures. [35,36,119,121] In a 50 mL round-bottom flask, **2-2** (100 mg, 0.24 mmol) was suspended in dry acetone (10 mL). Pyridine (19 µL, 0.24 mmol) was added to the solution in a dropwise manner and the solution was left to stir at room temperature for 4 h. The volume of the resulting dark orange solution was reduced under vacuum to 1 mL, 5mL of cold ether was then added to precipitate the crude product. The crude brown solids were purified by column chromatography by eluting with acetone/hexane (8:2, v/v) to yield the pure orange solid product. The product was used as a cell cytotoxicity control. Yield: 45.7%.

2.2.3. UV-Vis Stability Studies

Stock 50 mM solutions of **2-5** and **2-6** were prepared in DMSO and diluted to 200 µM using 1x PBS (pH 7.4, Chloride concentration of 134 mM) for analysis. To aid in the solubility of **2-6**, acetone (<1%) was added. UV-Vis measurements were collected using a PerkinElmer Lambda 850 UV/Vis Spectrophotometer and a 700 µL quartz cuvette with a pathlength of 10 mm. The scan range was set to 600-300 nm with 2.00 nm scan intervals and a slit width of 2.00 nm. UV-Vis spectra were collected every 2 to 5 minutes over a period of 1 to 3 hours at 25 °C.

2.2.4. NMR Ligand-Exchange Measurements

Measurements were taken using a Bruker 500 MHz AVANCE III HD NMR spectrometer. Stock 50 mM solutions of **2-5** and **2-6** were prepared in deuterated DMSO. From the stock solutions, 5 mM (for **2-5**) and 2.5 mM (for **2-6**) solutions in 1x deuterated PBS pH 7.4 (chloride concentration of 134 mM) were prepared. ^{1}H and ^{19}F NMR measurements were taken from the samples at 15-minute intervals at room temperature over 2 hours. Due to solubility difficulties with **2-6** a small amount of deuterated acetone (<1%) was doped into the sample.

2.2.5. Fluorescence Quantum Yield Measurements

Measurements were collected using an Edinburgh FS5 spectrophotometer, direct measurement method, 3 mL quartz cuvettes (10 mm pathlength), scan range of 315-700 nm, 335 nm excitation and emission wavelengths, 1.0 nm scan steps, 1.0 sec dwell time, 10 nm excitation bandwidth, and 0.55 nm emission bandwidth. Stock 5 mM solutions (in DMSO) of dansyl glycine, **2-3**, **2-5** and **2-6** were used to prepare 200 µM solutions in 1x PBS (pH 7.4, 134 mM NaCl, <1% acetone) for analysis at 25 °C. Acceptable measurements of **2-4** were not obtained due to solubility difficulties. A solution of 1x PBS (pH 7.4, 134 mM NaCl, <1% acetone) was used as a reference. Quantum yield values were calculated using the Fluoracle® software through the comparison of the area under the emission peaks from 350-700 nm.

2.2.6. Log*D* Calculations

Experimental Calculations

The shake-flask method using PBS pre-saturated n-octanol and n-octanol pre-saturated PBS solution (containing NaCl (137 mM), KCl (2.7 nM), Na_2HPO_4 (10 mM), and KH_2PO_4 (2 mM), pH 7.4) was used to determine the distribution coefficient (Log*D*) of the ruthenium complexes. From stock 5mM solutions of **2-5** and **2-6** in DMSO, 200 µM solutions in n-octanol pre-saturated PBS were prepared. The solutions were mixed with n-octanol (1:1 ratio, v/v) on an orbital shaker for 24h at 25 °C. the mixtures were centrifuged at 5000 rpm for 3 minutes at 25 °C. UV-Vis spectra were taken of the aqueous phase before, and after shaking, and the absorbance at λ_{max} was compared to ascertain the value of *D*.

Theoretical Calculations

Due to the limited aqueous solubility, ligand-exchange behaviour and rapid precipitation of the complexes out of solution, experimental methods to determine Log*D* values failed to produce usable results. Therefore, Playground software (Chemaxon, Budapest, Hungary) was used to determine theoretical distribution coefficients. The calculations follow a method developed by Viswanadhan *et. al.* where each fragment of the molecule is assigned a predetermined distribution coefficient.[122] The distribution

coefficient of the molecule is calculated as the sum of all the partition coefficients of the fragments.

2.2.7. *In-Vitro* Cytotoxicity studies*

MTT Assay in U2-OS (human osteosarcoma) Cells*

Stock 20 mM solutions of **2-3**, **2-4**, **2-5**, and **2-6** were prepared in DMSO. Stock solutions were diluted into 384 well plates to a top working concentration of 100 μM. The samples were then diluted using a 3x serial dilution 8-point curve. Each plate contained DMSO as a negative control and Latrunculin B as a positive control. U2-OS cells were plated at a density of 2400 cells per well in 40 μL of media. 24 hours after seeding, cells were treated with the compounds and controls. After 24 hours of treatment, media was exchanged and the MTT solution was added to each well. Cells were incubated for 4 hours at 37 °C before washing. Absorbance as measured at 540 nm on a Biotek plate reader. All samples were run in singlets.

MTT Assay data analysis*

Dose-response data for each compound was subject to model fitting as follows: using the R package DRC (dose response curve), the 4-parameter log-logistic (LL4) model was fit with the upper bound for the upper limit of the curve set to 1.25, and the lower bound for the lower limit set to 0. The rest of the boundaries for the 4 parameters were set to default (∞ for the upper asymptote and -∞ for the lower asymptote). Using the R package broom, the following statistical measures were obtained: 1) The Corresponding *p-value* for the EC_{50} estimation and 2) The residual standard error (RSE) of the model. Compounds were defined as active when they have EC_{50} < 100 μM, a negative hill slope, and lower limit <0.5. Compounds were defined as inactive if they had EC_{50} > 100 μM, a positive hill slope, or a lower limit >0.5.

* The in-Vitro cytotoxicity studies and analyses were done in a collaboration with Bold Therapeutics. The MTT Assays were performed at the centre for high-throughput for chemical biology at Simon Fraser University, while the remaining assays and cytotoxicity work were done by the Raynal Research Group at Département de pharmacologie et physiologie, Faculté de médecine, Université de Montréal.

2D ViaCount Assay in HCT-116, MRC-5, and HEP-3B Cells*

Stock 20 mM solutions of **NAMI**, **2-3**, **2-4**, **2-5**, **2-6, and 2-7** were prepared in DMSO. The stock solutions were then diluted into 96 well plates to a top working concentration of 100 µM. The samples were then diluted using an 8-point dilution curve. Cells were cultured in their appropriate media supplemented with 10% fetal bovine serum (FBS). HCT-116, HEP-3B, and MRC-5 cells were cultured and seeded in 96-well plates 24 hours before treatment. Cells were treated for 72 hours with 8 increasing doses of the compounds (0.001, 0.01, 0.1, 0.5, 1, 5, 10, 50, and 100 µM). DMSO was used as a vehicle control to normalize viabilities. Each test compound was screened in a single replicate. Viability was measured using Guava ViaCount Fluorescent Viability Dye Reagent (Luminex, Austin, TX, USA) on a Guava EasyCyte 6HT High-Throughput Flow Cytometer (EMD-Millipore, Burlington, MA, USA). Data were plotted and the half-maximal inhibitory concentration (IC_{50}) values were calculated in GraphPad Prism using log(inhibitor) vs. response-variable slope (four parameter) and the least square method. The dose response data are presented as the concentration of the drug in µM vs. the fraction of affected cells.

Synergy Assay with Standard of Care (SOC) Agents*

Based on previously obtained dose-response curves, the IC_{30} value of **2-6** was calculated. This value was used to obtain the 2 µM concentration to be used for the synergy screen. A 72-hour ViaCount assay in the 2D colon cancer cell line (HCT-116) was performed in a single replicate. To assess the potential synergy with SOC agents, the following compounds were run in the ViaCount assay in parallel in the cancer model: Paclitaxel (2 nM), 5-fluoroucil (60 µM), Irinotecan (5 µM), AZD6783 (25 µM), and Olaparib (100 µM). Drug synergy between each SOC and **2-6** was assessed using effect-based combination indices (CI) with Bliss formula. ViaCount Assay was performed using Guava ViaCount fluorescent viability dye agent (Luminex, Austin, TX, USA) on a Guava EasyCyte 6HT High-Throughput Flow Cytometer (EMD-Millipore, Burlington, MA, USA). Cells were treated for 72 hours at appropriate concentrations. Obtained normalized viabilities were used to assess synergy between **2-6** and each SOC combination pair.

2.3. Results and Discussion

2.3.1. Molecular Design, Synthesis and Characterization

The design concept for the complexes in this chapter was to create ligand-metal complexes resembling the sodium-compensated analog of **NAMI-A**, that also possess reliable spectroscopic handles to aid in the intracellular visualization of the drug candidates. In addition, our design rational revolved around creating a versatile and modifiable ligand that can serve as a foundation for future researchers in the group. As explained in the thesis introduction, although Ru(III) anticancer and antimetastatic agents like **KP1019** and **NAMI-A** show promise, the mechanism of action of these drugs is poorly understood. Therefore, by creating novel fluorescent analogs of these compounds, and developing reliable cell delivery methods, we hope to create a path to investigating the underlying intra- and intercellular interactions of these Ru(III) molecules. Since **NAMI**-type complexes are negatively charged, they are accompanied by a cation to balance the charged metal complex. The cation is usually the positively charged organic ligand, and in the case of **NAMI-A**, the counterion is the positively charged imidazolium ion. However, having the ligand as the counterion provided some potential issues for this project. Fluorescence arising from compensating cation could inhibit measurement of the metal-complex's physiological interactions and presence. Therefore, Na^+ was chosen as the counterion. Moreover, **NAMI** (the sodium compensated complex) demonstrated similar biological properties as **NAMI-A**, and has better aqueous solubility and an easy synthetic route.[44]

As outlined in **Chapter 2.1**, dansyl-based dyes are invaluable fluorophores in biological environments due to their relatively high quantum yields and large stokes shifts. The use of 4-(aminomethyl)-pyridine as the linker molecule between the fluorophore and the Ru(III) scaffold (**Figure 2.3**) was done with the goal of creating a path for future modification of the parent molecule. The secondary amine provides a highly modifiable site for the conjugation of spectroscopic handles, and bioactive molecules for improved pharmacokinetics and uptake. In addition, the hydrocarbon chain on this linker molecule can be lengthened to alter the water solubility of the overall complex and change its lipophilicity profile.

The syntheses of the organic ligands followed simple and highly reproducible literature procedures (**Figure 2.4**) and involved a one-step coupling reaction between 4-(aminomethyl)-pyridine and dansyl chloride in dichloromethane to produce **2-3** with an acceptable 82% yield. The functionalization of **2-3** with 4-(trifluoromethyl)-benzyl bromide was carried out following a modified literature procedure to increase the overall yield.[123] The structures of both ligands were confirmed and analyzed using ^{1}H and ^{13}C NMR, MS, and ^{19}F NMR. The spectra for these analyses are presented in **Appendix A**.

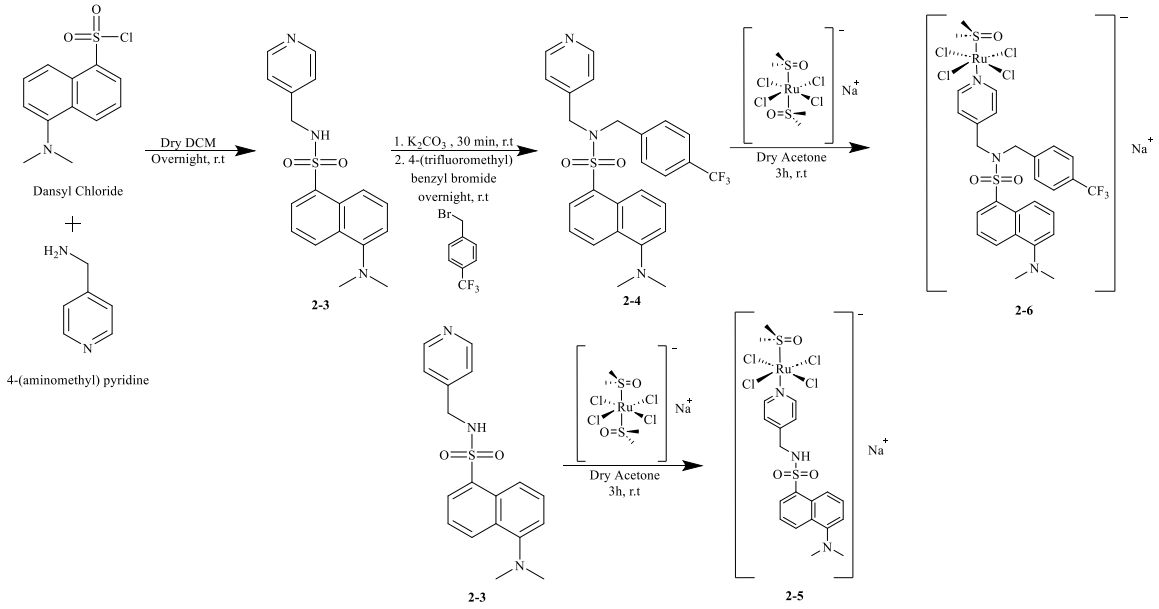

Figure 2.4. The synthetic scheme for the novel NAMI analogs.

The comparison of the ^{1}H NMR data (**Figure A.1** and **Figure A.3**) of **2-3** and **2-4** shows an obvious conversion of the doublet at 4.07 ppm which accounts for 2 protons, to the two singlets at 4.45 and 4.39 ppm each accounting for 2 aliphatic protons. Moreover, the disappearance of the triplet signal (6.77 ppm, 1H) from the secondary amine on **2-3** further confirms the coupling of the 4-(trifluoromethyl)-benzyl moiety to the ligand and the conversion of the secondary amine to a tertiary amine. To attach the organic ligands to the ruthenium scaffold, a previously established synthetic approach for **NAMI-A** was followed.[119] **NAMI** and **NAMI-A** are prepared through the replacement of one of the axial DMSO ligands of Na[*trans*-$RuCl_4(DMSO)_2$] with a heterolytic nitrogen-donor ligand. This chemical reaction is quite straightforward and involves the dropwise addition of the organic ligand to a suspension of Na[*trans*-$RuCl_4(DMSO)_2$] in dry acetone.

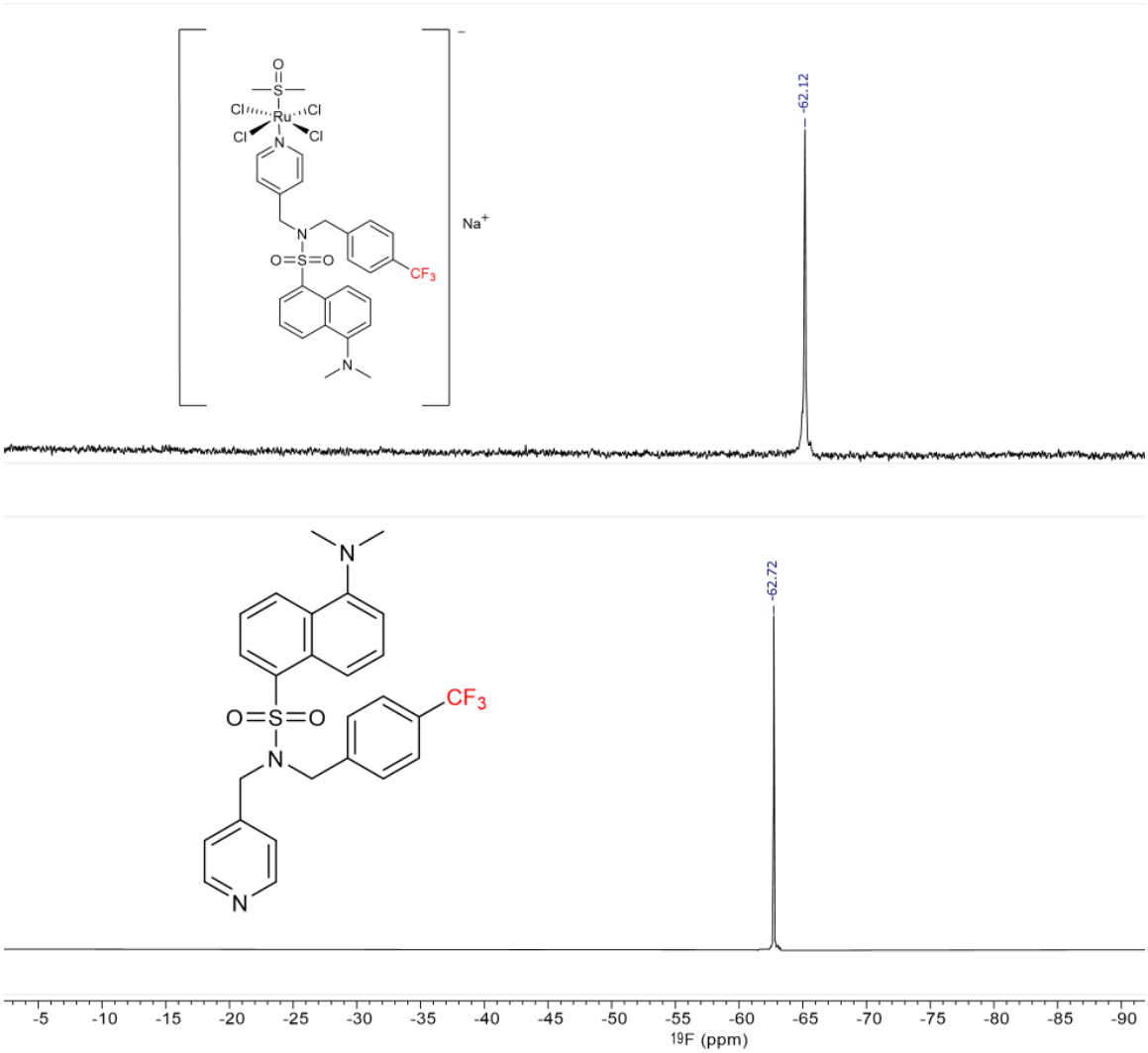

Figure 2.5. Upfield shift of the fluorine signal upon attachment of 2-4 to Ru(III).

Although the syntheses of the **NAMI** analogs were simple, the characterization of these complexes proved to be challenging. Due to the influence of the paramagnetic Ru(III) metal centres, most ^{1}H NMR signals are broadened and have lower intensity.[124] Hence, making reliable ^{1}H assignments quite challenging. However, the broadened peaks with the unique chemical shift at approximately -13.0 ppm, from the axial DMSO ligand, and the two shifts around -0.86 ppm and -3.06 ppm, from the pyridine ring of the fluorophore, can be seen in the NMR spectra of both metal complexes.[119,125] In addition, the ^{19}F spectroscopic handle can be used to further confirm the successful synthesis and purity of **2-4** and **2-6**. The ^{19}F NMR of the ligand (**2-4**) shows a singlet peak at -62.72 ppm. Upon the attachment to the Ru(III) scaffold, the peak arising from the fluorine

atoms shifts upfield to -62.12 ppm and broadens slightly (**Figure 2.5)**. Finally, to further confirm the attachment of the organic ligands and the successful synthesis of the **NAMI** analogs, MS was employed. Since both of the synthesized Ru(III) complexes are negatively charged salts, their mass spectra are easily recognizable in negative mode (**Figure A.11** and **A.12**). Unfortunately, due to the poor in-solution stability of the complexes, suitable crystals of **2-5** and **2-6** could not be obtained despite countless efforts using various conditions and methods.

2.3.2. Lipophilicity and Log*D*

Lipophilicity denotes the tendency of a molecule to dissolve in lipids. Given that cell membranes are primarily composed of lipids forming a bilayer, lipophilic molecules possess an advantage in permeating (through passive diffusion) these membranes compared to their hydrophilic counterparts. While various factors like molecule size, charge, and shape influence cell membrane permeability of pharmaceuticals, lipophilicity plays a significant role.

The determination of a molecule's lipophilicity or hydrophilicity is typically carried out experimentally, often involving water/octanol distribution measurements. In this context, distribution coefficients (Log*D*) serve as crucial metrics. Extensive efforts were undertaken to ascertain Log*D* values for the ligands and both ruthenium complexes in phosphate buffered saline (PBS) and octanol by utilizing the shake flask method.[126] Unfortunately, due to rapid aqueous ligand-exchange, precipitation of complexes, and solubility challenges, obtaining meaningful results was not possible.

Alternatively, partition coefficients can be determined using a method pioneered by Viswanadhan *et. al*. [122] This method involves calculating Log*D* values by summing the individual distribution coefficients of each molecular fragment. In this study, Log*D* values were computed using the Playground application developed by Chemaxon. The calculated Log*D* values for the compounds at physiological pH (7.4) are presented in **Table 2.1**.

As expected, functionalizing the ligand **2-3** with the trifluoromethyl benzyl group led to a notable increase in the distribution coefficient, elevating it from 2.40 to 5.32. consequently, this modification resulted in the creation of a more lipophilic compound.

Similarly, significant enhancements in lipophilicity were observed in the ruthenium complexes, where the non-fluorinated complex exhibited a Log*D* value of 4.92, while the fluorinated complex, **2-6**, displays a Log*D* value of 7.82. The incorporation of the trifluoromethyl benzyl moiety into the drug remarkedly augmented the molecule's lipophilicity. This enhancement holds potential implications for increased cellular uptake and cytotoxic activity, as extensively documented in the literature.[115,127] Its important to mention that although the theoretically calculated Log*D* values of the metal-complexes can be used to compare the effect of fluorination on the compounds, these calculations have limitations and may not be an accurate representation of experimentally determined distribution coefficients.

Table 2.1. Computed Water/Octanol Distribution Coefficients (Log*D*) for the synthesized compounds at pH 7.4.

Compound	Theoretical Log*D* at pH 7.4
2-3	2.40
2-4	5.23
2-5	4.92
2-6	7.82

2.3.3. Aqueous Solution Behaviour

^{1}H and ^{19}F NMR Measurements in PBS

Metal-based anticancer and antimetastatic compounds like, cisplatin, **NAMI-A**, and **KP1019** can interact with biomolecules in cell following ligand-exchange processes. This transformation through the ligand-exchange process has been suggested to be responsible for the activity of many metal-based chemotherapeutics. In the case of the Ru(III) compounds, this activation involves the aquation of the complex through the replacement of one or more of the coordinated ligands (usually the chloride or the DMSO ligands). This ligand-exchange is followed by the coordination/interaction of the aquated specie with biological targets.[4] Therefore, it is crucial to understand the underlying exchange processes that allow these interactions. To investigate the ligand-exchange behaviour of the synthesized **NAMI** analogs, time-dependent ^{1}H NMR measurements were collected in 1x PBS at physiological pH (7.4). The ^{1}H NMR of **NAMI/NAMI-A** have previously been investigated and assigned by Alessio *et. al*.[125]

The ^{1}H NMR spectrum of **NAMI** exhibits two groups of peaks: (1) an upfield shifted and extremely broad peak at approximately -15 ppm from the DMSO ligand, (2) paramagnetically shifted peaks of the imidazole ligand centered at -7.8, -5.6, and -3.5 ppm.[44,125] The hydrolysis of **NAMI** in aqueous media results in the gradual disappearance of the NMR signals from the parent compound, and their replacement with new signals arise from aquated species and dissociated ligands. At mildly acidic pH, the dissociation of the DMSO ligand is favored. This pH-dependent exchange, results in the disappearance of the parent molecule from the solution within 15 minutes at physiological temperature (37 °C).[44] Moreover, this exchange process results in the precipitation of dark-green poly-oxo species.

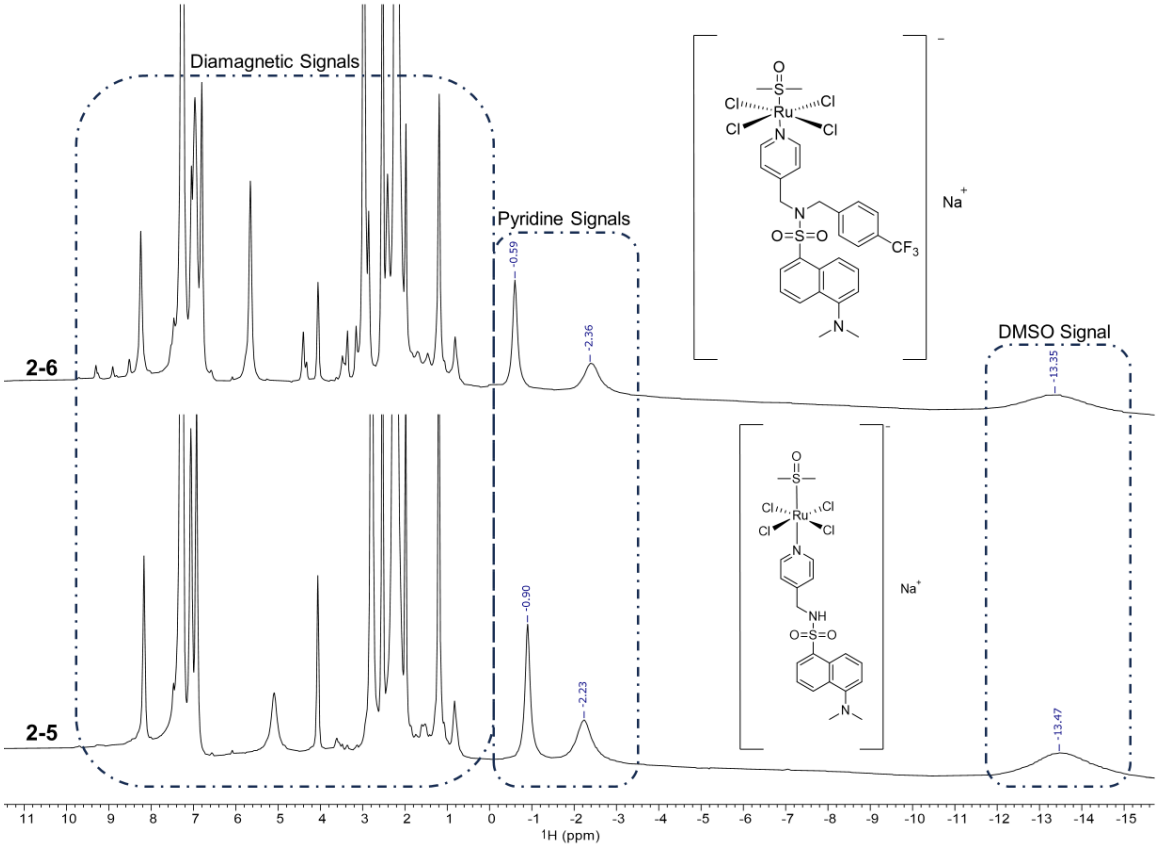

Figure 2.6 **^{1}H NMR (500 MHz, $CDCl_3$) of 2-5 and 2-6. 2-5 (bottom): -13.47 ppm (DMSO), -2.23 ppm and -0.90 ppm (pyridine linker), 2-6 (top): -13.35 ppm (DMSO), -2.36 ppm and -0.59 ppm (pyridine linker).**

The ^{1}H NMR spectra of **2-5** and **2-6** exhibit three groups of resonances: (1) the broad upfield shifted signal from the DMSO ligand at approximately -13 ppm, (2) a pair of broad and paramagnetically-shifted peaks from the methyl pyridine linker at -0.59 and

-2.36 ppm (for **2-5**), and -0.90 and -2.23 ppm (for **2-6**), (3) broadened signals from the protons on the dansyl/trifluoromethyl benzene in the diamagnetic regions (**Figure 2.6**). To examine the ligand-exchange behaviour of the two Ru(III) complexes in solution, time-based ^{1}H and ^{19}F NMR scans of the compounds in PBS were performed.

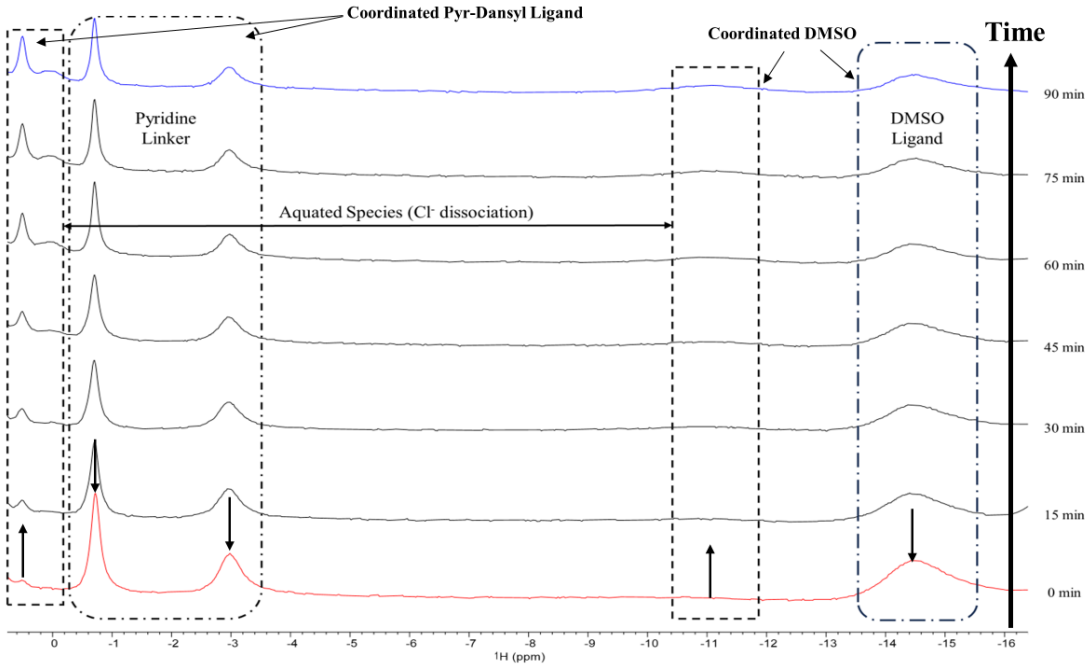

Figure 2.7. Time-based ^{1}H NMR (500 MHz) measurements of 2-5 in PBS (D_2O) pH 7.4 (red = 0 min, blue = 90 min)

The time-based ^{1}H NMR measurements of **2-5** in PBS presented in **Figure 2.7** report the change in signals due to the formation of new chemical species. The examination of these spectra shows a gradual decrease in the broad signal from the coordinated DMSO ligand which initially appears at approximately -14.5 ppm in solution. Moreover, the two broad signals from the pyridine linker at -0.71 ppm and -2.97 ppm decrease in intensity in a similar manner. At first glance, one may assume that this is due to the dissociation of the fluorophore and the DMSO ligands from the complex. However, upon closer examination of the diamagnetic region of the spectra (**Figure A.13**), no visible signals from free DMSO (which is normally seen at 2.78 ppm) nor the free dansyl-pyridine ligand are observed. Concurrently, the formation of a green precipitate is observed as the measurements are taken, consistent with a decrease in the signal intensities from DMSO and the linker could be due to precipitation of the complex through the formation of poly-oxo species.[44,49] Additionally, the formation of an

extremely broad and weak signal at approximately -11.0 ppm is observed, which is assigned to the coordinated DMSO ligand of the mono-aquo species formed following the loss of a chloride ligand.

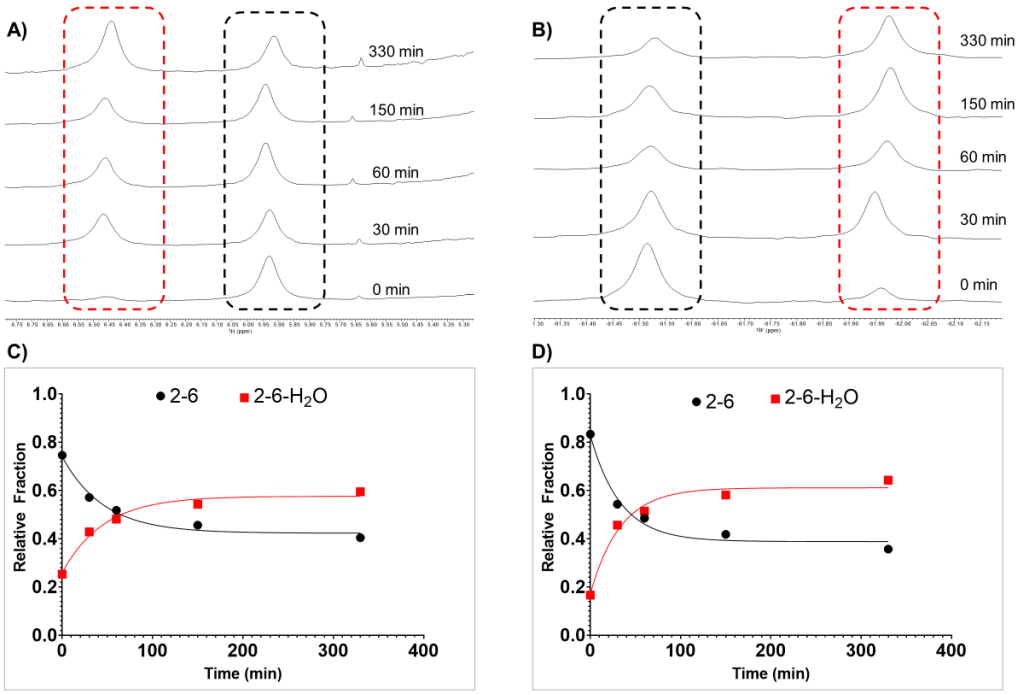

Figure 2.8. NMR ligand-exchange studies of 2-6 in 1xPBS (pH 7.4, 134 mM NaCl) over 330 minutes. A) ^{1}H NMR. B) ^{19}F NMR. Relative contribution from parent complex and the aquo-complex as determinted by the area under the fitted NMR peaks (MestReNova) for C) ^{1}H NMR D) ^{19}F NMR.

In addition, the broad signals in the diamagnetic region change over time. While some of the signals reduce in intensity (8.64, 7.68, 7.19, 6.95, and 6.64 ppm), an increase in signal intensity of new signals (8.73, 8.55, 8.47, 7.56, 7.44, and 7.38 ppm) is observed indicating the formation of new aquo species due to ligand-exchange processes (**Figure A.14**). Finally, due to a lack of evidence for the dissociation of DMSO and the organic ligand, which is marked by the absence of signals from those free species, we can conclude that the chloride dissociation is the primary exchange event within the first 90 minutes of aqueous dissolution of **2-5**. Although time-based NMR measurements of **2-6** in PBS shows similar ligand-exchange behaviour as **2-5**, the aquation process occurs at a different rate. Examining the time-based ^{1}H NMR scans of **2-6** in PBS over 5.5 hours, a similar reduction in the paramagnetic resonance from the

coordinated DMSO ligand at -13.48 ppm is observed. Moreover, an increase in intensity of a paramagnetic signal at approximately -10.5 ppm is detected, which is likely from the DMSO ligand of the mono-aquo species described above. The diamagnetic region of the spectra also sees major shifts. For example, the resonance at 5.92 ppm slowly decreases in intensity over 300 minutes, while the resonance at 6.44ppm, which is caused by the **2-6-aquo** species increases in intensity (**Figure 2.8**).

The ^{19}F NMR spectra also indicate a similar shift in the dominant species in solution. Within the first hour of aqueous dissolution of **2-6**, the mono-aquo exchange-products become the dominant species in solution, and a relative equilibrium is reached at approximately 300 minutes. Moreover, we can attribute the formation of the aquo species to hydrolysis of the chloride ligand due to the absence of signals from free-DMSO or free-ligand in the spectra. The aqueous ligand-exchange results of **2-5** and **2-6** are consistent with the ligand-exchange behaviour of **NAMI**, **NAMI-A** and **Pyridine-NAMI** in the literature.[127] These data indicate that the Ru(III) complexes synthesized in this chapter will undergo partial hydrolysis of the chloride ligand within the first 90 minutes following aqueous dissolution to form their respective aquo species. Moreover, as indicated by literature reports, Ru(III) anticancer/antimetastatic compounds undergo "activation" to engage with biomolecules through ligand-exchange processes. These findings provide valuable insight into this process.

UV-Vis Stability Studies in PBS

To further investigate the aqueous solution behaviour of the synthesized Ru(III) analogs of **NAMI**, UV-vis measurements were taken. From 50mM stock solutions (in DMSO) of **2-5** and **2-6**, 200 μM samples in 1x PBS (pH 7.4, 134 mM NaCl) were prepared and UV-Vis spectra were collected at 5-minute intervals over 3 hours at 25 °C. In accordance with the NMR measurements, the UV-Vis data for **2-5** and **2-6** show spectral changes indicating the occurrence of ligand-exchange processes. The UV-Vis spectrum of **2-5** immediately after aqueous dissolution, which is presented in **Figure 2.9**, shows two strong absorption peaks at 335 nm and 392 nm.

The peak at 392 nm likely rising from the Ru(III) centre, attributed to the ligand-to-metal charge transfer (LMCT) transition, whereas the exchange product shows an absorbance at 335 nm. Monitoring these absorption peaks over time, we can see the

gradual disappearance of the peak at 392 nm, and the increase in intensity of the peak from the ligand-exchange product. The observed isosbestic point is indicative of a single ligand-exchange process. This is consistent with the NMR study described above. The formation of poly-oxo species that precipitate during the experiment, inhibited the analysis of the exchange behaviours of the compounds in subsequent time points.

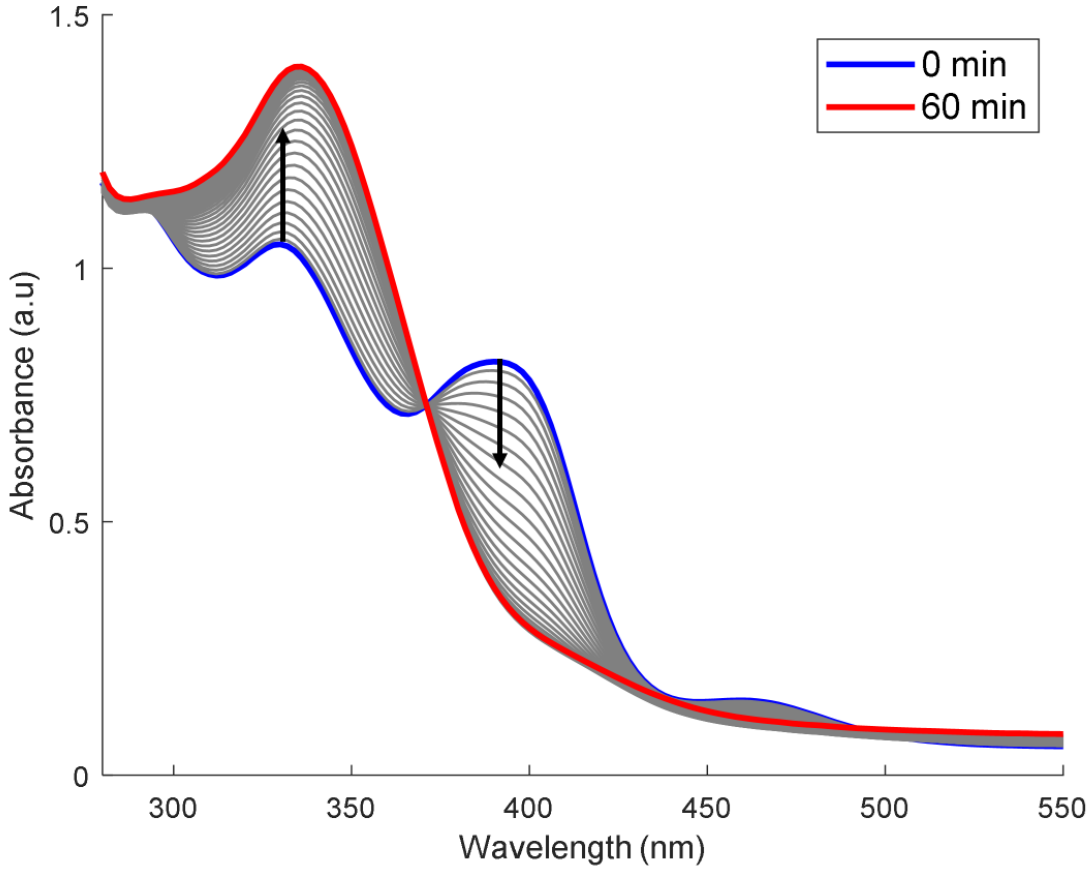

Figure 2.9. Time-dependent UV-Vis spectra of 2-5 in 1x PBS (pH 7.4, 134 mM NaCl) recorded over 1 hour at 25 °C.

Similar aqueous ligand-exchange behaviour was observed for **2-6**, exhibiting a maximum absorbance for the LMCT transition observed at 397 nm, and the exchange product displaying its maximum absorbance peak at 336 nm (**Figure 2.10**). The ligand-exchange process for this complex was slower than **2-5**, which is consistent with the NMR measurements. The LMCT absorbance from the parent species disappeared completely by the 3-hour time point. Due to solubility and precipitation difficulties, subsequent measurements were not collected. As observed in the time-based ^{19}F and

^{1}H NMR spectra, only one exchange event was observed in PBS (pH 7.4, 134 mM NaCl), attributed to the loss of chloride and the subsequent formation of the aquo species.

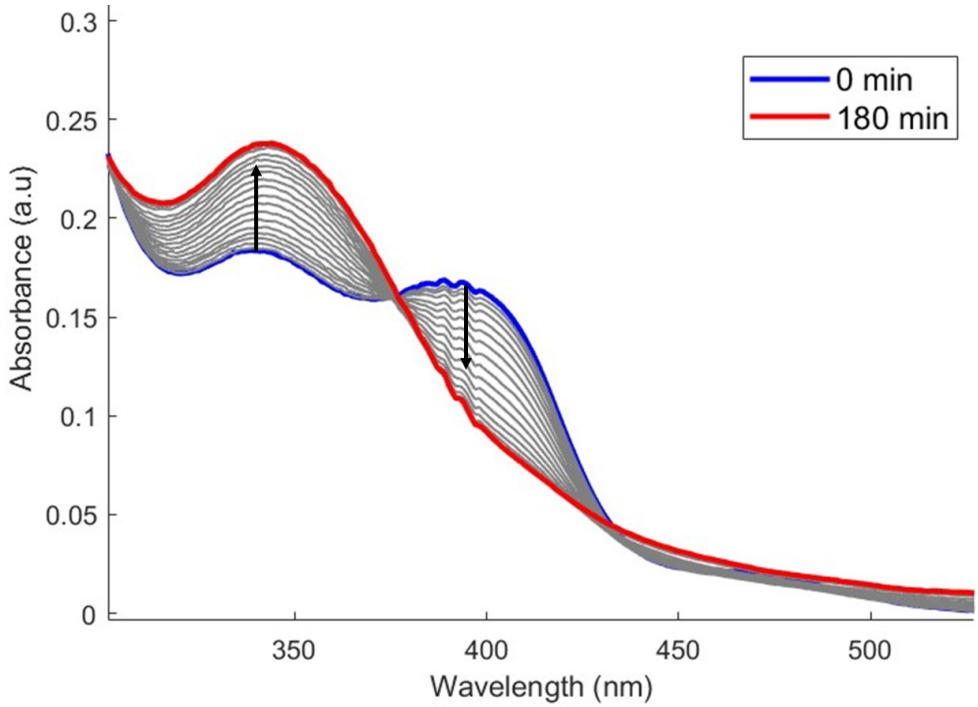

Figure 2.10. Time-dependent UV-Vis spectra of 2-6 in 1x PBS (pH 7.4, 134 mM NaCl) recorded over 3 hours at 25 °C.

The difference observed in the ligand-exchange behaviours of **2-5** and **2-6**, and their relative aqueous solution stabilities can be attributed to the molecular properties of the two complexes. Particularly, the crucial role that the axial ligands play in their stability and solution behaviour. As previously reported by the Walsby research group, the modification of Ru(III) complexes with CF_3 groups can have major effects on how the metal complexes behave in solution.[115] Fluorination of pharmaceuticals is generally associated with improved metabolic stability, increased lipophilicity and membrane permeability, and alteration of the chemical reactivity of drugs.[108] Comparing the aqueous solution stability of **2-5** and **2-6**, a slight differences in ligand-exchange behaviour is observed, which can potentially be attributed to the influence of the CF_3 ligand on the overall stability of the ligands surrounding the Ru(III) metal centre. In addition to slightly slower ligand-exchange, the appearance of precipitation in aqueous

solution was also delayed as a result, which can have a direct influence on the biological activity of the complex.

2.3.4. Fluorescence Quantum Yield (QY) Measurements

Fluorescence Quantum Yield (QY) is a measurement of the ratio of number of photons emitted to the number of photons absorbed by a molecule and is represented as a fraction of 1.0 or as a percentage. A QY value of 1.0 implies that for every photon absorbed by the molecule, a photon is emitted. To examine the fluorescence behaviour of the new Ru(III) compounds, absolute QY measurements were taken using an integrating sphere. Using the Fluoracle® software, the area under the emission peaks were compared and QY values for dansyl glycine, **2-3**, **2-5**, and **2-6** were calculated. Due to solubility and precipitation difficulties in aqueous solution, QY measurements of **2-4** were not collected. Since dansyl-based fluorophores are widely used as dyes in biological environments, dansyl glycine was chosen as a benchmark for the QY of the ruthenium complexes. As displayed in **Table 2.2**, in 1x PBS (pH 7.4, 134 mM NaCl), dansyl glycine exhibited a 13.36% QY. The observed quantum yield value for dansyl glycine is consistent with literature findings by Bramhall.[128] This molecule exhibits quantum yields ranging from as low as 7% to as high as 66% in aqueous media, depending on factors such as pH, temperature, and the presence of organic solvents.[128] The ligand, **2-3**, showed slightly higher QY values than dansyl glycine at 14.32%. The ruthenium complexes **2-5** and **2-6** displayed a 5.27% and 1.45% quantum yield value, respectively.

Table 2.2. Measured Quantum Yield values for dansyl glycine, 2-3, 2-5, and 2-6 in 1x PBS (pH 7.4, 134 mM NaCl, <1% Acetone) at 25 °C.

Compound Name	Quantum Yield (%)
Dansyl Glycine	13.36
2-3	14.32
2-4*	No Data
2-5	5.27
2-6	1.45

*Quantum Yield measurements of **2-4** were not collected due to precipitation/solubility difficulties in PBS.

The fluorescent properties and quantum yield of chemical species can be influenced by various factors including pH, inter/intramolecular interactions, solvent

effects, and temperature. In the case of the synthesized fluorophore, **2-3**, its attachment to the negatively charged ruthenium scaffold appears to supress its fluorescence quantum yield by a factor of 2.8. This reduction in fluorescence intensity may be attributed to a phenomenon known as the 'Paramagnetic Effect'. Paramagnetic fluorescence quenching can be a dynamic or static quenching phenomenon that occurs due to the interactions of a fluorophore with a negatively charged molecule.[129] The presence of the paramagnetic Ru(III) metal center can effectively quench the fluorescence emitted by the fluorophore ligand through either intramolecular or intermolecular interactions within the solution. The interactions between the excited fluorophore and the paramagnetic metal ion can lead to non-radiative relaxation pathways, causing the fluorophore to return to its ground state without emitting fluorescence, thereby suppressing the quantum yield of the complex.[129]

Additionally, the attachment of the trifluoromethyl benzyl moiety to the ruthenium complex further reduced the fluorescence quantum yield by a factor of 3.6. Though viable measurements of the fluorinated ligand, **2-4**, were not obtained due to solubility difficulties in aqueous solutions, the direct comparison of QY values of **2-5** and **2-6** can shed some light on the underlying causes of this quenching. The addition of the bulky and highly electron withdrawing benzyl-CF_3 group undoubtedly alters the electronic and steric properties of the ligand. These alterations can in turn lead to vibrational and rotational relaxation of the excited electron and decrease the fluorescent emission of the molecule through non-radiative pathways.[130] Although the synthesized ruthenium complexes, **2-5** and **2-6**, have notably small quantum yield values in phosphate buffered saline, their fluorescent properties could be vastly different when examined *in-vivo*/*in-vitro*, hence they still cannot be discounted as viable fluorescent spectroscopic probes.

2.3.5. Biological Testing

In-Vitro Cytotoxicity

The cytotoxic activity of the synthesized compounds was evaluated through a series of *in-vitro* studies using **2-3**, **2-4**, **2-5**, **2-6**, **NAMI**, and **Pyr-NAMI**. First, an MTT assay was performed on U2-OS (human osteosarcoma) epithelial cells to establish preliminary IC_{50} values for the compounds. Compounds were deemed inactive if their IC_{50} exceeded 100 μM, or if model fitting failed. Subsequently, human colorectal

carcinoma cells (HCT-116), epithelial liver cancer cells (Hep-3B), and non-cancerous lung fibroblast cells (MRC-5) were tested against the compounds and IC_{50} values were calculated from the dose response curves. **NAMI** and **Pyr-NAMI** were selected as positive controls. As depicted in **Table 2.3**, there was no evidence of anticancer activity observed with **NAMI** and **Pyr-NAMI** when tested against U2-OS and HCT-116 cell lines. These results align with findings of multiple studies reported in the literature.[44,131,132] Although **NAMI** exhibited some anticancer activity at concentrations exceeding 100 μM against MRC-5 cells, cytotoxicity at these higher concentration ranges was deemed insignificant.

Only the fluorinated organic ligand (**2-4**) and the fluorinated ruthenium-based complex (**2-6**) showed potency towards the cell lines tested, while no activity was observed from **2-3** and **2-5**. Literature reports indicate that the presence of electron-withdrawing $-CF_3$ groups can improve cytotoxicity through the enhancement of lipophilicity and increase of cellular uptake of ruthenium anticancer drugs.[115,133] As determined by computational Log*D* measurements, the fluorine functionalized compounds, **2-4** and **2-6**, are more lipophilic compared to **2-3** and **2-5**. This improved lipophilicity could aid in the passive diffusion of the molecules across the cell membrane, which could be a major contributing factor in the observed *in-vitro* activity of the compounds.

Table 2.3. Summary of IC50 results for the compounds against U2-OS (human osteosarcoma), HCT-116 (colorectal cancer), HEP-3B (liver cancer), and MRC-5 (healthy lung fibroblast) cell lines.

Compound	IC_{50} (μM): U2-OS	IC_{50} (μM): HCT-116	IC_{50} (μM): HEP-3B	IC_{50} (μM): MRC-5
NAMI	Inactive	Inactive	No Data*	117
Pyr-NAMI	Inactive	No Data*	No Data*	No Data*
2-3	Inactive	No Data*	No Data*	No Data*
2-4	Inactive	24.66	No Data*	38.96
2-5	Inactive	No Data*	No Data*	No Data*
2-6	35.03	8.44	3.89	14.11
Cisplatin**	NA	9.5-25.2	11.0-20.9	9.5-13.2

*Due to insolubility, assays were not run on these compounds.
**Literature reported IC_{50} values presented as a reported range based on multiple studies.[134–140]

Comparing the potency of **2-4** and **2-6**, we can see that coordination of the organic ligand to the Ru(III) scaffold results in a clearcut enhancement of activity against

both HCT-116 and MRC-5 cells. For HCT-116 cells, the IC_{50} of **2-6** (8.44 μM) is approximately threefold lower than that of **2-4** (24.66 μM). similarly, for MRC-5 cells, the IC_{50} of **2-6** (14.11 μM) is approximately threefold lower than that of **2-4** (38.96 μM). Importantly, the incorporation of **2-4** into the ruthenium complex resulted in greater potency against both cancer and non-cancer cells. As literature suggests, this improvement of activity could be attributed to multiple factors including: the improvement of cellular uptake upon attachment to Ru(III) complex, and the alteration of the mechanism of action in which the drug induces cell death. [8,37,44,49,50] Interestingly, potential selectivity is also observed when comparing the activity of **2-6** against both cancerous and non-cancerous cell lines. Although both **2-4** and **2-6** show decreased potency towards MRC-5 cell line, we can see that **2-6** maintains a more noticeable selectivity profile, with 70% more potency towards the cancerous HCT-116 cell line. Consistent with literature reports, the anticancer efficacy of the ruthenium complex is more pronounced towards the cancer cell lines as demonstrated by its lower IC_{50} values.[8,9,44,47]

The comparison of the cytotoxic potency of **2-6** against HCT-116, HEP-3B, and MRC-5 cell lines with the IC_{50} values of cisplatin reported in the literature reveals comparable activity. Against HCT-116 and HEP-3B cell lines, cisplatin exhibits IC_{50} values ranging from 9.2 to 25.2 μM, and 11.0 to 20.9 μM respectively.[134,135,138–140] In comparison to cisplatin, **2-6** displays higher potency in both cell lines, with a significant improvement against HEP-3B cells (3.89 μM). Moreover, IC_{50} values ranging from 9.5 to 13.2 μM have been reported for the activity of cisplatin towards the non-cancerous MRC-5 cell line.[136,137] Therefore, greater selectivity towards cancerous cells is also observed for **2-6**.[39,44,47]

Synergy Assay

Combination therapy utilizes a combined treatment using two or more therapeutic agents. This treatment strategy can potentially reduce drug resistance and provide enhanced therapeutic response when compared to monotherapy methods.[141] Thus, combination therapy has become a popular strategy in modern chemotherapy. The biologically active ruthenium complex **2-6** from the *in-vitro* cytotoxicity assays was examined in a synergy assay to assess its potential as a combination therapy candidate. The ruthenium compound (**2-6**, 2 μM) was tested against HCT-116 in absence, and in

conjunction with standard of care (SOC) agents. The SOC agents were also tested in monotherapy to assess their individual therapeutic response. Therapeutic response was presented as the fraction of cells affected by the treatment and the magnitude of synergy between the two compounds was presented as the Bliss Combination Index (CI). The magnitudes of CI for the combination therapy of **2-6** and the SOC agents are presented in **Table 2.4**. Generally, CI values of less than 1.0 indicate a synergistic relationship between the two compounds, with lower values suggesting greater synergy.

Synergistic effects were observed when cells were treated using **2-6** and Olaparib. Olaparib is an organic drug used to treat patients with advanced ovarian cancer. Olaparib induces apoptosis in cancer cells by inhibiting poly (ADP-ribose) polymerase, PARP, a family of proteins responsible for repairing single-strand breaks (SSB) in DNA.[142] Ruthenium(III) and (II) compounds, such as **NAMI-A** and **RAPTA-T**, have previously been explored in the literature for their function as PARP inhibitors.[143,144] The observed synergistic effects between Olaparib and **2-6** suggest that **2-6** may promote apoptosis either by enhancing processes that disrupt DNA repair mechanisms, or through direct inhibition of PARP. The observed antagonistic effects can have many implications including the two compounds' possible competition for the same biological target, resulting in a lower overall therapeutic effect.

Table 2.4. Results of the Synergy Assay of 2-6 (2 μM) against HCT-116 Cell line.

SOC Agent	SOC Agent Concentration	Bliss Combination Index	Bliss Verdict
Oxaliplatin	30 μM	1.75	Antagonistic
Paclitaxel	2 nM	2.08	Antagonistic
5-Fluorouracil	60 μM	1.26	Antagonistic
Olaparib	100 μM	0.50	Synergistic
AZD6783	25 μM	2.20	Antagonistic
Irinotecan	5 μM	1.09	Antagonistic

2.4. Conclusions

In this chapter, two novel fluorescent analogs of the Ru(III) anticancer compound **NAMI** were successfully synthesized through the incorporation of a modified dansyl ligand into the classic **NAMI** structure. One of the **NAMI** analogs was functionalized

using a trifluoromethyl benzyl moiety to investigate its effects on the water/octanol distribution coefficient (LogD), cell uptake and cytotoxicity of the molecule. Moreover, fluorination of the molecule had the additional goal of introducing a spectroscopic handle. The addition of the trifluoromethyl benzyl moiety significantly increased the lipophilicity of the ruthenium complex, with the calculated Log*D* value increasing from 4.92, in the non-fluorinated molecule, to 7.82 in the fluorinated ruthenium complex.

The quantum yield values of the synthesized ligands were measured in PBS to examine the potential of the ruthenium complexes as fluorescent probes. The ruthenium complex, **2-5**, exhibited a quantum yield value of 5.27%, whereas the fluorinated ruthenium complex, **2-6**, gave a quantum yield value of 1.45%. Although these values are low, the in-vivo quantum yield values of the molecules could be vastly different, due to interactions with biomolecules. Hence, the synthesized Ru(III) complexes cannot be discounted as possible fluorescent probes and this remains an on-going area of investigation.

Studies of the ligand-exchange properties of the ruthenium complexes in aqueous media via NMR and UV-Vis techniques gave insight into the likely physiological exchange behaviour of the complexes. These studies revealed that the hydrolysis of the chloride ligands begins almost immediately following aqueous dissolution. Moreover, the ligand-exchange products for both ruthenium complexes become the dominant species in solution within the first hour following dissolution. The fluorinated compound showed slower ligand-exchange rates with an equilibrium being reached after 300 minutes, whereas the non-fluorinated analog reached an exchange equilibrium within 90 minutes. In addition, ruthenium poly-oxo species were formed following ligand-exchange which was highlighted by the formation of green precipitates.

Biological studies of the synthesized Ru(III) complexes against various cell lines (U2-OS, HCT-116, HEP-3B, MRC-5) revealed valuable information regarding their possible mechanism of action, and their potential as anticancer drug candidates. While no cytotoxic activity was observed from the non-fluorinated ligand and ruthenium complex (**2-3** and **2-5** respectively), the fluorinated compounds (**2-4** and **2-6**) showed promising results in the growth inhibition of cancer cell lines. More specifically, the fluorinated Ru(III) complex, **2-6**, exhibited IC_{50} values of 35.03 μM (against U2-OS), 8.44 μM (against HCT-116), 3.89 μM (against HEP-4B), and 14.11 μM (against MRC-5).

These IC_{50} values are comparable to literature reported IC_{50} values of cisplatin. Notably, **2-6** showed selectivity when comparing its activity against cancer cell lines (HCT-116, HEP-3B) versus the non-cancerous MRC-5 cell line. Finally, it was determined through a synergy assay that **2-6** exhibits a synergistic relationship with Olaparib to induce growth inhibition of HCT-116 cells. This may suggest that the cytotoxic activity of **2-6** can be a result of the disruption of DNA repair mechanisms through the inhibition of PARP.

Overall, the experimental results in this chapter provide compelling evidence that the functionalization of Ru(III) **NAMI** compounds with lipophilic CF_3 groups enables the introduction of cytotoxicity into compounds previously known for their negligible impact on cell viability. This approach opens new avenues for the development of Ru(III) complexes as potent anticancer agents, challenging conventional perceptions and offering promising prospects for future research and therapeutic applications.

Chapter 3. Nanoparticle Encapsulation and Aptamer-coating of Novel Analogs of Ru (III) NAMI

3.1. Introduction

Nanomaterials (NMs) have been used extensively in pharmaceutical drug delivery, due to their biological safety, biodegradable nature, and facile synthetic procedures. One major advantage of utilizing nanoparticle systems for anticancer drug delivery is their ability to exploit the Enhanced Permeability and Retention (EPR) effect.[145] Due to their small size, prolonged physiological circulation times, and the leaky, permeable, and defective vascular formation, coupled with poor lymphatic drainage in tumor tissues, nanoparticles demonstrate enhanced accumulation within cancer tissue. Additionally, encapsulating labile anticancer agents in nanoparticles has been shown to prevent premature activation, alter physiological distribution, and effectively reduce off-target activity and associated side-effects.[87–89] Furthermore, nanoparticles have the capacity to encapsulate both hydrophilic and hydrophobic drugs, including those with poor water-solubility.[145] Finally, many tumors develop acquired resistance towards chemotherapeutics and consequently downregulate uptake mechanisms or excrete the anticancer agent.[146] Nanoparticle drug delivery systems can overcome this obstacle by introducing alternative drug entry mechanisms to the cells.[146]

Polymeric nanoparticles possess an advantage over other types of NP systems, such as lipid and inorganic nanoparticles, due to their high stability in biological media and the feasibility of large-scale manufacturing.[146] Furthermore, the surface modification of nanoparticles allows for the tunability of the circulation time, biological stability, and the introduction of active targeting to the nanoparticles.[145,147,148] Poly Lactide-co-Glycolide Acid (PLGA) is a copolymer that has been widely studied for the delivery of pharmaceuticals in cardiovascular therapy, chemotherapy, immunotherapy, neural disease therapy, and respiratory disease therapy (**Figure 3.1**).[145,146,149–152] PLGA's biosafety, biodegradability, and biocompatibility make it safe for use in humans and has led to its approval by the FDA for drug delivery. PLGA nanoparticles are metabolised *in vivo*, breaking down into lactic acid and glycolic acid which are natural biproducts of various metabolic processes. These components are further metabolised into non-toxic molecules, such as water and carbon dioxide, which are ultimately excreted naturally.[145]

In addition, polymeric nanoparticles are versatile delivery tools. The release kinetics of PLGA nanoparticles can be modified through various methods. These modifications include: adjusting the lactic to glycolic acid ratio, altering the polymer chain lengths, and the incorporation of hydrophilic polyethylene glycol (PEG) blocks—otherwise known as PEGylation—into the polymeric chains.[145] PEGylation is found to increase the systematic circulation times of the NP's by shielding the surface from aggregation, opsonization, and phagocytosis.[84] The PLGA-PEG co-polymer also allows for the attachment of targeting molecules to increase the *in-vitro* and *in-vivo* uptake of the encapsulated molecules. The attachment of antibodies and aptamers to acid-terminated PEG chains has been studied extensively with the aim of increasing nanoparticle uptake and drug delivery.[153–155]

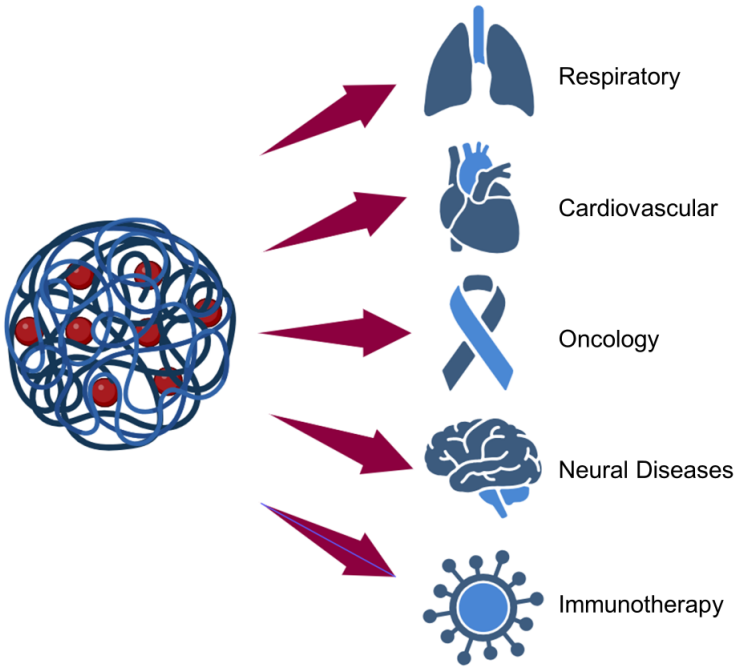

Figure 3.1. The versatility of PLGA nanoparticles in modern medicine.

Nucleolin (NCL) is a large protein that is found on cell-surfaces and in the nuclei of eukaryotic cells and is responsible for a multitude of functions related to cell growth, gene expression and regulation, and angiogenesis. Since cancer cells have elevated growth rates, they naturally have faster metabolism and an overexpression of the proteins responsible for these processes. AS1411 is a guanine rich aptamer that actively binds the RNA-binding domains of NCL and can be used to target cancer tissues.[156]

Successful delivery of organic and metal-based drugs through aptamer-functionalization using AS1411 has been reported in the literature.[79,155,157]

In this chapter, fluorinated and non-fluorinated analogs of the Ru(III) **NAMI**-type complexes that were synthesized in **Chapter 2** were encapsulated in aptamer-functionalized PLGA-PEG nanoparticles. To determine the optimal formulation for the encapsulation of the ruthenium compounds, a variety of drug-to-polymer formulations were explored. The optimal formulations, with the highest drug loading percentages, were used for biological testing to explore the effects of NP encapsulation on cell-uptake and cytotoxicity and study the relationship between ruthenium uptake and observed cytotoxicity. In addition, the drug release profile from the nanoparticles, size, and surface charge of the nanoparticle formulations was evaluated.

3.2. Experimental

3.2.1. Materials and Instrumentation

NH_2-PEG-COOH (3.4 kDa) was purchased from Biopharma PEG Scientific Inc. AS1411 aptamer and a non-specific aptamer were purchased from Integrated DNA Technologies Inc. PTFE syringe filters were purchased from Mandel Scientific Company Inc. All other reagents and materials were purchased from Sigma-Aldrich. Eppendorf 5415D and IEC Centra MP4R were used as the centrifuges for the syntheses. NMR Spectra were collected on a Bruker 600 NMR spectrometer. ICP-MS data were collected using a Thermo Scientific iCAP Qc ICP-MS and Qtegra software. Particle size and zeta potential measurements were performed using a Malvern Panalytical Zetasizer Nano ZS Size Analyzer. All Data/spectra can be found in **Appendix B**.

3.2.2. Synthesis

PLGA-PEG-COOH Co-polymer. Synthesis followed NHS/DCC protocols and literature procedures.[87,89,90,158,159] In a 50 mL round bottom flask, PLGA-COOH (7-17KDa, 300mg, 0.044 mmol) and N,N'-Dicyclohexylcarbodiimide (DCC) (455 mg, 2.21 mmol) were dissolved in chloroform (10 mL). The solution was stirred at room temperature for 5 min and N-hydroxy succinimide (NHS) (250 mg, 2.21 mmol) was added to the mixture and allowed to stir at room temperature for 6 h. The resulting

solution was reduced under vacuum, and then cold diethyl ether and cold methanol were added to precipitate the intermediate. The resulting white precipitate was centrifuged (6000 rpm, 15 min) and washed with cold methanol/diethyl ether three times to remove excess NHS/DCC. The precipitate was dissolved in chloroform (15 mL). To the mixture, NH_2-PEG-COOH (3.4 kDa, 150 mg, 0.044 mmol) and DIEA (100 µL, 0.44 mmol) dissolved in chloroform (5 mL) were added and the solution was allowed to stir at room temperature for 18 h. The solution was reduced under vacuum to ~5 mL and cold methanol was added to precipitate the co-polymer. The co-polymer was washed with cold methanol to remove excess PEG and centrifuged (6,000 rpm, 15 min) three times to separate the product. The final product, a white powder, was dried under vacuum and used for nanoparticle formulation without further purification. ^{1}H NMR (601 MHz, $CDCl_3$) δ 5.20 (m), 4.81 (s), 3.62 (s), 1.57 (s).

PLGA-PEG-AS1411. Synthesis followed NHS/EDC protocols and literature procedures.[18,158–161] In a 25 mL round bottom flask PLGA-PEG-COOH (100 mg, 0.0083 mmol) was dissolved in acetonitrile (10 mL) and EDC (120 mg, 0.77 mmol) was added to the solution. To the mixture NHS (90 mg, 0.77 mmol) dissolved in acetonitrile (0.5 mL) was added and the solution was allowed to stir at room temperature for 30 minutes. The solution was dried under vacuum and resuspended in methanol (10 mL) and centrifuged three times (6000 rpm, 15 min) and washed to removed excess NHS/EDC. The washed precipitate was dissolved in acetonitrile (10 mL) and AS1411 aptamer (234 µL, 1 mM) in formamide/acetonitrile (1:1, v/v) was added to the solution. The mixture was stirred at room temperature for 24 h. The resulting solution was dried under vacuum, resuspended in cold methanol and the resulting white precipitate was washed and centrifuged (6000 rpm, 15 min) three times. The washed product was dissolved in DCM and dried under vacuum to yield the final product. The final product, a white powder, was used to create the nanoparticle formulation without further purification. ^{1}H NMR (601 MHz, $CDCl_3$) δ 8.22 (s), 6.14 (s), 5.20 (m), 4.81 (s), 3.62 (s), 2.72 (m), 2.64 (m), 1.57 (s), 0.83 (m).

Nanoparticle Encapsulation of Na[RuCl$_4$(DSC-Pyr)(DMSO)]. Synthesis of the NP formulations was achieved following literature procedures.[87–89] In a 10 mL scintillation vial, Pluronic F-127 surfactant (0.1% w/v, 5 mL) was placed. To the surfactant solution, **2-5** (5 mg) and PLGA-PEG-COOH (10 mg) in a solution of acetone:

DCM (39:1, v/v, 2mL) was added in a dropwise manner under stirring. The mixture was stirred at room temperature for 30 min. The NP solution was filtered using a 0.45 μm PTFE syringe filter. The organic solvent was then removed under vacuum. The resulting milky nanoparticle solution was centrifuged (11,000 rpm, 10 min) and washed three times with deionized water to remove unencapsulated complex and free surfactant. The resulting pellet was frozen and dried by lyophilization and used in subsequent experiments without further purification.

Nanoparticle Encapsulation of Na[RuCl$_4$(Benzyl-CF$_3$-DSC-Pyr)(DMSO)]. Synthesis of the NP formulations were achieved following literature procedures.[87–89] In a 10 mL scintillation vial, Pluronic F-127 surfactant (0.1% w/v, 5 mL) was placed. To the surfactant solution, **2-6** (5 mg) and PLGA-PEG-COOH (10 mg) in a solution of acetone: DCM (39:1, v/v, 2mL) was added in a dropwise manner under stirring. The mixture was stirred at room temperature for 30 min. The NP solution was filtered using a 0.45 μm PTFE syringe filter. The organic solvent was removed under vacuum. The resulting milky nanoparticle solution was centrifuged (11,000 rpm, 10 min) and washed three times with deionized water to remove unencapsulated complex and free surfactant. The resulting pellet was frozen and dried by lyophilization and used in subsequent experiments without further purification.

Conjugation of aptamers to NPs containing metal complexes. Aptamers were attached to the surface of complex-containing nanoparticles following NHS/EDC protocols and literature procedures.[18,95] MES buffer (pH 6.0, 500 mM NaCl) was added to a 10 mL scintillation vial containing nanoparticle formulation (10 mg/mL). To the nanoparticle suspension, 1-Ethyl-3-(3-dimethylaminopropyl) carbodiimide (EDC) (109 mg, 0.7 mmol) was added followed by the dropwise addition of NHS (160 mg, 1.4 mmol) dissolved in MES buffer (0.5 mL, pH 6.0, 500 mM NaCl). The mixture was allowed to stir at room temperature for 30 min. The suspension was centrifuged (11,000 rpm, 10 min) and washed with phosphate buffer (pH 8.0) three times to remove excess NHS and EDC. The washed pellet was resuspended in PB buffer (2 mL, pH 8.0). Aptamer suspended in deionized water (76 μL, 1mM) was added to the suspension and the solution was stirred overnight. The resulting solution was centrifuged (11,000 rpm, 10 mins) and washed with deionized water three times and the pellets were dried under lyophilization. The resulting aptamer conjugated nanoparticles were used for subsequent experiments without further purification.

3.2.3. Nanoparticle Encapsulation Studies

Nanoparticle Preparation

To examine the encapsulation efficiency and drug loading percentage inside the nanoparticles, a series of nanoparticle formulations with varying drug and polymer mass ratios were prepared and analyzed using a Thermo-Scientific iCAP Qc ICP-MS. Following literature nanoprecipitation methods, a series of nanoparticle samples were prepared using varying masses of **2-5** and **2-6** (1.25 mg, 2.5 mg, and 5 mg) and 10 mg of PEGylated and non-PEGylated PLGA-COOH.[87–89] Varying masses of **2-5** and **2-6**, and 10 mg of PEGylated or non-PEGylated PLGA-COOH were dissolved in acetone (1.95 mL) and DCM (0.05 mL). The solution was stirred until both the polymer and the complex were fully dissolved. The complex/polymer solution was added in a dropwise manner to a stirring solution of Pluronic F127 in water (0.2% w/v). The resulting milky suspension was stirred at room temperature for 30 minutes. The organic solvent was removed under vacuum and the remaining solution was filtered through 0.45 μm PTFE syringe filter. The nanoparticles were washed with deionized water and centrifuged (11,000 rpm, 15 min) to remove unencapsulated drug and remaining surfactant. The resulting nanoparticles were suspended in deionized water, transferred to scintillation vials, flash frozen in liquid nitrogen, and lyophilized. The recovered mass was weighed and the resulting solid nanoparticle samples were digested for analysis.

Nanoparticle Acid Digestion

A stir bar, 3 mL of HNO_3 (70% w/w, UltraPure for trace analysis, Avantor J.T Baker®), and 2 mL of H_2O_2 (30% w/w, PlasmaPure for trace analysis, Sigma-Aldrich) were added to each scintillation vial containing the solid nanoparticle samples. The solutions were stirred overnight at room temperature. Following the acid digestion, the solutions were quantitatively transferred to acid-washed 10 mL volumetric flasks and diluted to mark with 2% ultrapure nitric acid solution.

Analysis by Inductively Coupled Plasma – Mass Spectrometry

ICP-MS was performed on a Thermo Scientific iCAP Qc ICP-MS equipped with an aqueous liquid sample introduction autosampler, and the Qtegra analysis software. Argon flow was set to 0.3 mL/min. Ruthenium-102 was detected in KED mode with helium as the gas flowing into the collision cell. 1 mL injection volumes were used with

simultaneous detection of Rh and In from a 10.0 ppb internal standard. Detected values of ruthenium-102 were determined using a calibration curve created from ruthenium standards of 0.1, 1.0, 10.0, 100.0, and 500.0 ppb prepared in ultrapure nitric acid (2% w/w). Raw data was collected with Qtegra analysis software, imported into Microsoft Excel for processing and the ruthenium content of each formulation was determined using the calibration curve.

3.2.4. Drug Release Studies

Drug release studies were conducted at 37 °C over 72 hours following modified literature procedures reported by Jusu and co-workers.[162] Triplicate nanoparticle formulations using PLGA-PEG-COOH encapsulated **2-5** and **2-6** were prepared, lyophilized, and the post lyophilization masses were recorded. The optimal formulation of 10 mg of polymeric nanoparticle, and 5 mg of the ruthenium drugs was used. The lyophilized samples were suspended in PBS (pH 7.4, 0.2% PF-127 surfactant) to give a 1 mg/mL solution and placed in 15 mL falcon tubes. The tubes containing the nanoparticle suspensions were placed in an orbital shaker at 37 °C rotating at 100 rpm. At various timepoints during the 72-hour period the falcon tubes were removed from the shaker and centrifuged (6500 rpm, 15 minutes), 1 mL sample of the supernatant was removed and replaced by 1 mL of fresh buffer. The nanoparticles were agitated to ensure complete resuspension following sampling, and the falcon tubes were placed back in the shaker. 100 µL aliquots of the 1 mL samples were diluted to mark in 10 mL volumetric flasks using ultrapure nitric acid (2% w/w). The amount of ruthenium released was determined by ICP-MS and reported as the cumulative percentage of ruthenium relative to the total amount of encapsulated ruthenium in the formulations. To visualize the release profile of the drugs from the NPs, GraphPad Prism 8 software (GraphPad Software Inc., La Jolla, CA, USA) was used to generate a kinetic model.

3.2.5. Particle Size and Zeta Potential Measurements

The size, and the surface charge of the nanoparticle formulations were measured via dynamic light scattering and zeta potential measurements on a Malvern Zetasizer Nano-ZS (Malvern Panalytical Ltd, Malvern, UK). Triplicate formulations of empty PLGA-PEG-COOH NPs, **2-5** and **2-6** encapsulated PLGA-PEG-COOH NPs, and **2-5** and **2-6** encapsulated PLGA-PEG AS1411-coated NPs were prepared using the optimal

formulation. The samples were suspended in deionized water and placed in DTS1070 folded capillary cells (Malvern Panalytical Ltd, Malvern, UK). DLS measurements were taken using a 60 sec equilibrium time, scatter angle of 173°, measurement position of 5.50 mm, with the number of runs set to 'automatic'. Zeta potential measurements were taken at room temperature using the Smoluchowski model, equilibrium time of 60 sec, and the number of scans set to automatic.

3.2.6. Cellular Uptake Studies*

For intracellular ruthenium determination, 1 x 10^6 HCT116 cells were seeded per well in 6-well plates. Prior to treatment, NP formulations were prepared using 10mg of polymer and 5 mg of **2-5** and **2-6**, and the NP formulations were passed through 0.8 µm sterile PTFE syringe filters (Cobetter, Xiaoshan District, China) to remove precipitates. After 24 hours, monolayers were treated with 20 µM of unencapsulated **2-5** and **2-6** and NP formulations (with equivalent **2-5**/**2-6** concentrations) in triplicates and incubated for 24 hours. Cells were washed three times with Hank's Balanced Buffer Solution (HBSS, Thermo Fisher) and detached using 0.25% trypsin solution (Thermo Fisher), and 5 x 10^5 cells of each condition were pelleted. The resulting pellets were digested using 1 mL of HNO_3 (70% w/w, UltraPure for trace analysis, Avantor J.T Baker®) and 200 µL of H_2O_2 (30% w/w, PlasmaPure for trace analysis, Sigma-Aldrich) for 24 hours. Ruthenium standard solutions were prepared ranging from 0.1 ppb to 500 ppb using ruthenium atomic absorption standard solution (Sigma-Aldrich). 0.5 mL of each digestion solution was diluted to 10 mL in acid-washed volumetric flasks using 2% ultrapure HNO_3 in Milli-Q® H_2O. The results were visualized using GraphPad Prism 8.0 software (GraphPad Software Inc., La Jolla, CA, USA). Statistical significance was calculated using a two-way ANOVA with p-value <0.05 considered to be statistically significant.

3.2.7. *In Vitro* Cell Cytotoxicity Studies*

A549 (2000 cells/well) and HCT116 (1500 cells/well) cells were purchased from ATCC and maintained at 37 °C with 5% CO_2 in DMED (Gibco) and supplemented with

*Cytotoxicity assays, and cell uptake seeding, incubation, and pellet preparations were performed by Devon Heroux under the supervision of Marcel Bally at the BC Cancer Agency, 686 West Broadway, Suite 500, Vancouver, BC, Canada, V5Z 1G1.

10% FBP (Gibco) and 2 mM L-glutamine (Gibco). Cells were seeded in a 384-well black-walled, clear bottom plate (Greiner Bio-one, Monroe, NC, USA) in a volume of 50 µL/well. Prior to treating the wells, NP formulations were prepared using 10 mg of polymer and 5 mg of **2-5** and **2-6,** and the NP formulations were passed through 0.8 µm sterile PTFE syringe filters (Cobetter, Xiaoshan District, China) to remove precipitates. After 24 hours post seeding, the wells were treated with 0 to 100 µM (equivalent **2-5** and **2-6** concentrations) of NP formulations. At 72 hours post-treatment, cells were stained with 4.87 µM Hoechst 33342 (Life Technologies, Carlsbad, CA, USA) and 312.5 nM ethidium homodimer I ((Biotium, Hayward, CA, USA). The cells were incubated with the dyes for 20 minutes at 37 °C, 5% CO_2, and the plates were imaged using an IN-Cell Analyzer 2200 (GE Healthcare, Mississauga, ON, Canada) that uses an automated fluorescence microscope platform for high content screening. Cell counts were determined using the Developer Toolbox 1.9 software (GE Healthcare), and percentages of viable cells were normalized to vehicle controls and expressed as the fraction affected. All data was plotted using Prism 8.0 software (GraphPad Software Inc., La Jolla, CA, USA).

3.3. Results and Discussion

3.3.1. Formulation Optimization and NP Characterization

The initial synthetic plan for this chapter was to directly conjugate the amine-terminated aptamer to the acid terminated PLGA nanoparticles. However, due to numerous unsuccessful attempts, the focus was shifted towards using a PLGA-PEG copolymer. The conjugation of the aptamer to nanoparticles is performed in aqueous media. Previous literature reports indicate that in aqueous environments, carboxylic acid-terminated PLGA polymers form hydrophobic cores.[163] Moreover, it is possible that the carboxylic chains could be sequestered inside the nanoparticle core. Steric hinderance caused by the bulky nanoparticle core could then prevent successful attachment of the aptamer to the PLGA nanoparticles. This is exacerbated by the 2% molar ratio of the aptamer with respect to the nanoparticles. In contrast, the PEG polymers are hydrophilic and form on the outside of the nanoparticle, providing a more accessible site for the attachment of the aptamer.

In addition to the challenges encountered with the conjugation of the aptamer to the nanoparticles, the confirmation of the conjugation using literature methods appeared to be ineffective. Many of the confirmation methods outlined in the literature rely on the use of polyacrylamide gel electrophoresis (PAGE), with the expectation of observing a visible band indicating the attachment of aptamer to the NPs.[79,89] However, despite following these procedures, no such band corresponding to the apt-NP structure was observed. Extensive literature research revealed that due to the spherical nature of the nanoparticles, they may not penetrate and pass through the UREA gel, thus potentially being washed away. Consequently, NMR techniques were employed instead of gel electrophoresis to confirm the attachment of the aptamer to the nanoparticles.[164] **Figure 3.2** illustrates the changes in the ^{1}H NMR following the formation of the co-polymer, and the conjugation of the aptamer to the nanoparticles respectively.

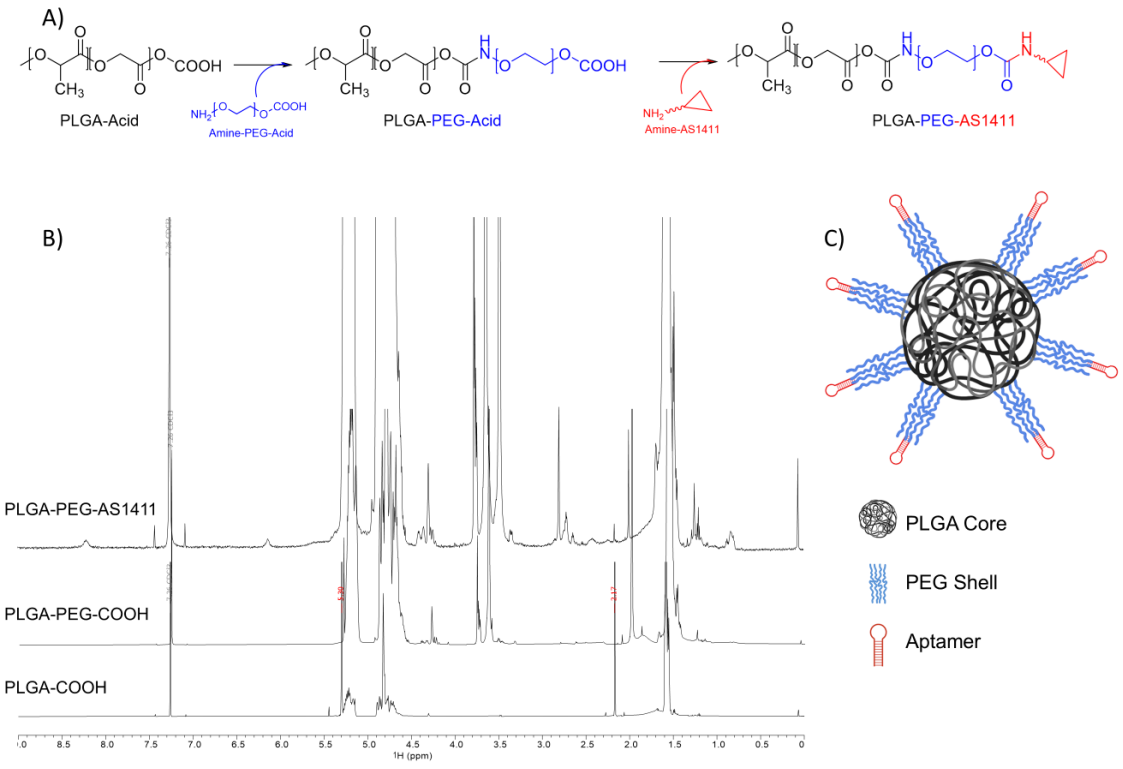

Figure 3.2. A) The synthetic scheme for the PLGA-PEG-COOH copolymer, and the conjugation of AS1411 aptamer to the NPs. B) The change in the ^{1}H NMR spectrum (601 MHz, $CDCl_3$) upon the addition of PEG, and the aptamer. C) The structural representation of the PLGA-PEG-AS1411 triblock.

Importantly, the incorporation of PEG into the nanoparticle structure can offer several advantages, including enhanced stability of the nanoparticles, prolonged circulation times *in-vivo*, and the prevention of nanoparticle aggregation in solution.[165] To synthesize the copolymer, acid-terminated PLGA, and acid- and amine-terminated PEG were utilized. The most common strategy reported in the literature for synthesizing the PLGA-PEG copolymer is through amide coupling reactions since the amide bonds formed are quite stable in physiological conditions. The subsequent conjugation of the aptamer to the copolymer also followed established amide bond coupling procedures described in the literature.[79,88,166]

In nanoparticle drug delivery, achieving higher drug loading is considered advantageous as it allows for an increased therapeutic effect, smaller drug dosages, and reduced frequency of drug administration. To identify the most optimal nanoparticle formulation, a series of nanoparticle samples were prepared for **2-5** and **2-6** through the nanoprecipitation method. Various parameters in nanoprecipitation could influence the particle size, surface charge, drug loading percentage, and encapsulation efficiency of the resulting nanoparticles. These parameters include, the choice of surfactant, surfactant concentration, solvent choice, drop rate, and stirring speed. The effects of these parameters on the PLGA nanoencapsulation of **KP1019** was investigated by Keppler *et. al.*[89] From this report, the optimal organic solvent mixture of 1.95 mL acetone and 0.05 mL DCM was used to dissolve the ruthenium compounds and the PLGA-PEG-COOH polymer prior to addition to the surfactant mixture for nanoprecipitation.

Initially, Tween-80 (Polysorbate 80) was used as the surfactant, however, rapid colour change, marked by the formation of green precipitates was observed with both Ru(III) compounds which indicates the reduction of the ruthenium complex. A similar change in color was observed in the report by Keppler and co-workers.[89] This study revealed that the reduction of the ruthenium metal center is possible by Tween-80 through an oxidation reaction involving the surfactant. This change in color was not observed when Pluronic PF-127 was used as the surfactant. To streamline the process, previously established parameters for Ru(III) nanoencapsulation reported by Keppler *et. al.* were adopted, with modifications limited to polymer-to-drug-mass ratio.[89] The resulting formulations used 10 mg of polymer, and the mass of **2-5** and **2-6** were varied. The results of these experiments are summarized in **Table 3.1**.

Table 3.1. Recovered Mass (RM), Encapsulation Efficiency (EE), and Drug Loading (DL) for PLGA-PEG NP formulations with varying masses of 2-5 and 2-6 and 10 mg polymer mass determined by ICP-MS following acid digestion.

	2-5			2-6		
Mass of Drug	1.25 mg	2.50 mg	5.00 mg	1.25 mg	2.50 mg	5.00 mg
RM (%)	22 ± 15	15 ± 5	28 ± 8	27 ± 3	42 ± 7	36 ± 6
EE (%)	3.3 ± 0.7	1.7 ± 0.5	2.3 ± 0.2	2.8 ± 0.5	3.1 ± 0.2	3.7 ± 0.5
DL (%)	0.4 ± 0.1	0.4 ± 0.1	1.2 ± 0.1	0.3 ± 0.1	0.8 ± 0.1	3.4 ± 0.3

*Errors are represented as ± the standard deviation of three replicate samples for each formulation

As discussed above, drug loading was used as a point of reference to assess the performance of each formulation. Drug loading (DL) is determined by comparing the total mass of the ruthenium complex detected by ICP-MS to the total mass of material recovered after nanoencapsulation. Higher drug loading percentages were observed in the 5 mg loading formulation for both ruthenium complexes. Lower overall drug loading, and encapsulation efficiencies were observed for the non-fluorinated complex, **2-5**. Encapsulation efficiency (EE), which is described by comparing the mass of ruthenium complex in the formulation (determined by ICP-MS) versus the initial ruthenium drug mass, was also calculated for both complexes. Lower encapsulation efficiency and drug loading observed with **2-5** is likely related to the nature of the polymeric nanoparticles.

As discussed above, the PLGA-PEG copolymer assembly by nanoprecipitation in aqueous media results in the creation of a hydrophobic core, comprised of the PLGA block, with the hydrophilic PEG chains facing outwards.[165] This characteristic of the nanoparticles promotes the encapsulation of more lipophilic compounds like **2-6**. Comparing the drug loading and encapsulation efficiency values to the reported literature values by Keppler and co-workers significantly smaller values were achieved.[89] However, the DL and EE values reported in this earlier study are likely exaggerated as unencapsulated ruthenium drug was not removed from solution by centrifugation or filtration techniques prior to analysis. Moreover, during the synthesis of the NP formulations of **2-5** and **2-6**, syringe filtration was performed to remove nanoparticle aggregates, which may reduce the nanoparticle concentration in the filtrate leading to lower recovered mass in our study.

Using the optimal formulations for both ruthenium complexes (using both aptamer-functionalized and non-functionalized PLGA-PEG NPs), particle size distribution and surface charge data were collected via dynamic light scattering (DLS) and zeta-potential measurements. Empty PLGA-PEG-COOH and PLGA-PEG-AS1411 nanoparticles were used as control samples. The size distribution, and zeta potential data are presented in **Table 3.2**. In addition, the polydispersity index (PDI), also known as the heterogeneity index is reported. This value is calculated using **Equation 3.1**:

$$PDI = \left(\frac{\sigma}{2a}\right)^2 \qquad \textit{Equation 3.1}$$

where σ is the standard deviation of the particle diameter and a is the mean particle diameter. PDI serves as a numerical representation of the distribution of size populations within a given sample. PDI values can range from 0.0, indicating a perfectly uniform size population in the sample, to 1.0, which signifies a highly polydisperse sample with multiple size populations.[167] In drug delivery applications, PDI values below 0.2 are generally considered acceptable for polymeric nanoparticles.[167]

Table 3.2. Surface charge (zeta potential), Average particle diameter (nm) and associated polydispersity index (PDI) of drug encapsulated, and empty nanoparticles using AS1411-functionalized, and non-functionalized PLGA-PEG. (Size distribution graphs are displayed in appendix B)

Nanoparticle Type	Encapsulated Drug	Average Particle diameter (nm)	PDI	Zeta Potential (mV)
PLGA-PEG-COOH	None	140± 50	0.117	-36 ± 7
PLGA-PEG-AS1411	None	160 ± 60	0.101	-45 ± 6
PLGA-PEG-COOH	2-5	160 ± 60	0.098	-26 ± 7
PLGA-PEG-COOH	2-6	160 ± 70	0.183	-29 ± 7
PLGA-PEG-AS1411	2-5	150 ± 50	0.076	-28 ± 7
PLGA-PEG-AS1411	2-6	140 ± 40	0.097	-31 ± 8

*Average particle size and zeta potential were measured from triplicate samples at 25 °C in D.I water (pH 7.4).

As discussed in **Chapter 1**, the defective and leaky nature of cancer tissue allows for the utilization of the EPR effect in targeting and accumulation of pharmaceuticals in these tissues. While the optimal nanoparticle size can vary significantly depending on factors such as the route of administration and the specific

target tissue, nanoparticles with a diameter of 100-200 nm are generally desired and show optimal accumulation in tumor tissue through the EPR effect.[85,167]

The 5 mg nanoparticle formulation of both ruthenium compounds displayed average particle diameters under 200 nm with a polydispersity index of less than 0.2. The aptamer-conjugated nanoparticles showed consistently smaller PDI values, indicating a homogeneous particle size distribution. Although aptamer conjugation caused a slight decrease in the average diameter of the nanoparticle formulations, the average diameter for all formulations falls within a similar range because of the standard deviation values.

In addition to particle diameter, the zeta potentials (ζ) of the nanoparticle formulations were measured to assess surface charge and colloidal stability in solution. The magnitude of zeta potential is directly related to the degree of electrostatic repulsion between neighbouring nanoparticles. The greater this value, the higher the electrostatic repulsion forces between the nanoparticles, resulting in a lower chance of aggregation, which indicates colloidal stability.[168]

The measured zeta potential values presented in **Table 3.2** clearly demonstrate that higher colloidal stability is achieved upon the conjugation of aptamers to the nanoparticle surfaces. The surface decoration of the NPs with AS1411 led to a considerable increase in the zeta potential of the empty NPs, from -36 ± 7 mv to -45 ± 6 mv. Moreover, the non-functionalized NPs of these compounds showed ζ values -26 ± 7 mv (**2-5**) and -29 ± 7 mv (**2-6**), while the aptamer-functionalized NPs of **2-5** and **2-6** exhibited ζ values of -31 ± 8 mv and 28 ± 7 mv respectively. On average, a 10% increase in the surface charge of the resulting particles is observed for drugs encapsulated in NPs functionalized with AS1411. This increase in surface charge can be attributed to the negatively charged phosphate backbone present in the aptamer structure.

Relating these findings to the observed particle diameter sizes, it becomes evident that non-functionalized drug-containing NPs exhibited slightly higher average particle diameters. This difference in particle diameter could be caused by the lower colloidal stability of the non-functionalized particles, leading to agglomeration and aggregation of the NPs in solution.

3.3.2. Drug Release Studies

While particle size, drug loading, and encapsulation efficiencies are crucial considerations in nanoparticle-based delivery of pharmaceuticals, the release rate of the drugs from these nanoparticles holds equal significance. One of the key advantages of nanoparticle drug delivery systems lies in their ability to control the release of drugs that might otherwise be rapidly cleared from the system. This facilitates drug delivery to tissues that would otherwise be inaccessible, extending the circulation time of the drug within the system, and potentially increases cell uptake and the overall therapeutic effect.[169] To study the release behaviour of **2-5** and **2-6** from PLGA-PEG nanoparticles, triplicate samples of the optimal formulations of each drug were suspended in PBS to give a final concentration of 1 mg/mL. The solutions were incubated at 37 °C, and at various time points centrifuged and the supernatant was analyzed via ICP-MS to determine total Ru content. The resulting release profiles of **2-5** and **2-6** are presented in **Figure 3.3** and **Figure 3.4** as the cumulative percentage of complex released with respect to the total drug loading.

In nanoparticle drug delivery, there are three dominating mechanisms of drug release from the NPs. These mechanisms include diffusion, solvent penetration, and polymer erosion.[170] The internal diffusion of the drug to the surface of the NPs is the most common release mechanism and it is highly dependent on the concentration of the drug in the release media.[170] Erosion is dependent on the stability and degradation kinetics of the nanomaterial.[170] Lastly, solvent penetration mechanisms are influenced by the solvent type, and the permeability of the polymer used.[170] Examining the release behaviour of both compounds in PLGA-PEG nanoparticles, an initial release 'burst' was observed in the first 10 hours. In this initial release period, approximately 33.5% and 32.2% of total encapsulated **2-5** and **2-6** were released from the nanoparticles, respectively. The initial burst release of the drug out of the nanoparticles is consistent with findings of Lippard *et. al.* where an initial 20% release of cisplatin from PLGA-PEG NPs was observed.[88] Following the initial release of the drugs from the nanoparticles, a slower prolonged release period was observed over a 72-hour period.

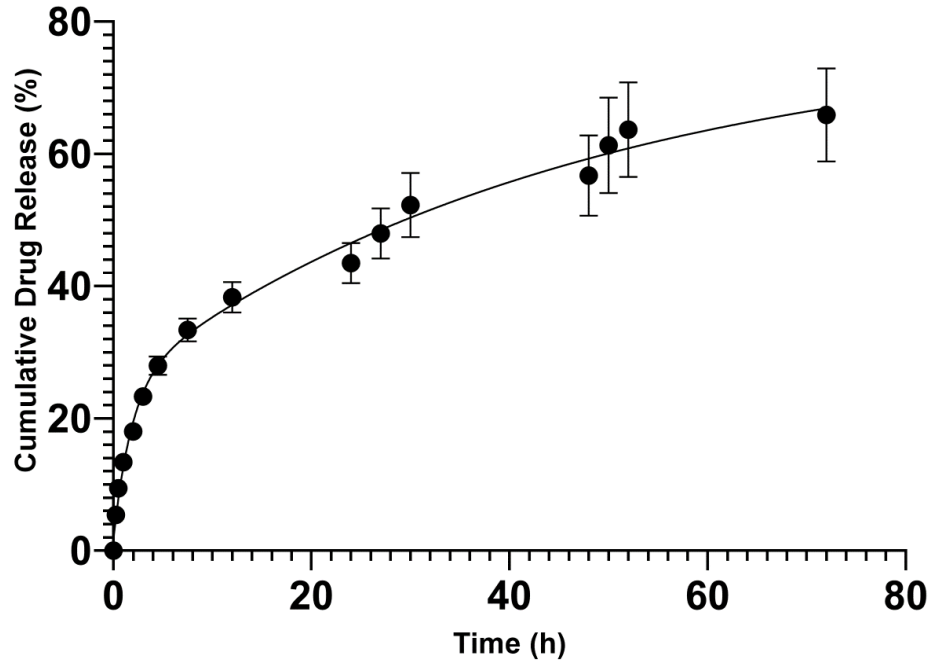

Figure 3.3. **Cumulative Release (%) of 2-5 from PLGA-PEG Nanoparticles over 72h in 1xPBS (pH 7.4, 0.2% PF-127, 134 mM NaCl) at 37 °C. Some error bars are hidden behind the data points.**

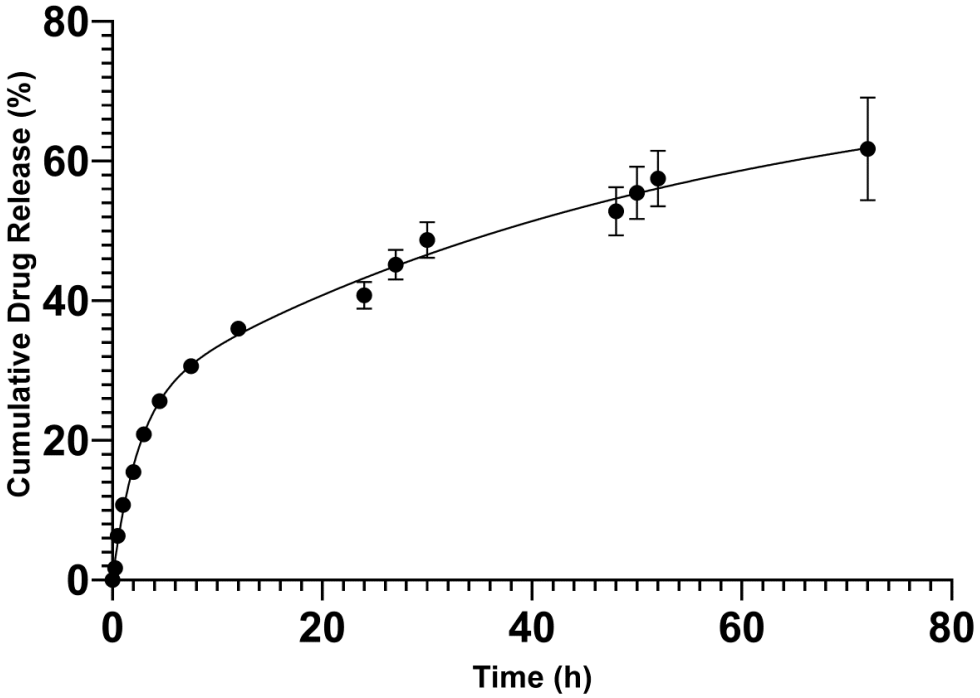

Figure 3.4. **Cumulative Release (%) of 2-6 from PLGA-PEG Nanoparticles over 72h in 1xPBS (pH 7.4, 0.2% PF-127, 134 mM NaCl) at 37 °C. Some error bars are hidden behind the data points.**

Due to the potential non-uniform encapsulation of ruthenium complexes within the polymeric nanoparticles, some of the encapsulated drug may be located near the outer surface of the NPs rather than being uniformly distributed in the nanoparticle core. Consequently, the release of these molecules may be more favored, leading to their rapid diffusion and the occurrence of an initial burst-release. Conversely, the encapsulated drug located at the core of the NPs is expected to exhibit a more gradual rate of release. Mechanisms such as polymer erosion, and solvent permeability can contribute to the slower release rates observed at later time points of the experiment. Considering these release mechanisms, the overall drug release from the NPs can be described by **Equation 3.2**:

$$\frac{d[Ru(sol)]}{dt} = k_1[Ru(sol)] + k_2[Ru(sol)] \qquad \textit{Equation 3.2}$$

where, k_1 and k_2 are rate-constants for the slow and the fast mechanisms of drug release, respectively. To expand on this idea and further examine the release behaviour of the drug from the PLGA-PEG NPs, a two-phase exponential growth model was utilized to analyze the cumulative release data and extract the rate constants. The release kinetics can be described by the following equation:

$$\%\ Release = S_{fast}\left(1 - e^{-k_{fast}t}\right) + S_{slow}\left(1 - e^{-k_{slow}t}\right) \qquad \textit{Equation 3.3}$$

Where, k_{fast} and k_{slow} are the rate constants governing the burst and prolonged drug release processes, respectively, while S_{fast} and S_{slow} represent the range over which the drug release occurs during the experiment. The release kinetic parameters of the ruthenium compounds from PLGA-PEG NPs are presented in **Table 3.3**.

Table 3.3. Release rate constants (min^{-1}) for 2-5 and 2-6 from PLGA-PEG nanoparticles, extracted from model fitting using equation 3.2. Maximum drug release percentage is presented as the plateau (%).

Compound	k_{fast} (min^{-1})	k_{slow} (min^{-1})	Theoretical Plateau (%)
2-5	0.658	0.0233	76.5
2-6	0.428	0.0189	74.5

Comparing the k_{fast} and k_{slow} values for **2-5** and **2-6**, it is evident that **2-5** has a faster overall rate of release from the PLGA-PEG nanoparticles. Conversely, the difference between the initial burst release of the two drugs is minor, with both

compounds exhibiting cumulative drug release values of ~30% within the first 10 hours (**Figure 3.3** and **Figure 3.4**). This observation can be attributed to the hydrophobic nature of the PLGA nanoparticle core, where rapid release of the more hydrophilic drug, **2-5,** is favored. The plateau values of 76.5% and 74.5% suggest that a similar maximum cumulative release of **2-5** and **2-6** will be achieved in vitro. Moreover, the release of hydrophilic molecules from PLGA NPs is enhanced by the porous nature of the polymeric nanoparticles, allowing for the penetration of water into the nanoparticles and facilitating the release of drug embedded on the outer surface of the NPs.[171]

The observed release profile of the drugs from the nanoparticles *in-vitro* underscores the potential of polymeric nanoparticles as effective delivery vehicles for ruthenium-based anticancer agents. The relatively prolonged release profile of both drugs suggests the feasibility of achieving a sustained therapeutic effect, mitigating potential issues associated with administering a large dose of the drug at once. Such issues may include heightened off-target activity, elevated side-effects, rapid clearance from the system, and premature drug activation.

3.3.3. Cell Studies

In-Vitro Cytotoxicity

To examine the influence of nanoparticle encapsulation on the antiproliferative activity of the synthesized **NAMI** analogs, *In-vitro* cytotoxicity assays against A549 (breast cancer) and HCT-116 (colorectal cancer) cell lines were conducted. A series of nanoparticle samples were prepared using the optimal formulation determined through the ICP-MS experiments. Aptamer-functionalized and non-functionalized nanoparticles, along with unencapsulated **2-5** and **2-6** were tested against the two cancer cell lines at concentrations ranging from 100 μM to 0.1 μM, and the fraction of live cells were determined to assess the antiproliferative activity of each sample against the cell lines. Surprisingly, the nanoparticle encapsulated **NAMI** analogs showed no notable cytotoxic behaviour *in-vitro*, and no IC_{50} values for these samples was extracted. Conversely, promising results were observed for the unencapsulated drugs. The dose response curves presented in **Figure 3.5** display the cytotoxic profile of the **NAMI** analogs against A549 and HCT116 cancer cell lines as the fraction of cells affected versus drug concentration.

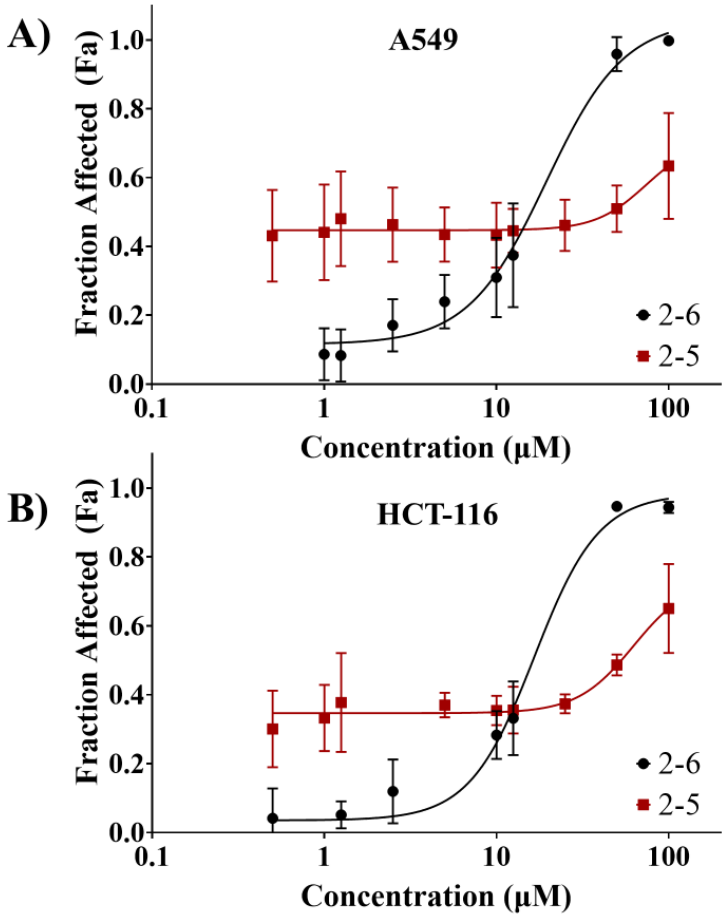

*The error bars represent the standard deviation in dose response recorded from 4 sample replicate measurements.

Figure 3.5. The dose response curves of the NAMI analogs resulted from recording the number of viable cells after 72 hours of incubation using 0.5 to 100 µM concentrations of the drugs. A) The dose response curves of 2-5 and 2-6 against A549 (Breast cancer) cell line, IC_{50} 2-5 = 77 ± 7 µM, IC_{50} 2-6 = 19 ± 2 µM. B) The doser-response curve of 2-5 and 2-6 against HCT-116 (colorectal cancer) cell line, IC_{50} 2-5 = 63 ± 5 µM , IC_{50} 2-6 = 16 ± 4 µM.

Both ruthenium complexes showed higher activity towards HCT-116 cancer cells, with the benzyl-CF_3 functionalized complex showing consistently higher activity, perhaps due to its more desirable lipophilicity profile. The observed IC_{50} values of **2-6** against HCT-116 cells (16 ± 4 µM) and A549 cells (19 ± 2 µM) are of the same order of magnitude observed with other cancer cell lines in **Chapter 2** and are comparable to the IC_{50} values of cisplatin reported in the literature.[137–140] The *in-vitro* activity of **2-6** indicates its potential as a ruthenium-based chemotherapeutic agent and opens the discussion for

further exploration of **NAMI** type complexes as not only antimetastatic agents, but potential antiproliferative agents.

Compound **2-5** displayed lower cytotoxicity than **2-6,** with IC_{50} values of 77 ± 7 μM and 63 ± 5 μM against A549 and HCT116, respectively. Interestingly, the dose response curve shape of **2-5** shows a biphasic curve with a wide horizontal response over the range of 0.5 to 25.0 μM. A mild cytotoxic response is observed in this range, with the effects increasing in concentrations above 25.0 μM. At higher concentrations, lower cellular responses are observed when compared to **2-6**. This could imply that the mechanisms by which **2-5** takes its effects, could be less damaging to the cancer cells than **2-6**. Alternatively, the mild fluorescence exhibited by **2-5** in quantum yield measurements, could be causing false positives in the flow cytometry measurements, leading to the flat dose-response curve observed at lower concentrations. Although no increase of cytotoxic response towards the cancer cells was observed with the nanoparticle encapsulations and aptamer functionalization of the drugs, further investigation of the cellular uptake of the drugs is necessary to explain these observations.

Cell-uptake

Although the relationship between cellular uptake of chemotherapeutic agents and their observed cytotoxic activity is quite complex, and influenced by a multitude of factors, higher activity is generally associated with higher cellular concentrations. To investigate the influence of nanoparticle encapsulation and aptamer functionalization of the **NAMI** analogs, **2-5** and **2-6**, cell uptake studies using ICP-MS were conducted.

Samples of nanoparticle encapsulated, AS1411-functionalized, and non encapsulated **2-5** and **2-6** were prepared using the optimal formulation. A non-specific aptamer functionalized NP sample for each drug was also prepared as a control for the AS1411 functionalized samples to examine the influence and efficiency of AS1411 as a targeting molecule. These samples were tested against triplicates of HCT-116 (colorectal cancer) cell lines, which the drugs showed the most promising activity against as determined via the cytotoxicity assays described above. Intracellular ruthenium content determined by ICP-MS is presented in **Table 3.4** and **Figure 3.6**.

Table 3.4. Intracellular ruthenium content of HCT-116 cells after incubation with 2-5 and 2-6 in different NP formulations.

		Intracellular Ruthenium Mass (ng/10^3 cells)	
Formulation Type	**Aptamer Type**	**2-5**	**2-6**
Free Complex	N/A	1.05 ± 0.04	1.9 ± 0.2
Drug-NP	N/A	2.0 ± 0.3	3.0 ± 0.2
Drug-NP-Aptamer	non-specific	1.40 ± 0.01	3.6 ± 0.5
Drug-NP-Aptamer	AS1411	4.1 ± 0.3	4.6 ± 0.1

*Standard deviation was calculated from triplicate samples. Statistical significance of the results was determined using a two-way ANOVA with p-values <0.05 considered being significant.

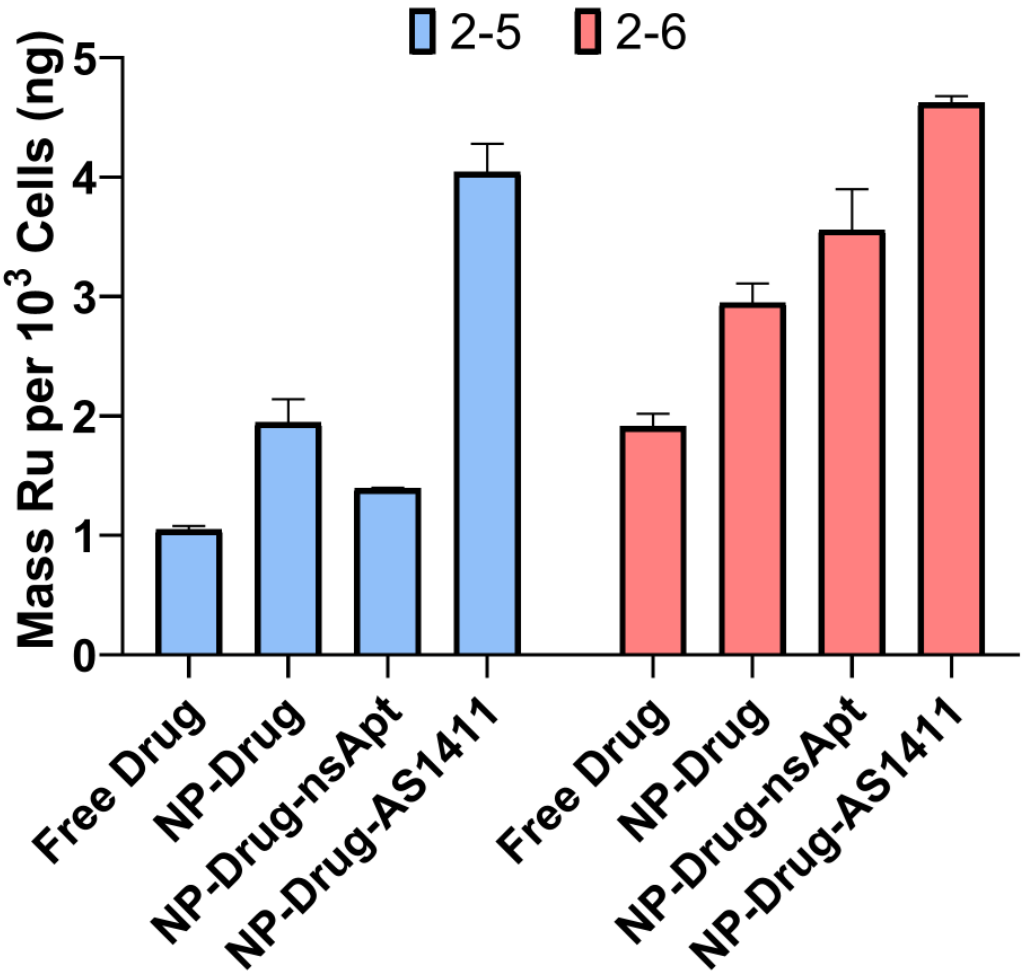

Figure 3.6 Intracellular ruthenium content (ng/10^3cells) of HCT-116 cells after 24 hours of incubation using 2-5 and 2-6 using different drug delivery methods.

The cell uptake data demonstrate the efficacy of nanoparticle encapsulation in enhancing the intracellular delivery of the **NAMI** analogs. Notably, an approximately 2-fold increase in intracellular ruthenium content was observed when comparing drug-loaded PLGA-PEG NPs to non-encapsulated **2-5** administration. Furthermore, functionalization with AS1411, further doubled the intracellular ruthenium content (for **2-6**) from 2.0 ± 0.2 ng/10^3cells to 4.6 ± 0.1 ng/10^3cells. It is unsurprising that compound **2-6** exhibited higher cell uptake values than **2-5** across all delivery methods, attributed to the presence of the lipophilic CF_3 moiety.

The presence of the non-specific aptamer had a negative impact on cellular accumulation of **2-5** and a modest positive impact on the uptake of **2-6**, versus the unfunctionalized NP formulations. These changes in uptake, compared to non-functionalized nanoparticles, may not be directly attributed to the non-specific aptamer. Instead, they may be due to initial diffusion out of the nanoparticles, followed by the entry of the free complex into the cell. Moreover, ruthenium uptake in the case of non-specific aptamer-functionalized NPs is elevated for **2-6** due to the lipophilic nature of the drug, facilitating increased uptake of the diffused drug into the cells. As determined by the Log*D* calculations presented in chapter 2, **2-6** exhibits lipophilic properties that could allow for an elevated level of passive diffusion across cell membranes.

Although nanoparticle encapsulation and aptamer-functionalization increased the overall cell uptake of the drug candidates, this enhancement did not translate into increased cytotoxic activity. As discussed above, no antiproliferative activity was observed with the nanoparticle encapsulation of drugs in the *in-vitro* experiments. These findings can have two possible implications. First, the lack of correlation between drug uptake and cytotoxicity may indicate that the ruthenium compounds **2-5** and **2-6** induce cytotoxicity through mechanisms that do not involve cell entry such as interactions with the cell membrane or cell surface receptors. Alternatively, the more plausible explanation behind this phenomenon is that the nanoparticles may have different release profiles within the cells. Consequently, lower than necessary amounts of drug may be released within the cells for the cytotoxic activity to occur, or the intracellular targeting of specific organelles may be inhibited. Nevertheless, the cell uptake results demonstrate the successful targeted delivery of aptamer-functionalized ruthenium-containing nanoparticles to cancer cells.

3.4. Conclusions

In this chapter, the new analogs of **NAMI** synthesized in **Chapter 2** were successfully encapsulated in polymeric PLGA-PEG nanoparticles using optimal loading parameters determined via ICP-MS experiments. Aptamer-functionalization of drug-containing nanoparticles was utilized to introduce active targeting with the goal of increasing cellular uptake and *in-vitro* activity. Characterization of the drug-containing nanoparticles via DLS and zeta potential measurements revealed the nanoparticles had suitable sizes and relative surface charges for targeting tumors.

Aptamer-functionalized PLGA-PEG nanoparticles containing the ruthenium complexes **2-5** and **2-6** exhibited ideal sub-200 nm average particle diameter size, allowing the possibility to take advantage of the enhanced retention and permeability (EPR) effect. Specifically, PLGA-PEG-AS1411 NPs containing **2-5** and **2-6** showed average particle diameters of 150 ± 50 nm and 140 ± 40 nm, respectively. In addition, the relatively high surface charge determined by zeta potential measurements observed with all formulations was indicative of acceptable colloidal stability in solution. Moreover, aptamer-functionalized nanoparticles exhibited consistently higher surface charge values due to the influence of the negatively charged phosphate backbone of the single stranded DNA (aptamer).

The release profile of the drugs out of the nanoparticles was examined via ICP-MS studies. This experiment revealed that drug release from the PLGA-PEG nanoparticles follows a two-phase process. Nanoparticles containing both ruthenium drugs exhibited a similar ‘burst’ release phase, where approximately 30% of the encapsulated drug is release. This burst release is followed by a more gradual release of the drug over 72 hours, likely via a combination of diffusion, polymer degradation and solvent penetration processes. The release profile of both drugs are promising for a sustained therapeutic effect.

Cellular uptake studies of the free-complexes, nanoparticle encapsulated complexes, and aptamer-functionalized NP encapsulated complexes highlighted the efficacy of nanoparticle delivery of ruthenium anticancer compounds. Cells treated with aptamer-functionalized nanoparticles contained 3 - 4x more intracellular ruthenium than cells treated with the free drugs. Overall, these findings demonstrate that nanoparticle

encapsulation of ruthenium anticancer agents and the functionalization of the NPs using active targeting molecules like aptamers can lead to increased drug uptake by cancer cells.

Surprisingly, the increased uptake of the Ru complexes mediated by the nanoparticle formulations did not translate to improved cytotoxicity. Indeed, the nanoparticle preparations were found to be essentially inactive. This is a significant result suggesting that the nanoparticles may negatively influence targeting of the complexes within cells. Moreover, this lack of observed activity could be attributed to factors such as NPs being sequestered in cellular compartment, and the *in-vitro* release inhibition of drugs which leads to insufficient amounts of the drug candidates reaching their target biomolecule.

The work presented in this chapter underscores the versatility and efficacy of aptamer-functionalized nanoparticle drug delivery systems for the targeted delivery of metal-based chemotherapeutics. Since nanoencapsulation using PLGA-PEG nanoparticles is well established and robust, it presents a simple route to greatly increase cellular uptake of both lipophilic and hydrophilic drugs. Furthermore, since most ruthenium-based chemotherapeutics undergo ligand-exchange process in biological environments, nanoencapsulation of these metal complexes can help mitigate pre-mature activation and unwanted chemical modifications prior to drug delivery to target tissues. The research presented in this chapter presents an alternative route to the conventional synthetic methods, such as ligand modification to improve the uptake and pharmacological properties of Ru(III) drug candidates.

Chapter 4. Future Work & Conclusions

4.1. Thesis Summary

The research presented in this thesis focused on the syntheses, nanoparticle encapsulation, and delivery of new analogs of the Ru(III) anticancer candidate **NAMI**. The key contributions outlined in this work encompass several key areas. First, is the design, synthesis, characterization of novel fluorescent **NAMI** analogs, aimed at expanding the repertoire of fluorescent probes for medicinal application. Additionally, comprehensive investigation of ligand-exchange behaviour, lipophilicity, and in-vitro activity of the synthesized compounds was performed, providing insight into their intracellular fates and interactions. Furthermore, the synthesis, optimization, characterization, and the investigation of the drug release profile of drug-loaded nanoparticles was developed, with the goal of producing a stable drug-delivery system with a controlled release profile. Finally, the effect of aptamer functionalization and nanoencapsulation on cell uptake and in-vitro activity was examined and offered valuable insight into methods of actively targeting and increasing cellular uptake of ruthenium anticancer drugs.

In **Chapter 2**, the functionalization of Ru(III) anticancer agents with CF_3 moieties and its subsequent effects on the physiochemical properties of the molecules were investigated. An increase in the distribution coefficient (Log*D*) was calculated with CF_3 functionalization, reflecting increased lipophilicity. This enhancement of lipophilicity was correlated with increased cell uptake of drug candidates reported in **Chapter 3,** along with an enhancement of cytotoxicity against cancer cells. The *in-vitro* cytotoxicity results highlighted the selective nature of the antiproliferative activity of ruthenium anticancer agents compared to their platinum-based counterparts. Investigation of ligand-exchange processes via NMR and UV-Vis revealed that activation of the Ru(III) complexes involves the exchange of a chloride ligand via hydrolysis, in both compounds, leading to the formation of the biologically active mono-aquo species.

Chapter 3 explored alternative drug delivery strategies for the new analogs of **NAMI** through nanoencapsulation via PLGA-PEG polymeric nanoparticles. In addition, the introduction of active targeting via aptamer-functionalization of the NPs was investigated. Significant improvements in cell uptake of ruthenium were observed with

nanoparticle encapsulation, and further improvements made through the functionalization of those NPs with Nucleolin-targeting aptamer. The drug release study of the drug-containing PLGA-PEG nanoparticles revealed a two-phased leaching mechanism of the drug out of the NPs. This included an initial burst release caused by the diffusion of drugs out of the nanoparticles, followed by a slower release likely due to diffusion, polymer degradation, and solvent penetration into the NPs.

Overall, with the research presented we hope to address some of the challenges associated with the Ru(III) anticancer compounds, by the targeted delivery of these drugs via chemical functionalization and nanoencapsulation in aptamer functionalized PLGA-PEG polymeric NPs.

4.2. Future Work

One of the limitations faced in this body of work was the loss of quantum yield upon the appendage of the ligands to the Ru(III) metal centre. These results were attributed to the change in the electronic and steric properties of the ligand-metal structure upon ligand conjugation which could quench the fluorescence of the resulting molecule. First, as part of future work, the in-vitro fluorescence of the metal complexes must be investigated to determine the viability of the drugs as fluorescent handles. Furthermore, the molecule can be modified by tuning the pyridine linker on the ligand to change the fluorescent properties of the ruthenium complex. Lastly, the length of the aliphatic carbon chain on the linker molecule can be modified to investigate its effects on QY values.

Importantly, in addition to exploring alternative nanoparticle delivery methods through the utilization of systems such as lipid nanoparticles and micelles, deeper mechanistic studies should be conducted to determine the underlying mechanisms responsible for the lack of cytotoxic activity of nanoparticle encapsulated ruthenium complexes observed in this thesis. This would give further insight into the release profile of the drug inside cells, cell uptake mechanisms, cellular internalization pathways, and interaction of the nanoparticles with intracellular components.

Finally, efforts should be made to translate the promising *in-vitro* cytotoxic findings into clinical and *in-vivo* applications. This may involve further preclinical testing

in appropriate animal testing models to determine the activity of drug-loaded nanoparticles.

References

(1) Sigel, Astrid.; Sigel, Helmut. *Metal Ions and Their Complexes in Medication*; Marcel Dekker, 2004.

(2) Dasari, S.; Bernard Tchounwou, P. Cisplatin in Cancer Therapy: Molecular Mechanisms of Action. *Eur. J. Pharmacol.* **2014**, *740*, 364–378.

(3) Carroll, V.; Demoin, D. W.; Hoffman, T. J.; Jurisson, S. S. Inorganic Chemistry in Nuclear Imaging and Radiotherapy: Current and Future Directions. *Radiochim Acta* **2012**, *100* (8–9), 653–667.

(4) Dabrowiak, J. C. *Metals in Medicine*; John Wiley & Sons, 2009.

(5) Jungwirth, U.; Kowol, C. R.; Keppler, B. K.; Hartinger, C. G.; Berger, W.; Heffeter, P. Anticancer Activity of Metal Complexes: Involvement of Redox Processes. *Antioxid. Redox Signal.* **2011**, *15* (4), 1085–1127.

(6) Ranasinghe, R.; Mathai, M. L.; Zulli, A. Cisplatin for Cancer Therapy and Overcoming Chemoresistance. *Heliyon* **2022**, *8* (9), 1–17.

(7) Astolfi, L.; Ghiselli, S.; Guaran, V.; Chicca, M.; Simoni, E.; Olivetto, E.; Lelli, G.; Martini, A. Correlation of Adverse Effects of Cisplatin Administration in Patients Affected by Solid Tumours: A Retrospective Evaluation. *Oncol. Rep.* **2013**, *29* (4), 1285–1292.

(8) Stevens, S. K.; Strehle, A. P.; Miller, R. L.; Gammons, S. H.; Hoffman, K. J.; McCarty, J. T.; Miller, M. E.; Stultz, L. K.; Hanson, P. K. The Anticancer Ruthenium Complex KP1019 Induces DNA Damage, Leading to Cell Cycle Delay and Cell Death in Saccharomyces Cerevisiae. *Mol. Pharmacol.* **2013**, *83* (1), 225–234.

(9) Gransbury, G. K.; Kappen, P.; Glover, C. J.; Hughes, J. N.; Levina, A.; Lay, P. A.; Musgrave, I. F.; Harris, H. H. Comparison of KP1019 and NAMI-A in Tumour-Mimetic Environments. *Metallomics.* **2016**, *8* (8), 762–773.

(10) Heffeter, P.; Böck, K.; Atil, B.; Reza Hoda, M. A.; Körner, W.; Bartel, C.; Jungwirth, U.; Keppler, B. K.; Micksche, M.; Berger, W.; Koellensperger, G. Intracellular Protein Binding Patterns of the Anticancer Ruthenium Drugs KP1019 and KP1339. *Journal of Biological Inorganic Chemistry* **2010**, *15* (5), 737–748.

(11) Cázares Marinero, J. D. J.; Lapierre, M.; Cavaillès, V.; Saint-Fort, R.; Vessières, A.; Top, S.; Jaouen, G. Efficient New Constructs against Triple Negative Breast Cancer Cells: Synthesis and Preliminary Biological Study of Ferrocifen-SAHA Hybrids and Related Species. *Dalt. Trans.* **2013**, *42* (43), 15489–15501.

(12) Idlas, P.; Lepeltier, E.; Jaouen, G.; Passirani, C. Ferrocifen Loaded Lipid Nanocapsules: A Promising Anticancer Medication against Multidrug Resistant Tumors. *Cancers (Basel)* **2021**, *13* (10), 1–23.

(13) Karges, J.; Stokes, R. W.; Cohen, S. M. Metal Complexes for Therapeutic Applications. *Trends Chem.* Cell Press July 1, 2021, pp 523–534.

(14) Top, S.; Dauer, B.; Vaissermann, J.; Jaouen, G. Chemistry Facile Route to Ferrocifen, 1-[4-(2-Dimethylaminoethoxy)]-1-(Phenyl-2-Ferrocenyl-but-1-Ene), First Organometallic Analogue of Tamoxifen, by the McMurry Reaction. *J. Organomet. Chem.* **1997**, *541*, 355–361.

(15) Li, L.; Wong, Y. S.; Chen, T.; Fan, C.; Zheng, W. Ruthenium Complexes Containing Bis-Benzimidazole Derivatives as a New Class of Apoptosis Inducers. *Dalt. Trans.* **2012**, *41* (4), 1138–1141.

(16) Stordal, B.; Davey, M. Understanding Cisplatin Resistance Using Cellular Models. *IUBMB Life* **2007**, *59* (11), 696–699.

(17) Brabec, V.; Kasparkova, J. Modifications of DNA by Platinum Complexes: Relation to Resistance of Tumors to Platinum Antitumor Drugs. *Drug Resist. Updat.* **2005**, *8* (3), 131–146.

(18) Fang, Y.; Lin, S.; Yang, F.; Situ, J.; Lin, S.; Luo, Y. Aptamer-Conjugated Multifunctional Polymeric Nanoparticles as Cancer-Targeted, MRI-Ultrasensitive Drug Delivery Systems for Treatment of Castration-Resistant Prostate Cancer. *Biomed. Res. Int.* **2020**, *2020*, 1–12.

(19) Howell, A.; Howell, S. J. Tamoxifen Evolution. *Br. J. Cancer.* **2023**, *128* (3), 421–425.

(20) Chang, M. Tamoxifen Resistance in Breast Cancer. *Biomol. Ther.* May 2012, pp 256–267.

(21) Top, S.; Vessiè, A.; Cabestaing, C.; Laios, I.; Leclercq, G.; Provot, C.; Jaouen, G. Studies on Organometallic Selective Estrogen Receptor Modulators. (SERMs) Dual Activity in the Hydroxy-Ferrocifen Series. *J. Organomet. Chem.* **2001**, *637*, 500–506.

(22) Chattaraj, A.; Masood, ; Syed, P.; Low, C. A.; Owonikoko, T. K. Cisplatin-Induced Ototoxicity: A Concise Review of the Burden, Prevention, and Interception Strategies. Background and Burden of the Problem. *JCO. Oncol. Pract.* **2023**, *19*, 278–283.

(23) Zhang, Q.; Lu, Q. Bin. New Combination Chemotherapy of Cisplatin with an Electron-Donating Compound for Treatment of Multiple Cancers. *Sci. Rep.* **2021**, *11* (1), 1–13.

(24) Dasari, S.; Bernard Tchounwou, P. Cisplatin in Cancer Therapy: Molecular Mechanisms of Action. *Eur. J. Pharmacol.* Elsevier October 5, 2014, pp 364–378.

(25) Kenny, R. G.; Marmion, C. J. Toward Multi-Targeted Platinum and Ruthenium Drugs - A New Paradigm in Cancer Drug Treatment Regimens? *Chem. Rev.* **2019**, *119* (2), 1058–1137.

(26) Wang, L.; Zhao, X.; Fu, J.; Xu, W.; Yuan, J. The Role of Tumour Metabolism in Cisplatin Resistance. *Front. Mol. Biosci.* **2021**, *8*, 1–13.

(27) Keener, A. Innovative Therapies to Tackle Platinum-Resistant Ovarian Cancer. *Nature* **2021**, *600*, 845–847.

(28) Konkankit, C. C.; Marker, S. C.; Knopf, K. M.; Wilson, J. J. Anticancer Activity of Complexes of the Third Row Transition Metals, Rhenium, Osmium, and Iridium. *Dalt. Trans.* **2018**, *47* (30), 9934–9974.

(29) Zhang, P.; Huang, H. Future Potential of Osmium Complexes as Anticancer Drug Candidates, Photosensitizers and Organelle-Targeted Probes. *Dalt. Trans.* **2018**, *47* (42), 14841–14854.

(30) Ellahioui, Y.; Prashar, S.; Gómez-Ruiz, S. Anticancer Applications and Recent Investigations of Metallodrugs Based on Gallium, Tin and Titanium. *Inorganics (Basel)* **2017**, *5* (1), 1–23.

(31) Meier-Menches, S. M.; Gerner, C.; Berger, W.; Hartinger, C. G.; Keppler, B. K. Structure-Activity Relationships for Ruthenium and Osmium Anticancer Agents-towards Clinical Development. *Chem. Soc. Rev.* **2018**, *47* (3), 909–928.

(32) Knopf, K. M.; Murphy, B. L.; Macmillan, S. N.; Baskin, J. M.; Barr, M. P.; Boros, E.; Wilson, J. J. In Vitro Anticancer Activity and in Vivo Biodistribution of Rhenium(I) Tricarbonyl Aqua Complexes. *J. Am. Chem. Soc.* **2017**, *139* (40), 14302–14314.

(33) Santini, C.; Pellei, M.; Gandin, V.; Porchia, M.; Tisato, F.; Marzano, C. Advances in Copper Complexes as Anticancer Agents. *Chem. Rev.* **2014**, *114* (1), 815–862.

(34) Moreno-Alcántar, G.; Picchetti, P.; Casini, A. Gold Complexes in Anticancer Therapy: From New Design Principles to Particle-Based Delivery Systems. *Angew. Chem., Int. Ed.* **2023**, *62* (22), 1–32.

(35) Musumeci, D.; Rozza, L.; Merlino, A.; Paduano, L.; Marzo, T.; Massai, L.; Messori, L.; Montesarchio, D. Interaction of Anticancer Ru(III) Complexes with Single Stranded and Duplex DNA Model Systems. *Dalt. Trans.* **2015**, *44* (31), 13914–13925.

(36) Alessio, E.; Balducci, G.; Calligaris, M.; Costa, G.; Attia, W. M.; Mestroni, G. Synthesis, Molecular Structure, and Chemical Behavior of Hydrogen Trans-Bis(Dimethyl Sulfoxide)Tetrachlororuthenate(III) and Mer-Trichlorotris(Dimethyl Sulfoxide)Ruthenium(III): The First Fully Characterized Chloride-Dimethyl Sulfoxide-Ruthenium (III) Complexes. *Inorg. Chem* **1991**, *30*, 609–618.

(37) Dömötör, O.; Hartinger, C. G.; Bytzek, A. K.; Kiss, T.; Keppler, B. K.; Enyedy, E. A. Characterization of the Binding Sites of the Anticancer Ruthenium(III) Complexes KP1019 and KP1339 on Human Serum Albumin via Competition Studies. *Journal of Biological Inorganic Chemistry* **2013**, *18* (1), 9–17.

(38) Trondl, R.; Heffeter, P.; Kowol, C. R.; Jakupec, M. A.; Berger, W.; Keppler, B. K. NKP-1339, the First Ruthenium-Based Anticancer Drug on the Edge to Clinical Application. *Chem. Sci,* **2014**, *5* (8), 2925–2932.

(39) Lee, S. Y.; Kim, C. Y.; Nam, T. G. Ruthenium Complexes as Anticancer Agents: A Brief History and Perspectives. *Drug Des Devel Ther.* **2020**, *14*, 5375–5392.

(40) Reedijk, J. Metal-Ligand Exchange Kinetics in Platinum and Ruthenium Complexes: Significance for Effectiveness as Anticancer Drugs. *Platin. Met. Rev.* **2008**, *52* (1), 2–11.

(41) Heffeter, P.; Böck, K.; Atil, B.; Reza Hoda, M. A.; Körner, W.; Bartel, C.; Jungwirth, U.; Keppler, B. K.; Micksche, M.; Berger, W.; Koellensperger, G. Intracellular Protein Binding Patterns of the Anticancer Ruthenium Drugs KP1019 and KP1339. *J. Biol. Inorg. Chem.* **2010**, *15* (5), 737–748.

(42) Pongratz, M.; Schluga, P.; Jakupec, M. A.; Arion, V. B.; Hartinger, C. G.; Allmaier, G.; Keppler, B. K. Transferrin Binding and Transferrin-Mediated Cellular Uptake of the Ruthenium Coordination Compound KP1019, Studied by Means of AAS, ESI-MS and CD Spectroscopy. *J. Anal. At. Spectrom.* **2004**, *19* (1), 46–51.

(43) Clarke, M. J. Ruthenium Metallopharmaceuticals. *Coord. Chem. Rev.* **2002**, *232* (1–2), 69–93.

(44) Alessio, E.; Messori, L. NAMI-A and KP1019/1339, Two Iconic Ruthenium Anticancer Drug Candidates Face-to-Face: A Case Story in Medicinal Inorganic Chemistry. *Molecules* **2019**, *24* (10), 1–20.

(45) Flocke, L. S.; Trondl, R.; Jakupec, M. A.; Keppler, B. K. Molecular Mode of Action of NKP-1339 – a Clinically Investigated Ruthenium-Based Drug – Involves ER- and ROS-Related Effects in Colon Carcinoma Cell Lines. *Invest. New. Drugs.* **2016**, *34* (3), 261–268.

(46) Antonarakis, E. S.; Emadi, A. Ruthenium-Based Chemotherapeutics: Are They Ready for Prime Time? *Cancer. Chemother. Pharmacol.* **2010**, *66* (1), 1–9.

(47) Hartinger, C. G.; Jakupec, M. A.; Zorbas-Seifried, S.; Groessl, M.; Egger, A.; Berger, W.; Zorbas, H.; Dyson, P. J.; Keppler, B. K. KP1019, a New Redox-Active Anticancer Agent - Preclinical Development and Results of a Clinical Phase I Study in Tumor Patients. *Chem. Biodivers.* **2008**, *5* (10), 2140–2155.

(48) Berger, M. R.; Garzon, F. T.; Keppler, B. K.; Schmähl, D. Efficacy of New Ruthenium Complexes against Chemically Induced Autochthonous Colorectal Carcinoma in Rats. *Anticancer. Res.* **1989**, *9* (3), 761–765.

(49) Alessio, E. Thirty Years of the Drug Candidate NAMI-A and the Myths in the Field of Ruthenium Anticancer Compounds: A Personal Perspective. *Eur. J. Inorg. Chem.* **2017**, *12*, 1549–1560.

(50) Alessio, E.; Messori, L. The Deceptively Similar Ruthenium(III) Drug Candidates KP1019 and NAMI-A Have Different Actions. What Did We Learn in the Past 30 Years? In *Met. Ions. Life. Sci.*; Walter de Gruyter GmbH, 2018; Vol. 18, pp 141–170.

(51) Pereira, E. S.; Chagas, M. A.; Rocha, W. R. Reduction Potential of RuIII-Based Complexes with Potential Antitumor Activity and Thermodynamics of Their Hydrolysis Reactions and Interactions with Possible Biological Targets: A Theoretical Investigation. *J. Braz. Chem. Soc.* **2019**, *30* (3), 571–584.

(52) Muz, B.; de la Puente, P.; Azab, F.; Azab, A. K. The Role of Hypoxia in Cancer Progression, Angiogenesis, Metastasis, and Resistance to Therapy. *Hypoxia.* **2015**, *5* (3), 83–92.

(53) Zelonka, R. A.; Baird, M. C. Benzene Complexes of Ruthenium(I1). *Can. J. Chem.* **1972**, *50*, 3063–3072.

(54) Dale, L. D.; Tocher, J. H.; Dyson, T. M.; Edwards, D. I.; Tocher, D. A. Studies on DNA Damage and Induction of SOS Repair by Novel Multifunctional Bioreducible Compounds. II. A Metronidazole Adduct of a Ruthenium-Arene Compound. *Anticancer. drug. des.* **1992**, *7* (1), 3–14.

(55) Dyson, P. J. Systematic Design of a Targeted Organometallic Antitumour Drug in Pre-Clinical Development. *Chimia (Aarau)* **2007**, *61* (11), 698–703.

(56) Allardyce, C. S.; Dyson, P. J.; Ellis, D. J.; Heath, S. L. [Ru(H6-p-Cymene)Cl2(Pta)] (Pta = 1,3,5-Triaza-7-Phosphatricyclo-[3.3.1.1]Decane): A Water Soluble Compound That Exhibits PH Dependent DNA Binding Providing Selectivity for Diseased Cells. *Chem. Comm.* **2001**, No. 15, 1396–1397.

(57) Murray, B. S.; Babak, M. V.; Hartinger, C. G.; Dyson, P. J. The Development of RAPTA Compounds for the Treatment of Tumors. *Coord. Chem. Rev.* **2016**, *306* (P1), 86–114.

(58) Zeng, L.; Gupta, P.; Chen, Y.; Wang, E.; Ji, L.; Chao, H.; Chen, Z. S. The Development of Anticancer Ruthenium(II) Complexes: From Single Molecule Compounds to Nanomaterials. *Chem. Soc. Rev.* **2017**, *46* (19), 5771–5804.

(59) Scolaro, C.; Bergamo, A.; Brescacin, L.; Delfino, R.; Cocchietto, M.; Laurenczy, G.; Geldbach, T. J.; Sava, G.; Dyson, P. J. In Vitro and in Vivo Evaluation of Ruthenium(II)-Arene PTA Complexes. *J. Med. Chem.* **2005**, *48* (12), 4161–4171.

(60) Morris, R. E.; Aird, R. E.; Del Socorro Murdoch, P.; Chen, H.; Cummings, J.; Hughes, N. D.; Parsons, S.; Parkin, A.; Boyd, G.; Jodrell, D. I.; Sadler, P. J. Inhibition of Cancer Cell Growth by Ruthenium(II) Arene Complexes. *J. Med. Chem.* **2001**, *44* (22), 3616–3621.

(61) Adhireksan, Z.; Davey, G. E.; Campomanes, P.; Groessl, M.; Clavel, C. M.; Yu, H.; Nazarov, A. A.; Yeo, C. H. F.; Ang, W. H.; Dröge, P.; Rothlisberger, U.; Dyson, P. J.; Davey, C. A. Ligand Substitutions between Ruthenium-Cymene Compounds Can Control Protein versus DNA Targeting and Anticancer Activity. *Nat. Commun.* **2014**, *5*, 1–13.

(62) Clarke, M. J.; Bitier, S.; Rennert, D.; Buchbinder, M.; Kelman, D. Reduction and Subsequent Binding of Ruthenium Ions Catalyzed by Subcellular Components. *J. Inorg. Biochem.* **1980**, *12*, 0.

(63) Durig, J. R.; Danneman, J.; Behnke, W. D.; Mercer, E. E. The Induction of Filamentous Growth in Escherichia Coli by Ruthenium and Palladium Complexes. *Chem. Biol. Interact.* **1976**, *13*, 28–35.

(64) Rademaker-Lakhai, J. M.; Van Den Bongard, D.; Pluim, D. Ruthenium Anticancer Agent DMSO-Imidazole-Tetrachlororuthenate, a Novel Trans-A Phase I and Pharmacological Study with Imidazolium-E-Mail Alerts. *Clin. Cancer. Res.* **2004**, *10*, 3717–3727.

(65) Hartinger, C. G.; Zorbas-Seifried, S.; Jakupec, M. A.; Kynast, B.; Zorbas, H.; Keppler, B. K. From Bench to Bedside - Preclinical and Early Clinical Development of the Anticancer Agent Indazolium Trans-[Tetrachlorobis(1H-Indazole)Ruthenate(III)] (KP1019 or FFC14A). *J. Inorg. Biochem.* **2006**, *100* (5–6), 891–904.

(66) Kapitza, S.; Pongratz, M.; Jakupec, M. A.; Heffeter, P.; Berger, W.; Lackinger, L.; Keppler, B. K.; Marian, B. Heterocyclic Complexes of Ruthenium(III) Induce Apoptosis in Colorectal Carcinoma Cells. *J. Cancer. Res. Clin. Oncol.* **2005**, *131* (2), 101–110.

(67) *Bold Therapeutics - Technology*. https://www.bold-therapeutics.com/technology (accessed 2023-11-10).

(68) Fuereder, T.; Berger, W. Metal Drugs Become Targeted. *ESMO Open* **2017**, *2* (3), 1–3.

(69) Bergamo, A.; Zorzet, S.; Gava, B.; Sorc, A.; Alessio, E.; Iengo, E.; Sava, G. Preclinical Report Effects of NAMI-A and Some Related Ruthenium Complexes on Cell Viability after Short Exposure of Tumor Cells. *Anticancer Drugs* **2000**, *11*, 665–672.

(70) Yusuf, A.; Almotairy, A. R. Z.; Henidi, H.; Alshehri, O. Y.; Aldughaim, M. S. Nanoparticles as Drug Delivery Systems: A Review of the Implication of Nanoparticles' Physicochemical Properties on Responses in Biological Systems. *Polymers (Basel)* **2023**, *15* (7), 1–26.

(71) Murthy, S. K. Nanoparticles in Modern Medicine: State of the Art and Future Challenges. *Int. J. Nanomedicine.* **2007**, *2* (2), 129–141.

(72) Jeevanandam, J.; Barhoum, A.; Chan, Y. S.; Dufresne, A.; Danquah, M. K. Review on Nanoparticles and Nanostructured Materials: History, Sources, Toxicity and Regulations. *Beilstein. J. Nanotechnol.* **2018**, *9* (1), 1050–1074.

(73) Haleem, A.; Javaid, M.; Singh, R. P.; Rab, S.; Suman, R. Applications of Nanotechnology in Medical Field: A Brief Review. *J. Glob. Health* **2023**, *7* (2), 70–77.

(74) Åkerman, M. E.; W Chan, W. C.; Laakkonen, P.; Bhatia, S. N.; Ruoslahti, E. Nanocrystal Targeting in Vivo. *Proc. Nat. Acad. Sci. U. S. A.* **2002**, *99* (20), 12617–12621.

(75) Harisinghani, M. G.; Barentsz, J.; Hahn, P. F.; Deserno, W. M.; Tabatabaei, S.; Hulsbergen van de Kaa, C.; de la Rosette, J.; Weissleder, R. Noninvasive Detection of Clinically Occult Lymph-Node Metastases in Prostate Cancer. *N. Engl. J. Med.* **2003**, *25*, 2491–2500.

(76) Feynman, R. There's Plenty of Room at the Bottom. *Eng. Sci.* **1960**, *23* (5), 22–36.

(77) De Jaeghere, F.; Allémann E; Kubel, F.; Galli, B.; Cozens, R.; Doelker, E.; Gurny, R. Oral Bioavailability of a Poorly Water Soluble HIV-1 Protease Inhibitor Incorporated into PH-Sensitive Particles. *J. Control. Release.* **2000**, *68* (2), 272–278.

(78) John, A. E.; Lukacs, N. W.; Berlin, A. A.; Palecanda, A.; Bargatze, R. F.; Stoolman, L. M.; Nagy, J. O. Discovery of a Potent Nanoparticle P-selectin Antagonist with Anti-inflammatory Effects in Allergic Airway Disease. *FASEB. J.* **2003**, *17* (15), 2296–2298.

(79) Vandghanooni, S.; Eskandani, M.; Barar, J.; Omidi, Y. AS1411 Aptamer-Decorated Cisplatin-Loaded Poly(Lactic-Co-Glycolic Acid) Nanoparticles for Targeted Therapy of MiR-21-Inhibited Ovarian Cancer Cells. *Nanomedicine (Lond)* **2018**, *13* (21), 2729–2758.

(80) Sultan, M. H.; Moni, S. S.; Madkhali, O. A.; Bakkari, M. A.; Alshahrani, S.; Alqahtani, S. S.; Alhakamy, N. A.; Mohan, S.; Ghazwani, M.; Bukhary, H. A.; Almoshari, Y.; Salawi, A.; Alshamrani, M. Characterization of Cisplatin-Loaded Chitosan Nanoparticles and Rituximab-Linked Surfaces as Target-Specific Injectable Nano-Formulations for Combating Cancer. *Sci. Rep.* **2022**, *12* (1), 1–16.

(81) Kango, S.; Kalia, S.; Celli, A.; Njuguna, J.; Habibi, Y.; Kumar, R. Surface Modification of Inorganic Nanoparticles for Development of Organic-Inorganic Nanocomposites - A Review. *Prog. Polym. Sci.* **2013**, *38* (8), 1232–1261.

(82) Salatin, S.; Maleki Dizaj, S.; Yari Khosroushahi, A. Effect of the Surface Modification, Size, and Shape on Cellular Uptake of Nanoparticles. *Cell. Biol. Int.* **2015**, *39* (8), 881–890.

(83) Shi, L.; Zhang, J.; Zhao, M.; Tang, S.; Cheng, X.; Zhang, W.; Li, W.; Liu, X.; Peng, H.; Wang, Q. Effects of Polyethylene Glycol on the Surface of Nanoparticles for Targeted Drug Delivery. *Nanoscale* **2021**, *13* (24), 10748–10764.

(84) Suk, J. S.; Xu, Q.; Kim, N.; Hanes, J.; Ensign, L. M. PEGylation as a Strategy for Improving Nanoparticle-Based Drug and Gene Delivery. *Adv. Drug. Deliv. Rev.* **2016**, *99*, 28–51.

(85) Wu, J. The Enhanced Permeability and Retention (Epr) Effect: The Significance of the Concept and Methods to Enhance Its Application. *J. Pers. Med.* **2021**, *11* (8), 1–8.

(86) Uchino, H.; Matsumura, Y.; Negishi, T.; Koizumi, F.; Hayashi, T.; Honda, T.; Nishiyama, N.; Kataoka, K.; Naito, S.; Kakizoe, T. Cisplatin-Incorporating Polymeric Micelles (NC-6004) Can Reduce Nephrotoxicity and Neurotoxicity of Cisplatin in Rats. *Br. J. Cancer.* **2005**, *93* (6), 678–687.

(87) Johnstone, T. C.; Kulak, N.; Pridgen, E. M.; Farokhzad, O. C.; Langer, R.; Lippard, S. J. Nanoparticle Encapsulation of Mitaplatin and the Effect Thereof on in Vivo Properties. *ACS Nano* **2013**, *7* (7), 5675–5683.

(88) Dhar, S.; Gu, F. X.; Langer, R.; Farokhzad, O. C.; Lippard, S. J. Targeted Delivery of Cisplatin to Prostatecancer Cells by Aptamer Functionalized Pt(IV)Prodrug-PLGA–PEG Nanoparticles. *Proc. Natl. Acad. Sci. U.S.A.* **2008**, *105* (45), 17356–17361.

(89) Fischer, B.; Heffeter, P.; Kryeziu, K.; Gille, L.; Meier, S. M.; Berger, W.; Kowol, C. R.; Keppler, B. K. Poly(Lactic Acid) Nanoparticles of the Lead Anticancer Ruthenium Compound KP1019 and Its Surfactant-Mediated Activation. *Dalt. Trans.* **2014**, *43* (3), 1096–1104.

(90) Blunden, B. M.; Stenzel, M. H. Incorporating Ruthenium into Advanced Drug Delivery Carriers - an Innovative Generation of Chemotherapeutics. *J. Chem. Technol. Biotechnol.* **2015**, *90* (7), 1177–1195.

(91) Heffeter, P.; Riabtseva, A.; Senkiv, Y.; Kowol, C. R.; Körner, W.; Jungwith, U.; Mitina, N.; Keppler, B. K.; Konstantinova, T.; Yanchuk, I.; Stoika, R.; Zaichenko, A.; Berger, W. Nanoformulation Improves Activity of the (Pre)Clinical Anticancer Ruthenium Complex KP1019. *J. Biomed. Nanotechnol.* **2014**, *10* (5), 877–884.

(92) Kamaly, N.; Xiao, Z.; Valencia, P. M.; Radovic-Moreno, A. F.; Farokhzad, O. C. Targeted Polymeric Therapeutic Nanoparticles: Design, Development and Clinical Translation. *Chem. Soc. Rev.* **2012**, *41* (7), 2971–3010.

(93) Khan, S.; Hussain, A.; Fahimi, H.; Aliakbari, F.; Haj Bloukh, S.; Edis, Z.; Mahdi Nejadi Babadaei, M.; Izadi, Z.; Shiri Varnamkhasti, B.; Jahanshahi, F.; Lin, Y.; Hao, X.; Hasan Khan, R.; Rasti, B.; Vaghar-Lahijani, G.; Hua, L.; Derakhshankhah, H.; Sharifi, M.; Falahati, M. A Review on the Therapeutic Applications of Aptamers and Aptamer-Conjugated Nanoparticles in Cancer, Inflammatory and Viral Diseases. *Arab. J. Chem.* **2022**, *15* (2), 1–12.

(94) Jo, H.; Ban, C. Aptamer-Nanoparticle Complexes as Powerful Diagnostic and Therapeutic Tools. *Exp. Mol. Med.* **2016**, *48* (5), 1–9.

(95) Fu, Z.; Xiang, J. Aptamer-Functionalized Nanoparticles in Targeted Delivery and Cancer Therapy. *Int. J. Mol. Sci.* **2020**, *21* (23), 1–39.

(96) Catuogno, S.; Esposito, C. L.; de Franciscis, V. Developing Aptamers by Cell-Based SELEX. In *Methods mol. biol.*; Humana Press Inc., 2016; Vol. 1380, pp 33–46.

(97) Sefah, K.; Shangguan, D.; Xiong, X.; O'Donoghue, M. B.; Tan, W. Development of DNA Aptamers Using Cell-Selex. *Nat. Protoc.* **2010**, *5* (6), 1169–1185.

(98) Bosak, A.; Saraf, N.; Willenberg, A.; Kwan, M. W. C.; Alto, B. W.; Jackson, G. W.; Batchelor, R. H.; Nguyen-Huu, T. D.; Sankarapani, V.; Parks, G. D.; Seal, S.; Willenberg, B. J. Aptamer-Gold Nanoparticle Conjugates for the Colorimetric Detection of Arboviruses and Vector Mosquito Species. *RSC. Adv.* **2019**, *9* (41), 23752–23763.

(99) Liang, C.; Guo, B.; Wu, H.; Shao, N.; Li, D.; Liu, J.; Dang, L.; Wang, C.; Li, H.; Li, S.; Lau, W. K.; Cao, Y.; Yang, Z.; Lu, C.; He, X.; Au, D. W. T.; Pan, X.; Zhang, B. T.; Lu, C.; Zhang, H.; Yue, K.; Qian, A.; Shang, P.; Xu, J.; Xiao, L.; Bian, Z.; Tan, W.; Liang, Z.; He, F.; Zhang, L.; Lu, A.; Zhang, G. Aptamer-Functionalized Lipid Nanoparticles Targeting Osteoblasts as a Novel RNA Interference-Based Bone Anabolic Strategy. *Nat. Med.* **2015**, *21* (3), 288–294.

(100) Liu, J.; Lu, Y. Preparation of Aptamer-Linked Gold Nanoparticle Purple Aggregates for Colorimetric Sensing of Analytes. *Nat. Protoc.* **2006**, *1* (1), 246–252.

(101) Jeon, W.; Lee, S.; Dh, M.; Ban, C. A Colorimetric Aptasensor for the Diagnosis of Malaria Based on Cationic Polymers and Gold Nanoparticles. *Anal. Biochem.* **2013**, *439* (1), 11–16.

(102) Leijen, S.; Burgers, S. A.; Baas, P.; Pluim, D.; Tibben, M.; Van Werkhoven, E.; Alessio, E.; Sava, G.; Beijnen, J. H.; Schellens, J. H. M. Phase I/II Study with Ruthenium Compound NAMI-A and Gemcitabine in Patients with Non-Small Cell Lung Cancer after First Line Therapy. *Invest. New. Drugs.* **2015**, *33* (1), 201–214.

(103) Antony, S.; Morris, J. C.; Bell, T. D. M.; Brown, T.; Spiccia, L.; Harris, H. H. The H.G. Smith Award Article: Fluorescent Analogues of NAMI-A: Synthesis, Characterisation, Fluorescent Properties, and Preliminary Biological Studies in Human Lung Cancer Cells. *Aust. J. Chem.* **2014**, *67* (12), 1711–1717.

(104) Vargiu, A. V.; Robertazzi, A.; Magistrato, A.; Ruggerone, P.; Carloni, P. The Hydrolysis Mechanism of the Anticancer Ruthenium Drugs NAMI-A and ICR Investigated by DFT-PCM Calculations. *J. Phys. Chem. B.* **2008**, *112* (14), 4401–4409.

(105) Kostova, I. Ruthenium Complexes as Anticancer Agents. *Curr. Med. Chem.* **2006**, *13* (9), 1085–1107.

(106) Xiao, Y.; Guo, Y.; Dang, R.; Yan, X.; Xu, P.; Jiang, P. A Dansyl-Based Fluorescent Probe for the Highly Selective Detection of Cysteine Based on a d-PeT Switching Mechanism. *RCS. Adv.* **2017**, *7* (34), 21050–21053.

(107) Purser, S.; Moore, P. R.; Swallow, S.; Gouverneur, V. Fluorine in Medicinal Chemistry. *Chem. Soc. Revs.* **2008**, *37* (2), 320–330.

(108) Shah, P.; Westwell, A. D. The Role of Fluorine in Medicinal Chemistry. *J. Enzyme Inhib. Med. Chem.* **2007**, *22* (5), 527–540.

(109) Park, K.; Kitteringham, N. R.; O'neill, P. M. Metabolism of Fluorine-Containing Drugs. *Annu. Rev. Pharmacol. Toxicol* **2001**, *41*, 443–470.

(110) Liu, X.; Testa, B.; Fahr, A. Lipophilicity and Its Relationship with Passive Drug Permeation. *Pharm. Res.* **2011**, *28* (5), 962–977.

(111) Golshayan, A. R.; Antonarakis, E. S. Enzalutamide: An Evidence-Based Review of Its Usein the Treatment of Prostate Cancer. *Core. Evid..* **2013**, *8*, 27–35.

(112) Longley, D. B.; Harkin, D. P.; Johnston, P. G. 5-Fluorouracil: Mechanisms of Action and Clinical Strategies. *Nat. Rev. Cancer.* **2003**, *3* (5), 330–338.

(113) Crown, J.; O'Leary, M.; Ooi, W.-S. Docetaxel and Paclitaxel in the Treatment of Breast Cancer: A Review of Clinical Experience. *Oncologist.* **2004**, *9* (S2), 24–32.

(114) Ruiz-Cabello, J.; Barnett, B. P.; Bottomley, P. A.; Bulte, J. W. M. Fluorine (19F) MRS and MRI in Biomedicine. *NMR. Biomed.* **2011**, *24* (2), 114–129.

(115) Chang, S. W.; Lewis, A. R.; Prosser, K. E.; Thompson, J. R.; Gladkikh, M.; Bally, M. B.; Warren, J. J.; Walsby, C. J. CF3 Derivatives of the Anticancer Ru(III) Complexes KP1019, NKP-1339, and Their Imidazole and Pyridine Analogues Show Enhanced Lipophilicity, Albumin Interactions, and Cytotoxicity. *Inorg. Chem.* **2016**, *55* (10), 4850–4863.

(116) Alavijeh, M. S.; Chishty, M.; Qaiser, M. Z.; Palmer, A. M. Drug Metabolism and Pharmacokinetics, the Blood-Brain Barrier, and Central Nervous System Drug Discovery. *NeuroRx.* **2005**, *2* (4), 554–571.

(117) Mayer, J. M.; Hall, S. D.; Rowland, M. Relationship between Lipophilicity and Tubular Reabsorption for a Series of 5-Alkyl-5-Ethylbarbituric Acids in the Isolated Perfused Rat Kidney Preparation. *J. Pharm. Sci.* **1988**, *77* (4), 359–364.

(118) Testa, B.; Crivori, P.; Reist, M.; Carrupt, P.-A. The Influence of Lipophilicity on the Pharmacokinetic Behavior of Drugs: Concepts and Examples. *Perspect. drug discov. des.* **2000**, *19*, 179–211.

(119) Webb, M. I.; Chard, R. A.; Al-Jobory, Y. M.; Jones, M. R.; Wong, E. W. Y.; Walsby, C. J. Pyridine Analogues of the Antimetastatic Ru(III) Complex NAMI-A Targeting Non-Covalent Interactions with Albumin. *Inorg. Chem.* **2012**, *51* (2), 954–966.

(120) Prosser, K. E.; Xie, D.; Chu, A.; MacNeil, G. A.; Varju, B. R.; Kadakia, R. T.; Que, E. L.; Walsby, C. J. Copper(II) Pyridyl Aminophenolates: Hypoxia-Selective, Nucleus-Targeting Cytotoxins, and Magnetic Resonance Probes. *Chem. Eur. J.* **2021**, *27* (38), 9839–9849.

(121) Lipponer, K.-G.; Vogel, E.; Keppler, B. K. Synthesis, Characterization and Solution Chemistry of Trans-Indazoliumtetrachlorobis(Indazole)Ruthenate(III), a New Anticancer Ruthenium Complex. IR, UV, NMR, HPLC Investigations and Antitumor Activity. Crystal Structures of Trans-1-Methyl-Indazoliumtetrachlorobis-(1-Methylindazole)Ruthenate(III) and Its Hydrolysis Product Trans-Monoaquatrichlorobis-(1-Methylindazole)-Ruthenate(III). *Met. Based. Drugs.* **1996**, *3* (5), 243–260.

(122) Viswanadhan, V. N.; Ghose, A. K.; Revankar, G. R.; Robins, R. K. Atomic Physicochemical Parameters for Three Dimensional Structure Directed Quantitative Structure-Activity Relationships. 4. Additional Parameters for Hydrophobic and Dispersive Interactions and Their Application for an Automated Superposition of Certain Naturally Occurring Nucleoside Antibiotics. *J. Chem. Inf. Comput. Sci* **1989**, *29*, 163–172.

(123) Prosser, K. Spectroscopy and Mechanisms of Redox-Active Copper-Based Anticancer Complexes, Simon Fraser University, Burnaby, 2019.

(124) Köhler, F. H. Paramagnetic Complexes in Solution: The NMR Approach. In *eMagRes*; John Wiley and Sons Inc, 2011; pp 1–8.

(125) Alessio, E.; Balducci, G.; Lutman, A.; Mestroni, G.; Calligaris, M.; Attia, W. M. Synthesis and Characterization of Two New Classes of Ruthenium(III)-Sulfoxide Complexes with Nitrogen Donor Ligands. *Inorganica Chim. Acta.* **1993**, *203*, 205–217.

(126) OECD Publishing. OECD, Test No. 107: Partition Coefficient (n-Octanol/Water): Shake Flask Method., 1995.

(127) Mu, C.; Chang, S. W.; Prosser, K. E.; Leung, A. W. Y.; Santacruz, S.; Jang, T.; Thompson, J. R.; Yapp, D. T. T.; Warren, J. J.; Bally, M. B.; Beischlag, T. V.; Walsby, C. J. Induction of Cytotoxicity in Pyridine Analogues of the Anti-Metastatic Ru(III) Complex NAMI-A by Ferrocene Functionalization. *Inorg. chem.* **2016**, *55* (1), 177–190.

(128) Bramhall, J. Phospholipid Packing Asymmetry in Curved Membranes Detected by Fluorescence Spectroscopy. *Biochem.* **1986**, *25*, 3479–3486.

(129) Formica, M.; Fusi, V.; Giorgi, L.; Micheloni, M. New Fluorescent Chemosensors for Metal Ions in Solution. *Coord. Chem. Rev.* **2012**, *256* (1–2), 170–192.

(130) Iwunze, M. O. Fluorescence Quenching. *Spectroscopy (Santa Monica)* **2004**, *16* (10), 141–192.

(131) Mu, C.; Chang, S. W.; Prosser, K. E.; Leung, A. W. Y.; Santacruz, S.; Jang, T.; Thompson, J. R.; Yapp, D. T. T.; Warren, J. J.; Bally, M. B.; Beischlag, T. V.; Walsby, C. J. Induction of Cytotoxicity in Pyridine Analogues of the Anti-Metastatic Ru(III) Complex NAMI-A by Ferrocene Functionalization. *Inorg. Chem.* **2016**, *55* (1), 177–190.

(132) Silvestri, S.; Cirilli, I.; Marcheggiani, F.; Dludla, P.; Lupidi, G.; Pettinari, R.; Marchetti, F.; Di Nicola, C.; Falcioni, G.; Marchini, C.; Orlando, P.; Tiano, L.; Amici, A. Evaluation of Anticancer Role of a Novel Ruthenium(II)-Based Compound Compared with NAMI-A and Cisplatin in Impairing Mitochondrial Functionality and Promoting Oxidative Stress in Triple Negative Breast Cancer Models. *Mitochondrion* **2021**, *56*, 25–34.

(133) Páez-Franco, J. C.; Zermeño-Ortega, M. R.; de la O-Contreras, C. M.; Canseco-González, D.; Parra-Unda, J. R.; Avila-Sorrosa, A.; Enríquez, R. G.; Germán-Acacio, J. M.; Morales-Morales, D. Relevance of Fluorinated Ligands to the Design of Metallodrugs for Their Potential Use in Cancer Treatment. *Pharmaceutics* **2022**, *14* (2), 1–36.

(134) Papachristou, F.; Anninou, N.; Koukoulis, G.; Paraskakis, S.; Sertaridou, E.; Tsalikidis, C.; Pitiakoudis, M.; Simopoulos, C.; Tsaroucha, A. Differential Effects of Cisplatin Combined with the Flavonoid Apigenin on HepG2, Hep3B, and Huh7 Liver Cancer Cell Lines. *Mutat. Res. Genet. Toxicol. Environ. Mutagen.* **2021**, *866*, 1–13.

(135) Mi, L.; Kuang, H. Melatonin Regulates Cisplatin Resistance and Glucose Metabolism through Hippo Signaling in Hepatocellular Carcinoma Cells. *Cancer. Manag. Res.* **2020**, *12* (12), 1863–1874.

(136) Thiagarajan, S. K.; Perumal, K. V.; Shafie, N. H.; Kadir, K. K. A.; Bahari, H. Anti-Proliferative and Apoptotic Induction Effect of Elateriospermum Extract on Human Lung Cancer Cell Line A549. *Proc West Mark Ed Assoc Conf* **2020**, *61* (4), 1–6.

(137) Dhar, S.; Lippard, S. J. Mitaplatin, a Potent Fusion of Cisplatin and the Orphan Drug Dichloroacetate. *Proc. Natl. Acad. Sci. U S A.* **2009**, *106* (52), 22199–22204.

(138) Saber, M. M.; Al-mahallawi, A. M.; Nassar, N. N.; Stork, B.; Shouman, S. A. Targeting Colorectal Cancer Cell Metabolism through Development of Cisplatin and Metformin Nano-Cubosomes. *BMC Cancer* **2018**, *18* (1), 1–11.

(139) Pillozzi, S.; D'Amico, M.; Bartoli, G.; Gasparoli, L.; Petroni, G.; Crociani, O.; Marzo, T.; Guerriero, A.; Messori, L.; Severi, M.; Udisti, R.; Wulff, H.; Chandy, K. G.; Becchetti, A.; Arcangeli, A. The Combined Activation of K Ca 3.1 and Inhibition of K v 11.1/HERG1 Currents Contribute to Overcome Cisplatin Resistance in Colorectal Cancer Cells. *Br. J. Cancer.* **2018**, *118* (2), 200–212.

(140) Cardoso, C. R.; Lima, M. V. S.; Cheleski, J.; Peterson, E. J.; Venâncio, T.; Farrell, N. P.; Carlos, R. M. Luminescent Ruthenium Complexes for Theranostic Applications. *J. Med. Chem.* **2014**, *57* (11), 4906–4915.

(141) Mokhtari, R. B.; Homayouni, T. S.; Baluch, N.; Morgatskaya, E.; Kumar, S.; Das, B.; Yeger, H. Combination Therapy in Combating Cancer Systematic Review: Combination Therapy in Combating Cancer. *Oncotarget* **2017**, *8* (23), 38022–38043.

(142) Goulooze, S. C.; Cohen, A. F.; Rissmann, R. Olaparib. *Br. J. Clin. Pharmacol.* **2016**, *81* (1), 171–173.

(143) Yusoh, N. A.; Ahmad, H.; Gill, M. R. Combining PARP Inhibition with Platinum, Ruthenium or Gold Complexes for Cancer Therapy. *ChemMedChem* **2020**, *15* (22), 2121–2135.

(144) Mendes, F.; Groessl, M.; Nazarov, A. A.; Tsybin, Y. O.; Sava, G.; Santos, I.; Dyson, P. J.; Casini, A. Metal-Based Inhibition of Poly(ADP-Ribose) Polymerase-the Guardian Angel of DNA. *J. Med. Chem.* **2011**, *54* (7), 2196–2206.

(145) Mares, A. G.; Pacassoni, G.; Marti, J. S.; Pujals, S.; Albertazzi, L. Formulation of Tunable Size PLGA-PEG Nanoparticles for Drug Delivery Using Microfluidic Technology. *PLoS One* **2021**, *16* (6), 1–18.

(146) Gagliardi, A.; Giuliano, E.; Venkateswararao, E.; Fresta, M.; Bulotta, S.; Awasthi, V.; Cosco, D. Biodegradable Polymeric Nanoparticles for Drug Delivery to Solid Tumors. *Front. Pharmacol.* **2021**, *12*, 1–24.

(147) Begines, B.; Ortiz, T.; Pérez-Aranda, M.; Martínez, G.; Merinero, M.; Argüelles-Arias, F.; Alcudia, A. Polymeric Nanoparticles for Drug Delivery: Recent Developments and Future Prospects. *Nanomaterials* **2020**, *10* (7), 1–41.

(148) Ghitman, J.; Biru, E. I.; Stan, R.; Iovu, H. Review of Hybrid PLGA Nanoparticles: Future of Smart Drug Delivery and Theranostics Medicine. *Mater. Des.* **2020**, *193*, 1–20.

(149) Luís, A. L.; Rodrigues, J. M.; Geuna, S.; Amado, S.; Shirosaki, Y.; Lee, J. M.; Fregnan, F.; Lopes, M. A.; Veloso, A. P.; Ferreira, A. J.; Santos, J. D.; Armada-Da-Silva, P. A. S.; Varejão, A. S. P.; Maurício, A. C. Use of PLGA 90:10 Scaffolds Enriched with in Vitro-Differentiated Neural Cells for Repairing Rat Sciatic Nerve Defects. *Tissue. Eng. Part. A.* **2008**, *14* (6), 979–993.

(150) Duwa, R.; Pokhrel, R. H.; Banstola, A.; Pandit, M.; Shrestha, P.; Jeong, J. H.; Chang, J. H.; Yook, S. T-Cell Engaging Poly(Lactic-Co-Glycolic Acid) Nanoparticles as a Modular Platform to Induce a Potent Cytotoxic Immunogenic Response against PD-L1 Overexpressing Cancer. *Biomater.* **2022**, *291*, 1–18.

(151) De Souza Ferreira, J. N.; Vasconcelos, V. V. V.; Figueiredo, B. S.; Alves, D. P.; de Abreu, A. L. L. V.; de Souza, P. P.; Costa, D. L. N.; da Silva, A. R. PLGA Nanoparticles for Treatment of Cardiovascular Diseases. In *Poly(lactic-co-glycolic acid) (PLGA) Nanoparticles for Drug Delivery*; Elsevier, 2023; pp 267–302.

(152) Guo, X.; Zuo, X.; Zhou, Z.; Gu, Y.; Zheng, H.; Wang, X.; Wang, G.; Xu, C.; Wang, F. An Overview of Their Applications in Respiratory Diseases. *Int. J. Mol. Sci* **2023**, *24*, 1–26.

(153) Lee, C. K.; Atibalentja, D. F.; Yao, L. E.; Park, J.; Kuruvilla, S.; Felsher, D. W. Anti-PD-L1 F(Ab) Conjugated PEG-PLGA Nanoparticle Enhances Immune Checkpoint Therapy. *Nanotheranostics* **2021**, *6* (3), 243–255.

(154) Odeh, F.; Nsairat, H.; Alshaer, W.; Ismail, M. A.; Esawi, E.; Qaqish, B.; Bawab, A. Al; Ismail, S. I. Aptamers Chemistry: Chemical Modifications and Conjugation Strategies. *Molecules.* **2020**, *25* (1), 1–51.

(155) Guo, J.; Gao, X.; Su, L.; Xia, H.; Gu, G.; Pang, Z.; Jiang, X.; Yao, L.; Chen, J.; Chen, H. Aptamer-Functionalized PEG-PLGA Nanoparticles for Enhanced Anti-Glioma Drug Delivery. *Biomaterials* **2011**, *32* (31), 8010–8020.

(156) Romano, S.; Fonseca, N.; Simões, S.; Gonçalves, J.; Moreira, J. N. Nucleolin-Based Targeting Strategies for Cancer Therapy: From Targeted Drug Delivery to Cytotoxic Ligands. *Drug. Discov. Today.* **2019**, *24* (10), 1985–2001.

(157) Li, F.; Lu, J.; Liu, J.; Liang, C.; Wang, M.; Wang, L.; Li, D.; Yao, H.; Zhang, Q.; Wen, J.; Zhang, Z. K.; Li, J.; Lv, Q.; He, X.; Guo, B.; Guan, D.; Yu, Y.; Dang, L.; Wu, X.; Li, Y.; Chen, G.; Jiang, F.; Sun, S.; Zhang, B. T.; Lu, A.; Zhang, G. A Water-Soluble Nucleolin Aptamer-Paclitaxel Conjugate for Tumor-Specific Targeting in Ovarian Cancer. *Nat. Commun.* **2017**, *8* (1), 1–14.

(158) Cheng, J.; Teply, B. A.; Sherifi, I.; Sung, J.; Luther, G.; Gu, F. X.; Levy-Nissenbaum, E.; Radovic-Moreno, A. F.; Langer, R.; Farokhzad, O. C. Formulation of Functionalized PLGA-PEG Nanoparticles for in Vivo Targeted Drug Delivery. *Biomater.* **2007**, *28* (5), 869–876.

(159) Shahrad, S.; Rajabi, M.; Javadi, H.; Karimi Zarchi, A. A.; Darvishi, M. H. Targeting Lung Cancer Cells with MUC1 Aptamer-Functionalized PLA-PEG Nanocarriers. *Sci. Rep.* **2022**, *12* (1), 1–11.

(160) Manoochehri, S.; Darvishi, B.; Kamalinia, G.; Amini, M.; Fallah, M.; Ostad, S. N.; Atyabi, F.; Dinarvand, R. Surface Modification of PLGA Nanoparticles via Human Serum Albumin Conjugation for Controlled Delivery of Docetaxel. *DARU J. Pharm. Sci.* **2013**, *21* (1), 1–10.

(161) Betancourt, T.; Byrne, J. D.; Sunaryo, N.; Crowder, S. W.; Kadapakkam, M.; Patel, S.; Casciato, S.; Brannon-Peppas, L. PEGylation Strategies for Active Targeting of PLA/PLGA Nanoparticles. *J. Biomed. Mater. Res.* **2009**, *91* (1), 263–276.

(162) Jusu, S. M.; Obayemi, J. D.; Salifu, A. A.; Nwazojie, C. C.; Uzonwanne, V.; Odusanya, O. S.; Soboyejo, W. O. Drug-Encapsulated Blend of PLGA-PEG Microspheres: In Vitro and in Vivo Study of the Effects of Localized/Targeted Drug Delivery on the Treatment of Triple-Negative Breast Cancer. *Sci. Rep.* **2020**, *10* (1), 1–23.

(163) Gu, F.; Zhang, L.; Teply, B. A.; Mann, N.; Wang, A.; Radovic-Moreno, A. F.; Langer, R.; Farokhzad, O. C. Precise Engineering of Targeted Nanoparticles by Using Self-Assembled Biointegrated Block Copolymers. *PNAS. USA.* **2008**, *105* (7), 2586–2591.

(164) Dutta, D.; Chakraborty, A.; Mukherjee, B.; Gupta, S. Aptamer-Conjugated Apigenin Nanoparticles to Target Colorectal Carcinoma: A Promising Safe Alternative of Colorectal Cancer Chemotherapy. *ACS Appl. Bio Mater.* **2018**, *1* (5), 1538–1556.

(165) Betancourt, T.; Byrne, J. D.; Sunaryo, N.; Crowder, S. W.; Kadapakkam, M.; Patel, S.; Casciato, S.; Brannon-Peppas, L. PEGylation Strategies for Active Targeting of PLA/PLGA Nanoparticles. *J. Biomed. Mater. Res. A* **2009**, *91* (1), 263–276.

(166) Fischer, M. J. E. Amine Coupling through EDC/NHS: A Practical Approach. In *Methods in molecular biology (Clifton, N.J.)*; 2010; Vol. 627, pp 55–73.

(167) Danaei, M.; Dehghankhold, M.; Ataei, S.; Hasanzadeh Davarani, F.; Javanmard, R.; Dokhani, A.; Khorasani, S.; Mozafari, M. R. Impact of Particle Size and Polydispersity Index on the Clinical Applications of Lipidic Nanocarrier Systems. *Pharmaceutics* **2018**, *10* (2), 1–17.

(168) Clogston, J. D.; Patri, A. K. Zeta Potential Measurement. In *Methods in Molecular Biology*; Humana Press Inc., 2011; Vol. 697, pp 63–70.

(169) Augustine, R.; Hasan, A.; Primavera, R.; Wilson, R. J.; Thakor, A. S.; Kevadiya, B. D. Cellular Uptake and Retention of Nanoparticles: Insights on Particle Properties and Interaction with Cellular Components. *Mater. Today Commun.* **2020**, *25*, 1–19.

(170) Hines, D. J.; Kaplan, D. L. Poly (Lactic-Co-Glycolic Acid) Controlled Release Systems: Experimental and Modeling Insights. *Crit. Rev. Ther. Drug. Carrier. Syst.* **2013**, *30* (3), 157–276.

(171) Elena de Souza, L.; Eckenstaler, R.; Syrowatka, F.; Beck-Broichsitter, M.; Benndorf, R. A.; Mäder, K. Has PEG-PLGA Advantages for the Delivery of Hydrophobic Drugs? Risperidone as an Example. *J. Drug Deliv. Technol.* **2021**, *61*, 1–9.

Appendix A. Supporting Information for Chapter 2

NMR and MS Spectra

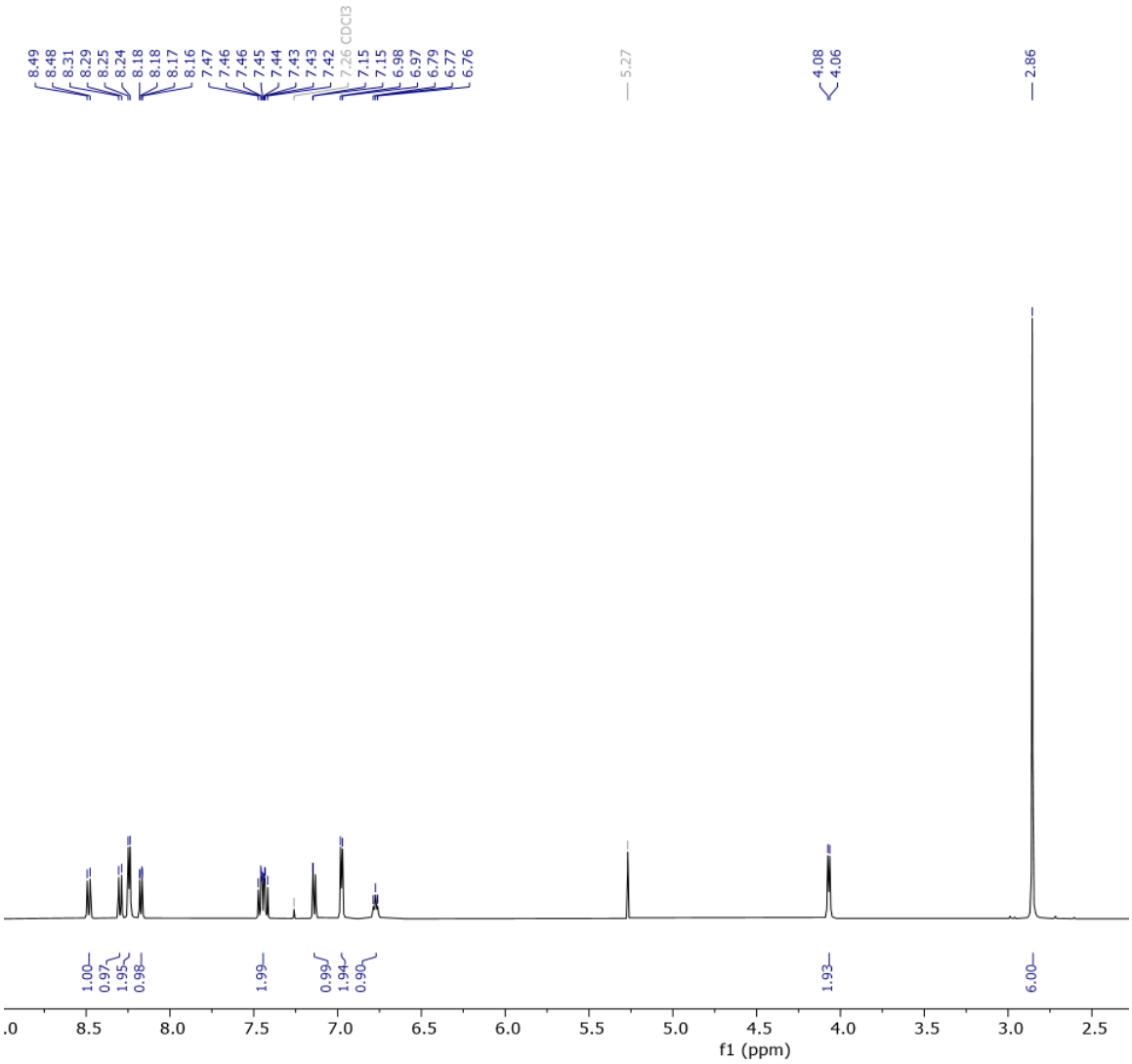

Figure A.1. **^{1}H NMR Spectrum of 2-3** (500 MHz, $CDCl_3$) δ 8.48 (d, J = 8.6 Hz, 1H), 8.30 (d, J = 8.7 Hz, 2H), 8.24 (d, J = 6.1 Hz, 2H), 8.20 – 8.13 (m, 1H), 7.44 (dt, J = 11.9, 8.0 Hz, 4H), 7.14 (d, J = 7.5 Hz, 2H), 6.98 (d, J = 6.2 Hz, 2H), 6.77 (t, J = 6.5 Hz, 2H), 4.07 (d, J = 6.0 Hz, 3H), 2.86 (s, 11H).

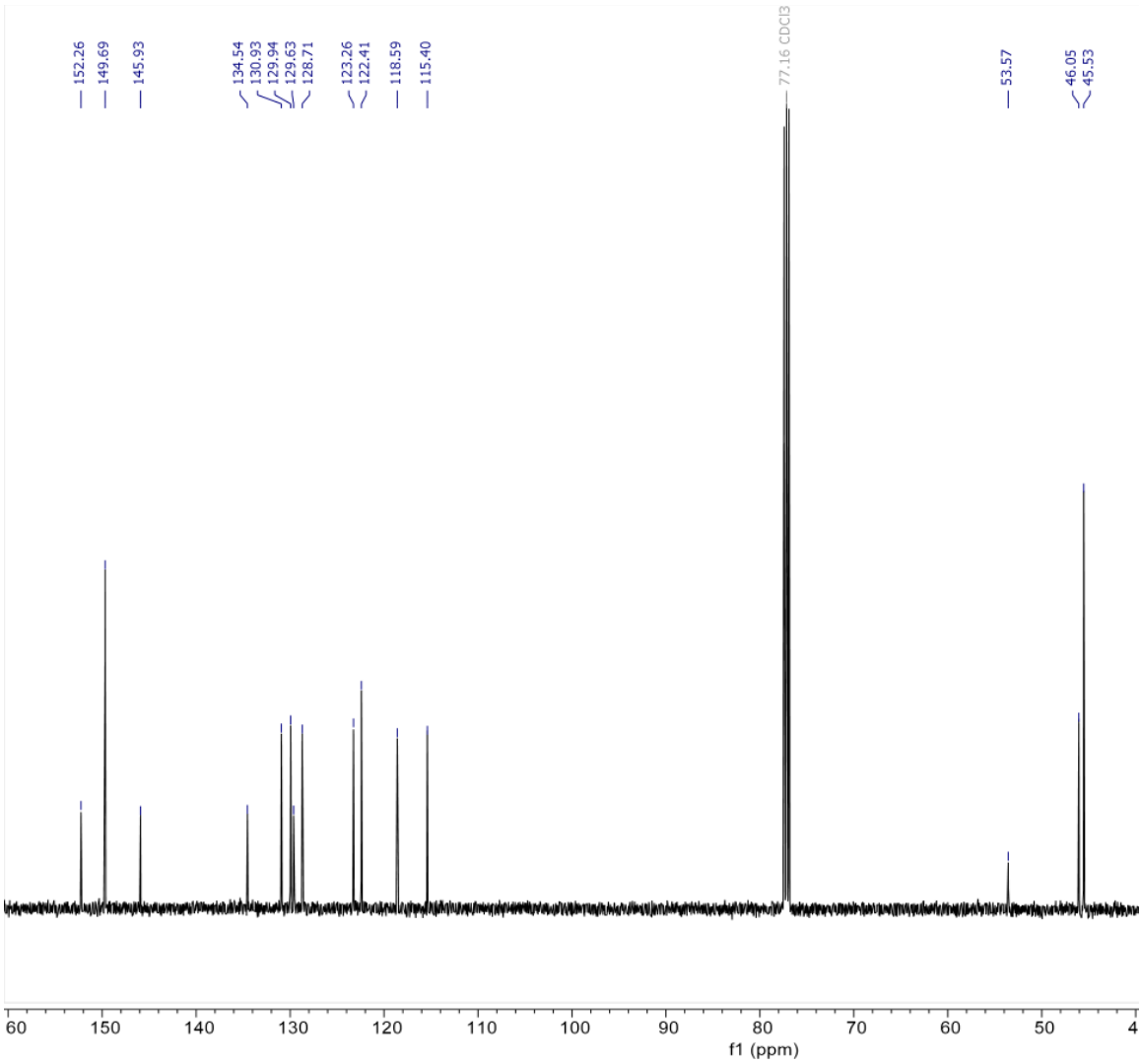

Figure A.2. **^{13}C NMR Spectrum of 2-3.** ^{13}C NMR (126 MHz, $CDCl_3$) δ 152.26, 149.69, 145.93, 134.54, 130.93, 129.94, 129.63, 128.71, 123.26, 122.41, 118.59, 115.40, 53.57, 46.05, 45.53.

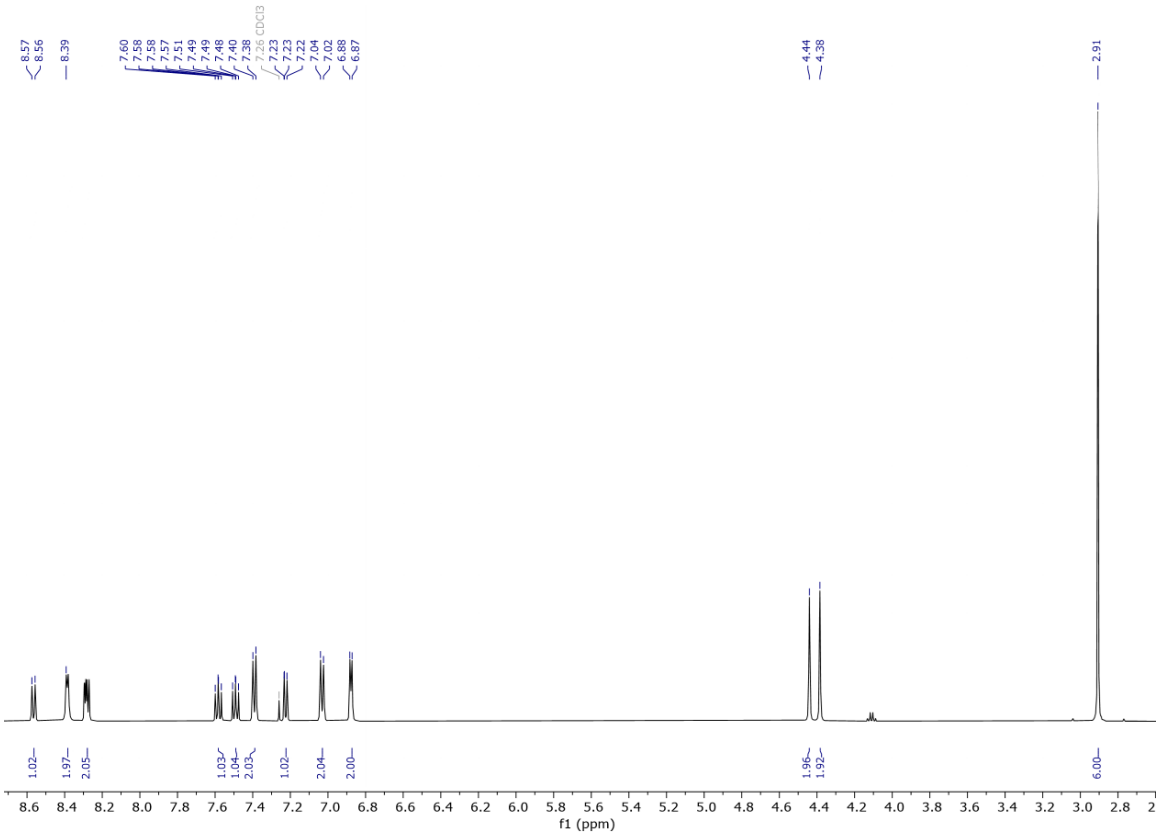

Figure A.3. **^{1}H NMR Spectrum of 2-4** (500 MHz, $CDCl_3$): δ 8.58 (d, J = 8.5 Hz, 1H), 8.42 – 8.38 (m, 2H), 8.29 (t, J = 8.0 Hz, 2H), 7.59 (dd, J = 8.7, 7.6 Hz, 1H), 7.50 (dd, J = 8.5, 7.3 Hz, 1H), 7.40 (d, J = 8.0 Hz, 2H), 7.24 (d, J = 7.6 Hz, 1H), 7.04 (d, J = 8.1 Hz, 2H), 6.89 (d, J = 6.1 Hz, 2H), 4.45 (s, 2H), 4.39 (s, 2H), 2.92 (s, 6H).

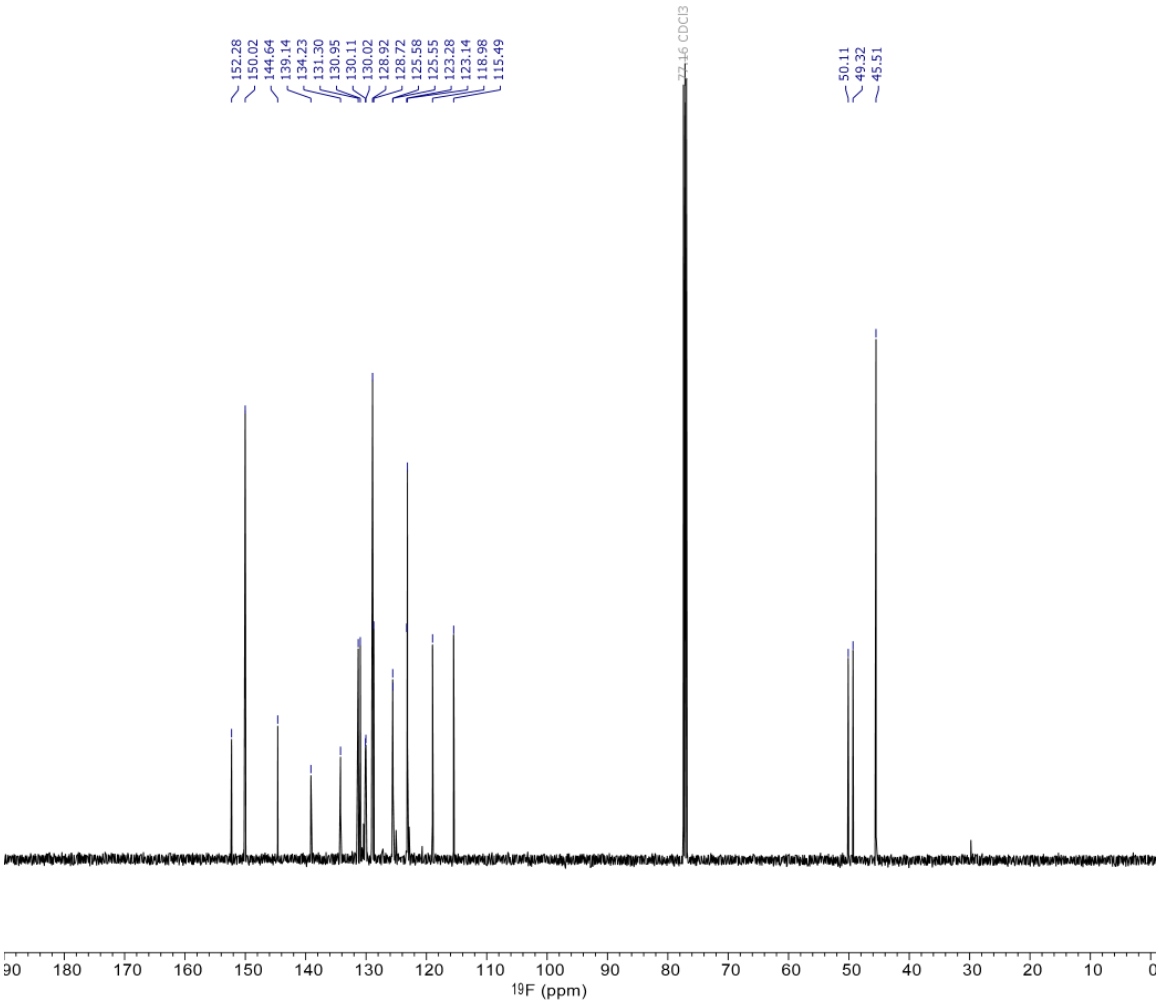

Figure A.4. **^{13}C NMR Spectrum of 2-4** (126 MHz, $CDCl_3$): δ 152.28, 150.02, 144.64, 139.14, 134.23, 131.30, 130.95, 130.11, 130.02, 128.92, 128.72, 125.58, 125.55, 123.28, 123.14, 118.98, 115.49, 50.11, 49.32, 45.51.

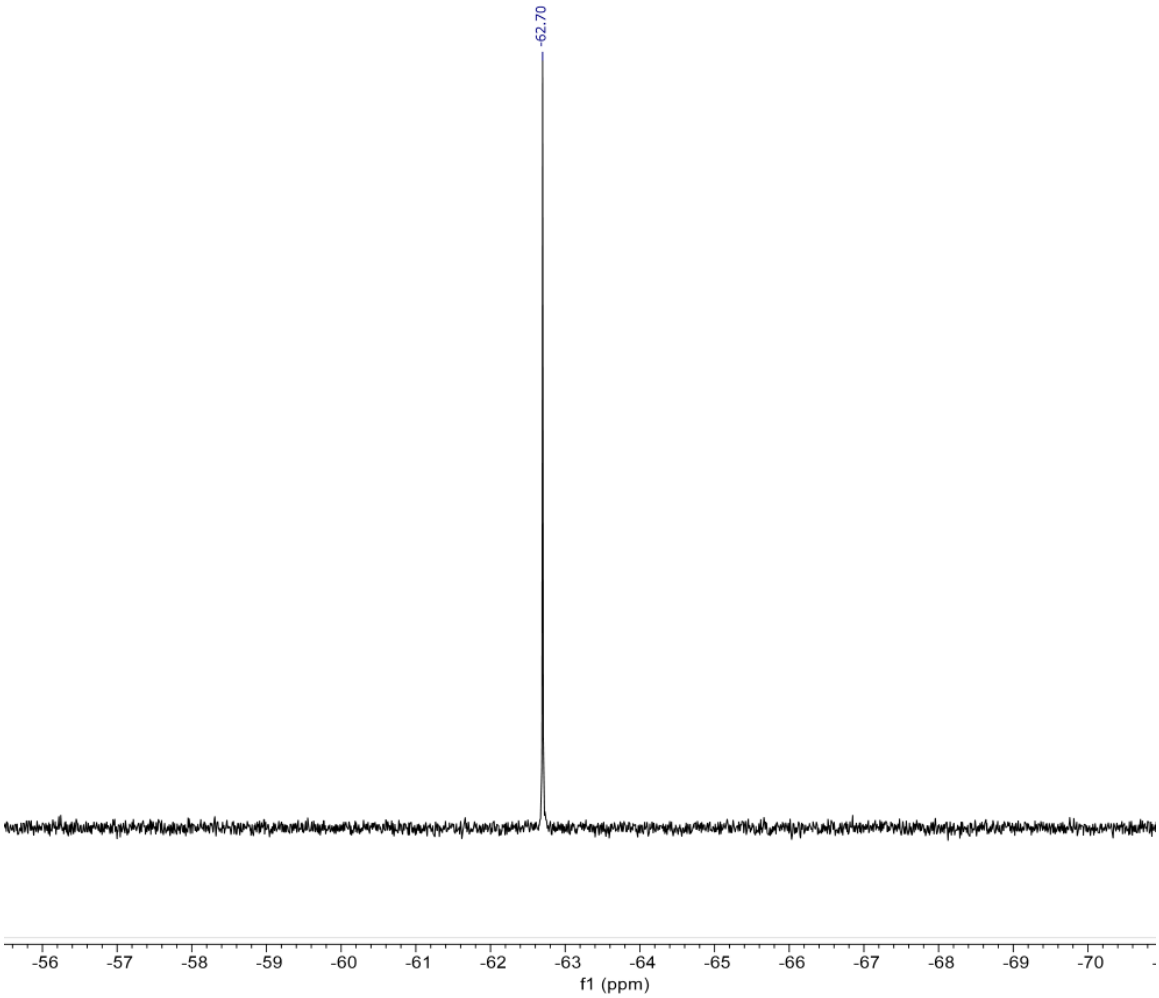

Figure A.5. **^{19}F NMR Spectrum of NMR of 2-4** (376 MHz, $CDCl_3$): δ -62.70.

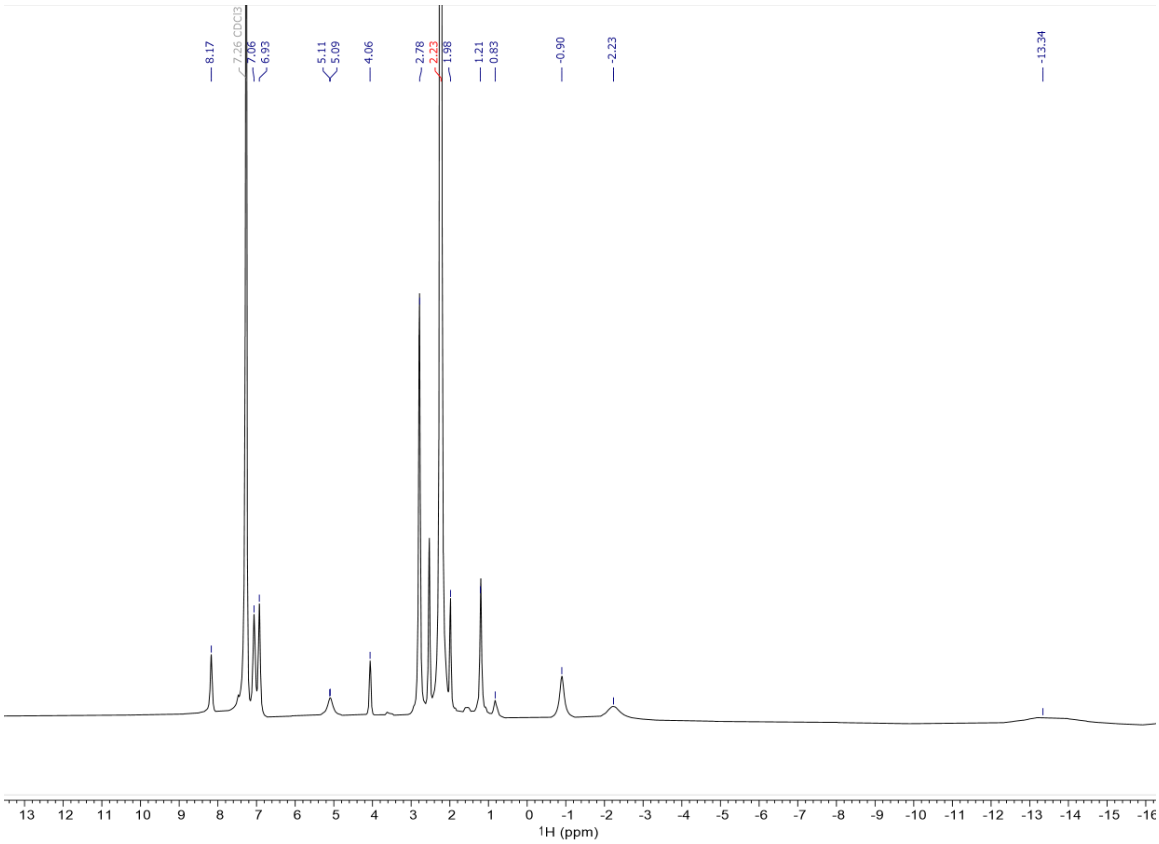

Figure A.6. **^{1}H NMR Spectrum of 2-5** (500 MHz, $CDCl_3$): δ 8.17, 7.06, 6.93, 5.11, 5.09, 4.06, 2.78, 2.23, 1.98, 1.21, 0.83, -0.90, -2.23, -13.34.

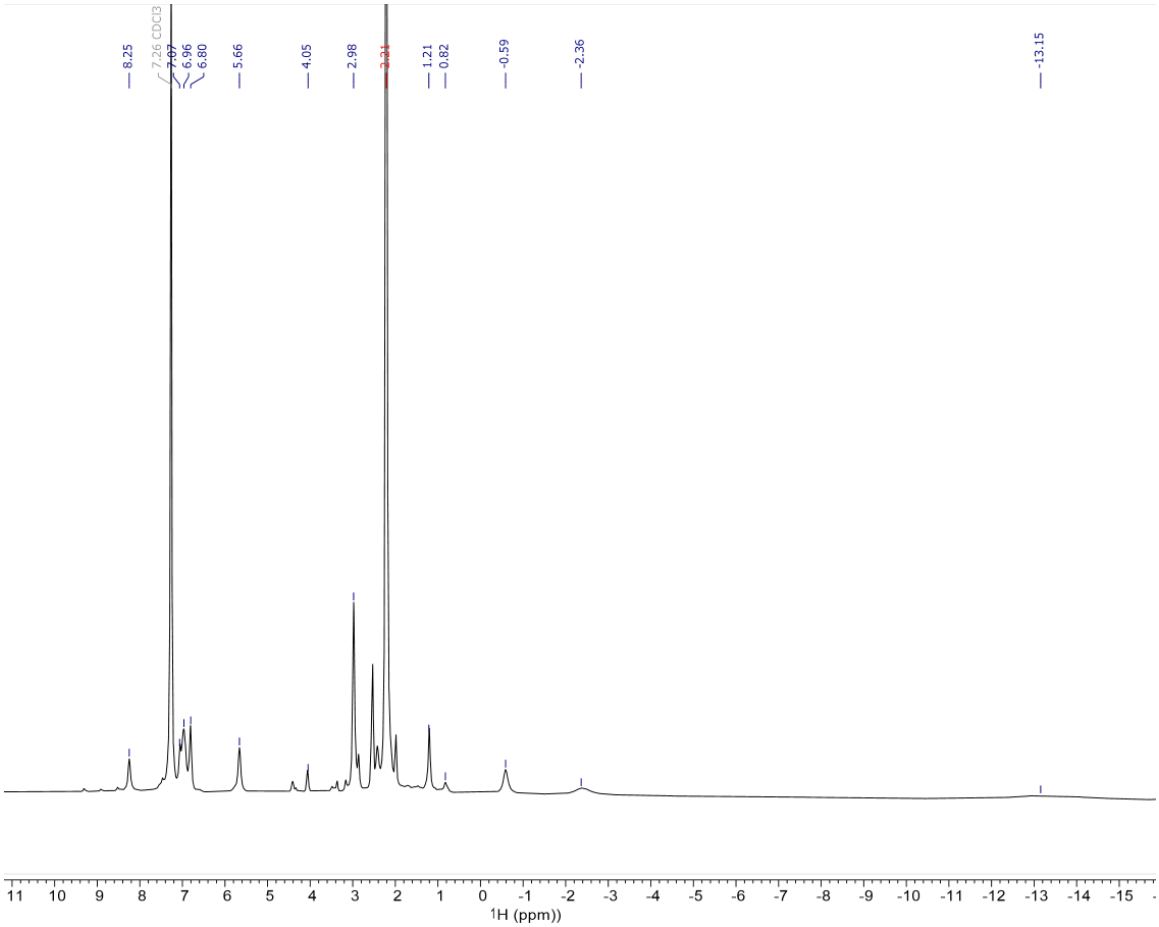

Figure A.7. **^{1}H NMR Spectrum of 2-6** (500 MHz, $CDCl_3$) δ 8.25, 7.07, 6.96, 6.80, 5.66, 4.05, 2.98, 2.21, 1.21, 0.82, -0.59, -2.36, -13.15.

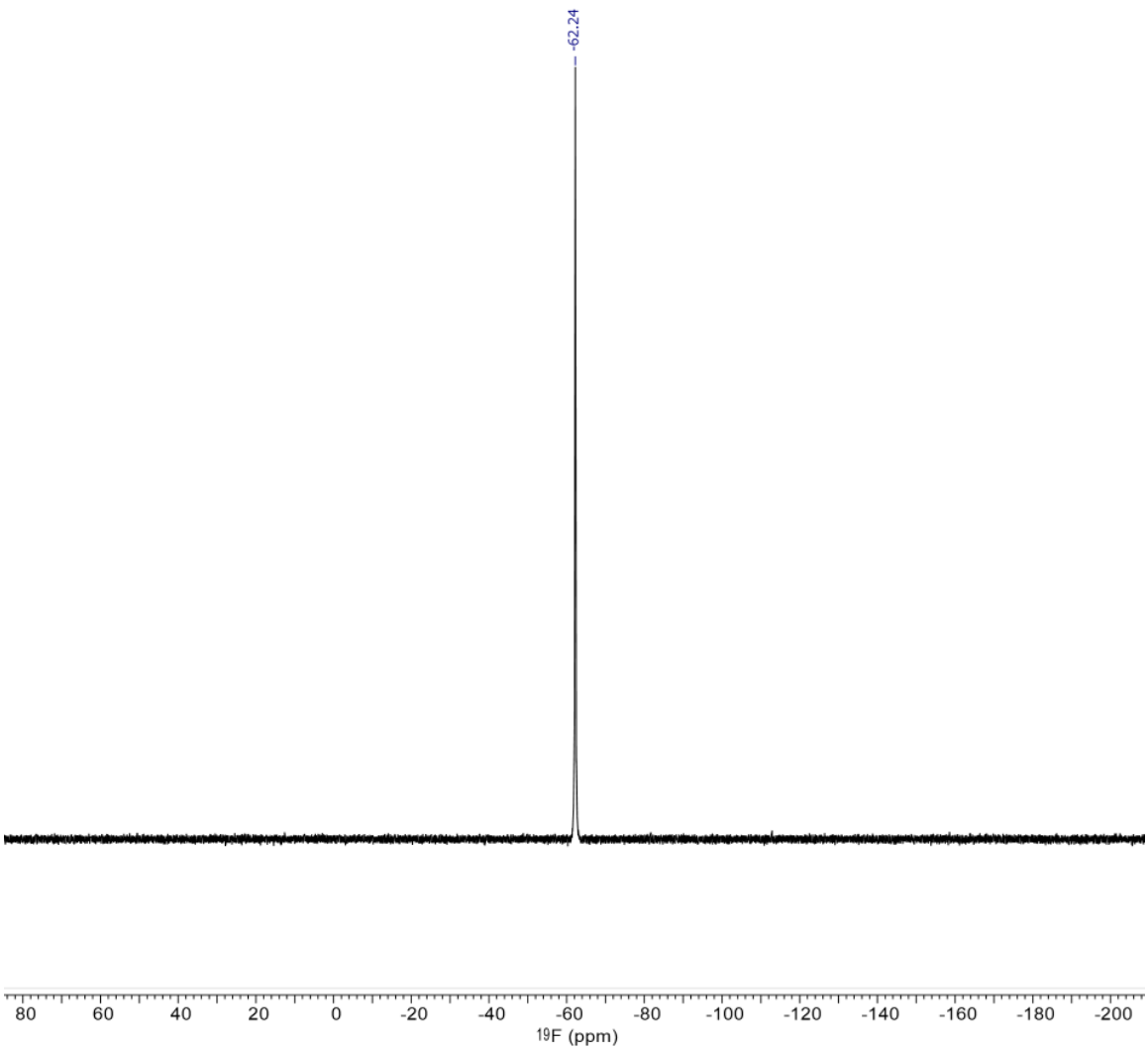

Figure A.8. **^{19}F NMR Spectrum of NMR of 2-6** (376 MHz, $CDCl_3$): δ -62.24.

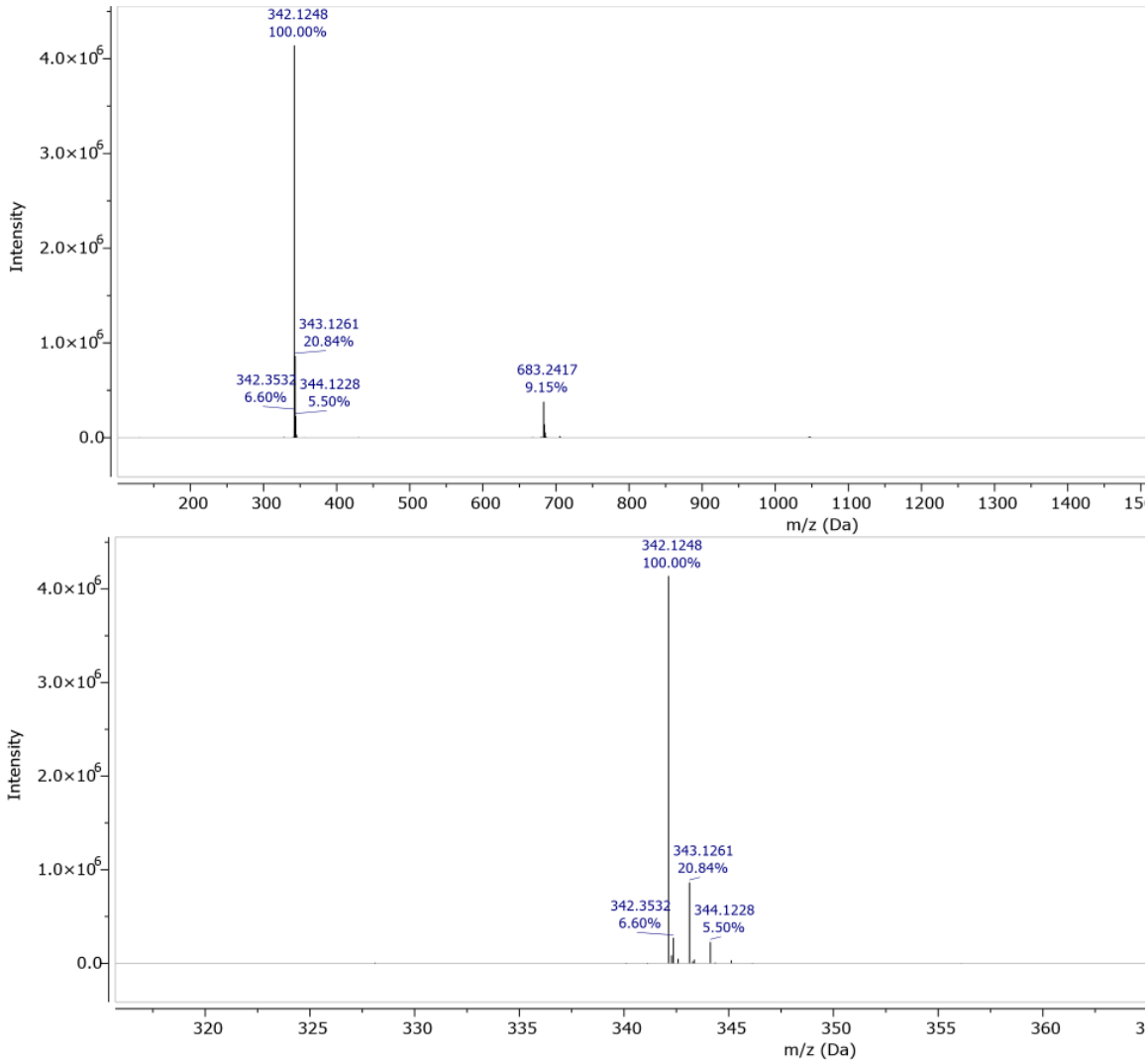

Figure A.9. MS Spectrum of 2-3 using an ESI-ToF in positive mode. Observed $[M+H]^+$: 342.123 *m/z*.Calculated $[M+H]^+$: 342.127 *m/z*.

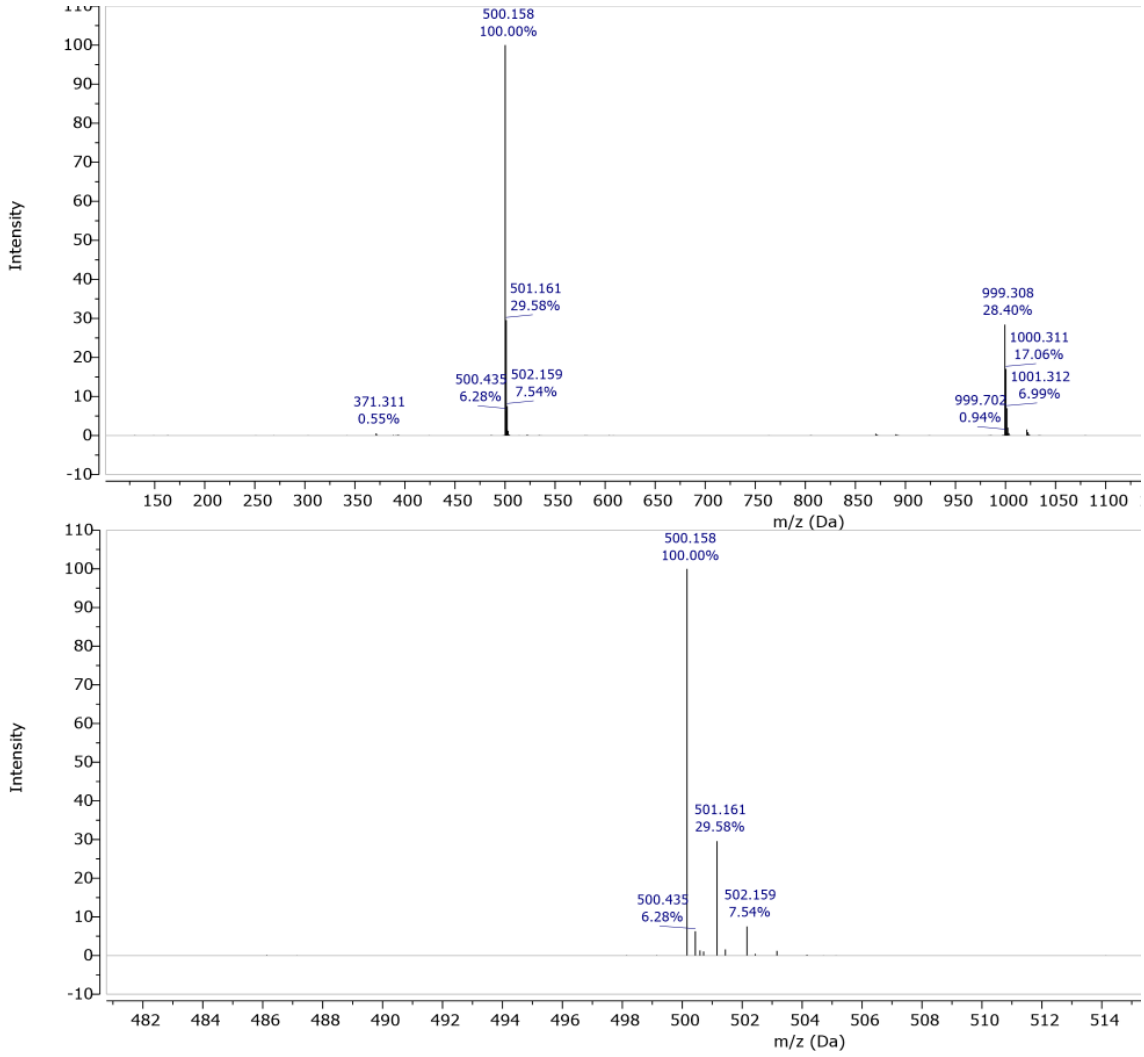

Figure A.10. MS Spectrum of 2-4 using an ESI-ToF in positive mode. Observed [M+H]+: 500.158 m/z.Calculated [M+H]+: 500.161 m/z.

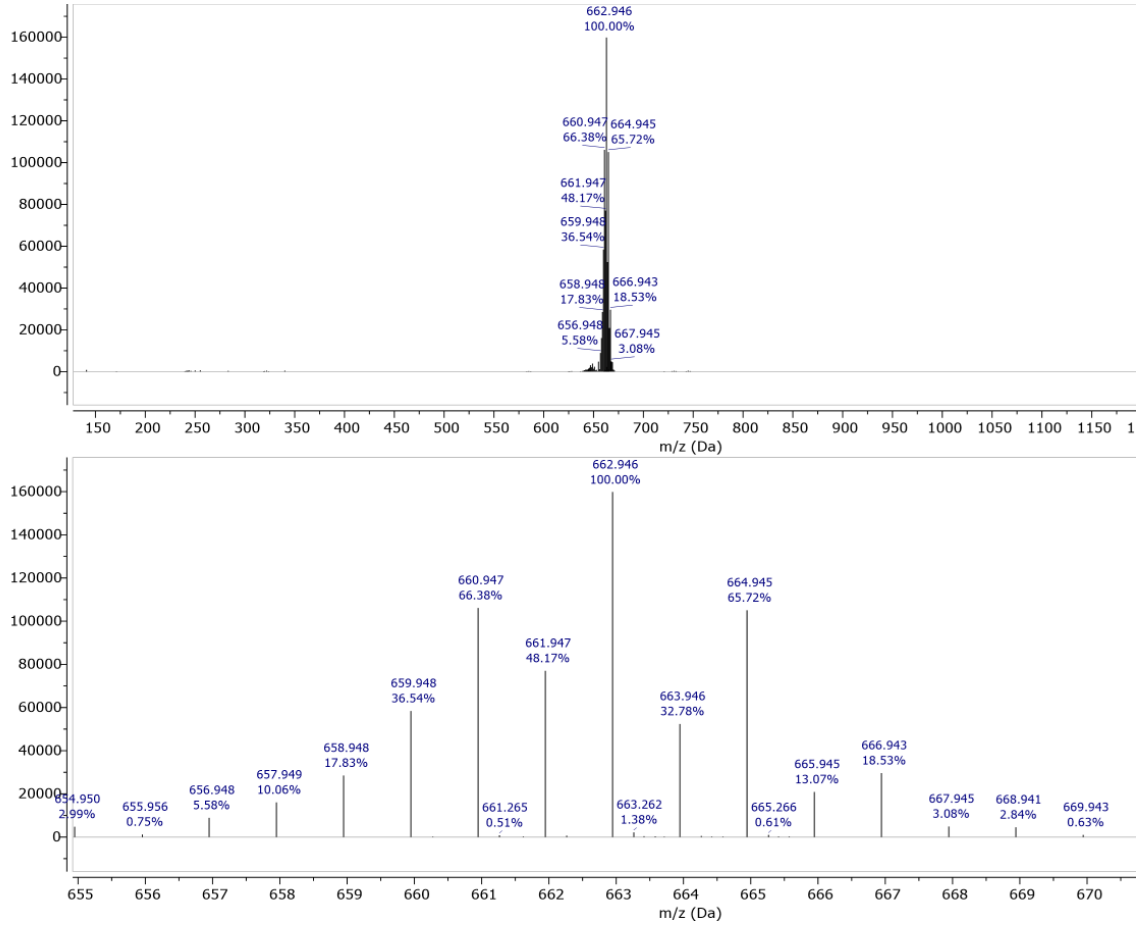

Figure A.11. MS Spectrum of 2-5 using an ESI-ToF in negative mode. Observed $[M]^-$: 662.946 m/z.Calculated $[M]^-$: 662.912 m/z.

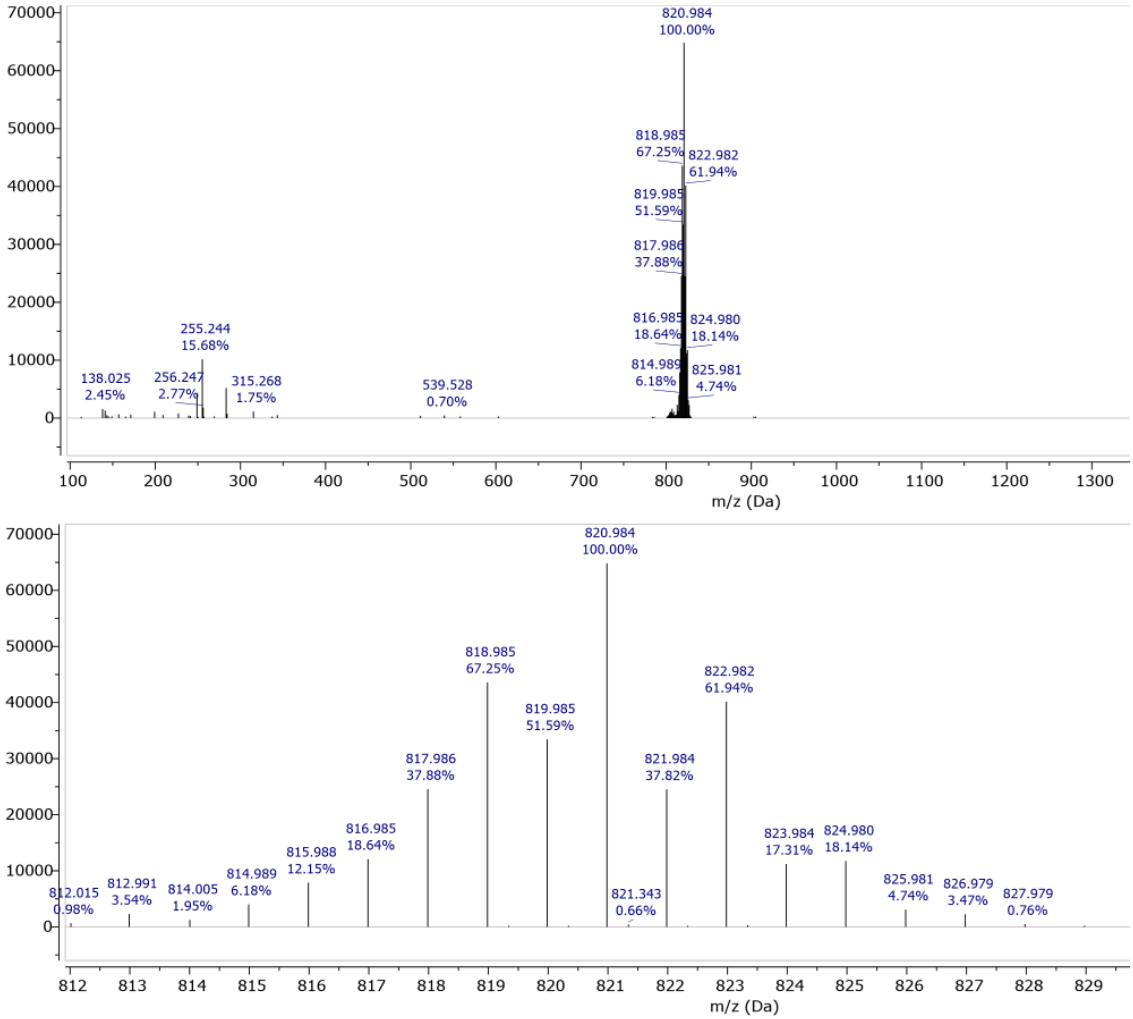

Figure A.12. MS Spectrum of 2-6 using an ESI-ToF in negative mode. Observed $[M]^-$: 820.984 m/z.Calculated $[M]^-$: 820.945 m/z.

Ligand-Exchange NMR

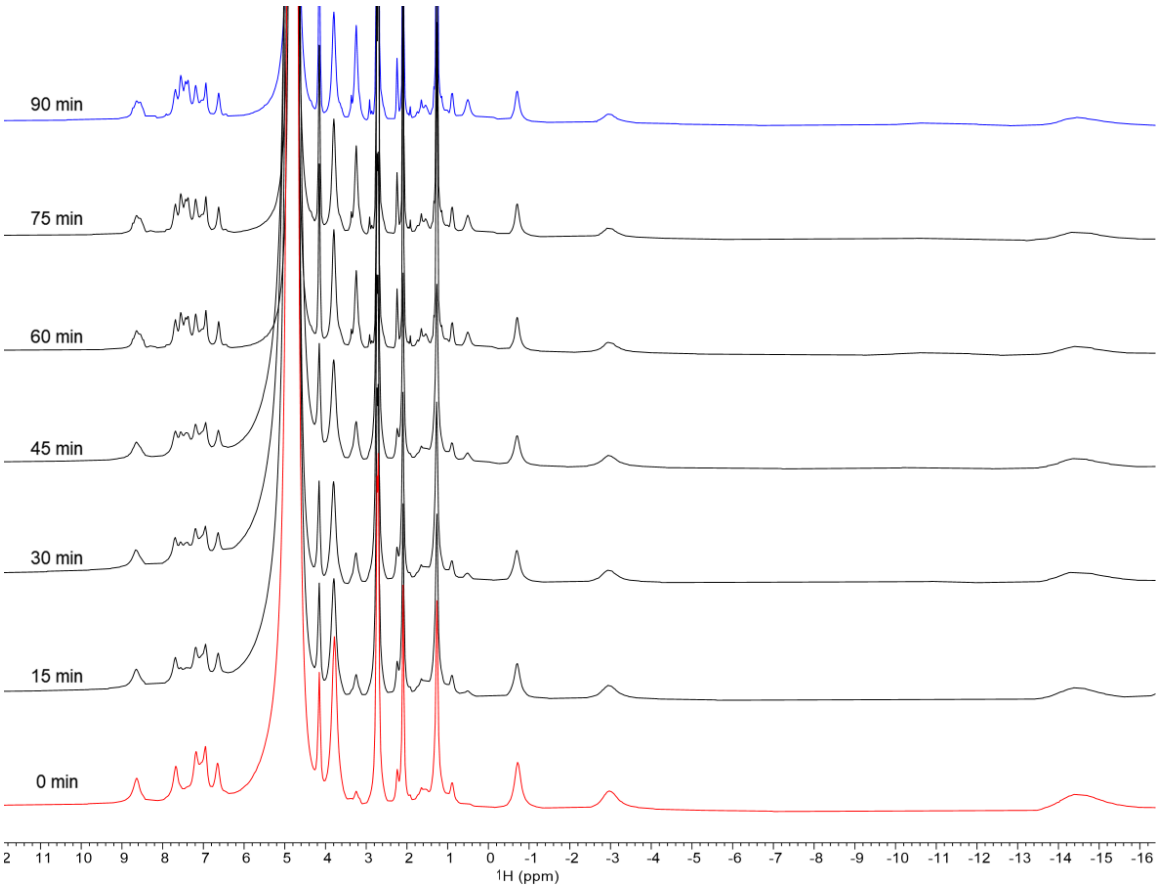

Figure A.13. Time-based ^{1}H NMR scans of 2-5 in 1x PBS (pH 7.4, 134 mM NaCl)

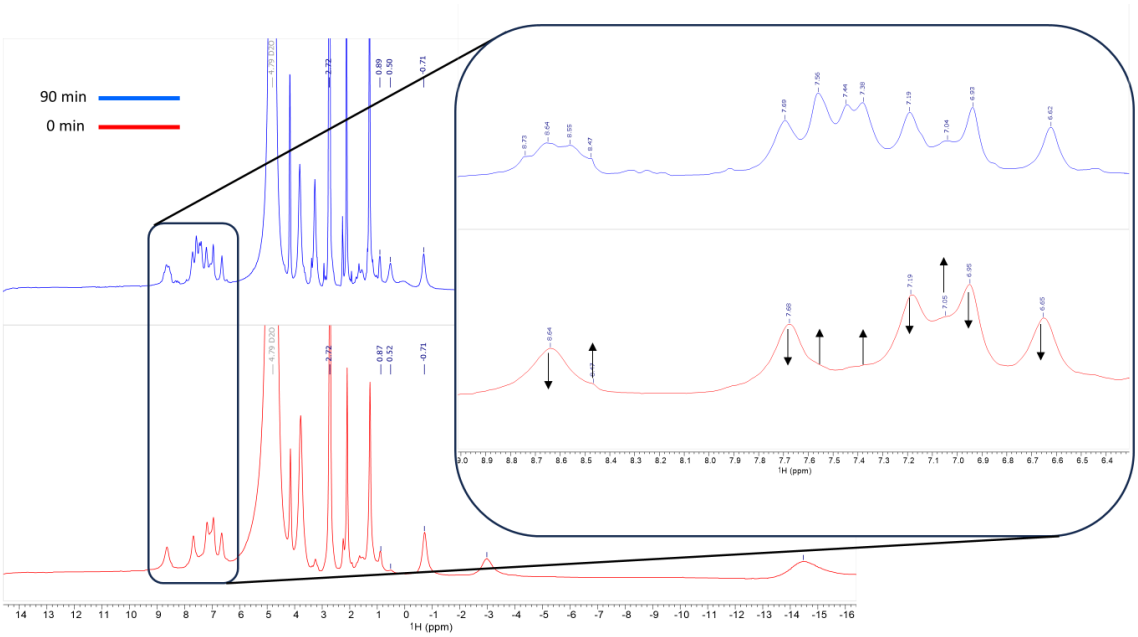

Figure A.14. The diamagnetic region of the ^{1}H NMR spectra of 2-5 in 1x PBS (pH 7.4, 134 mM NaCl) at 0 min, and 90 min.

Synergy Assay: Combination Index Calculation

$$\boldsymbol{Bliss\ Threshold} = \boldsymbol{E_a} + \boldsymbol{E_b} - \boldsymbol{E_{ab}}$$

Where, E_a and E_b are the % effect observed for each drug through monotherapy, and E_{ab} is the % effect observed for therapy using the combination of drugs.

$$\boldsymbol{C.I} = \frac{\boldsymbol{Bliss\ Threshold}}{\boldsymbol{E_{ab}}}$$

If log(CI)<0: synergistic combination

If log(CI)>0: antagonistic combination

Table A.1. Synergy Assay Drug Response Data.

SOC Agent	Combination Response	SOC Response	2-6 Response	Bliss Threshold	Combination Index	Verdict
Paclitaxel	3.83	4.45	3.69	7.97	2.08	Antagonistic
5 F-U	26.33	30.48	3.69	33.04	1.25	Antagonistic
Olaparib	28.85	11.28	3.69	14.55	0.50	Synergistic
Irinotecan	32.69	33.05	3.69	35.51	1.09	Antagonistic
AZD6738	16.26	33.38	3.69	35.84	2.20	Antagonistic
Oxaliplatin	23.10	38.15	3.69	40.43	1.75	Antagonistic

*Response values are reported as % response.

Appendix B. Supporting Information for Chapter 3

ICP-MS Calibration Data

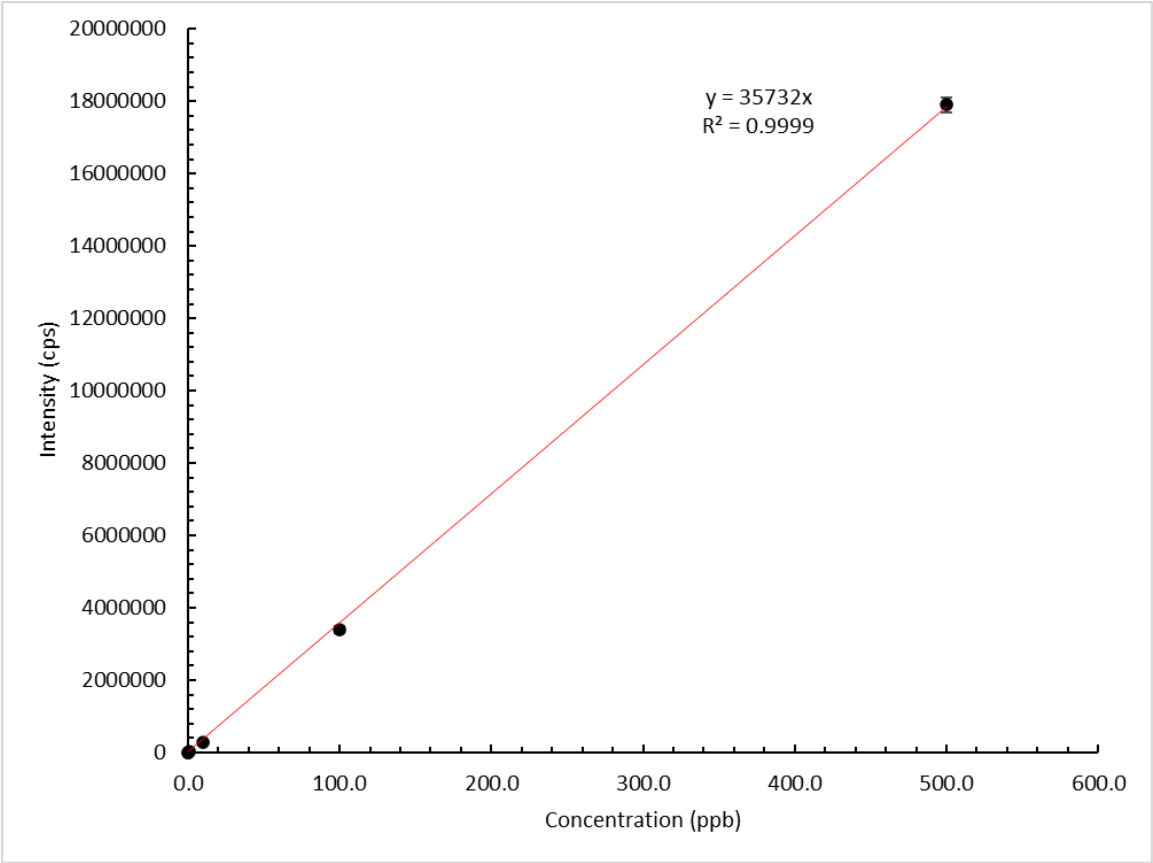

Figure B.1. The ruthenium calibration curve for ICP-MS studies. Data points at [Ru] = 0, 0.1, 1.0, 10.0, 100.0, and 500,0 ppb.

Size Distribution Graphs

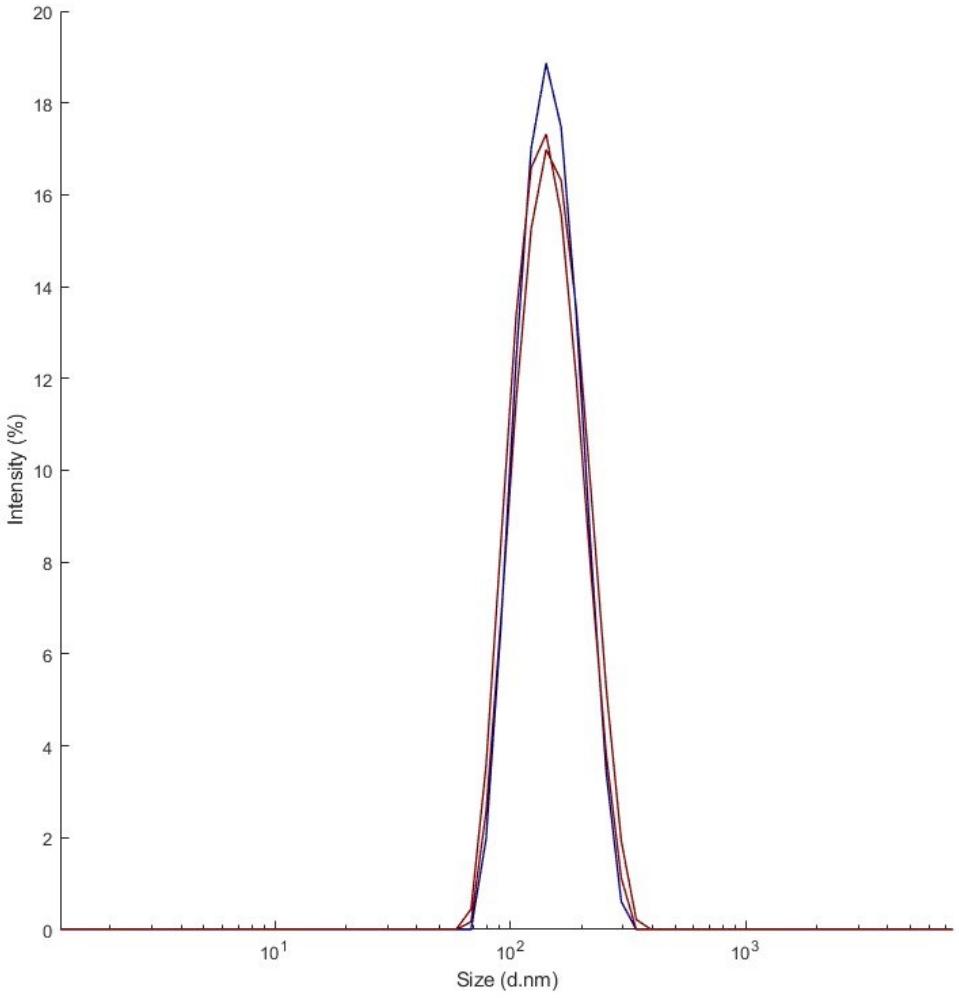

Figure B.2. Size distribution graph for empty non-functionalized PLGA-PEG NPs.

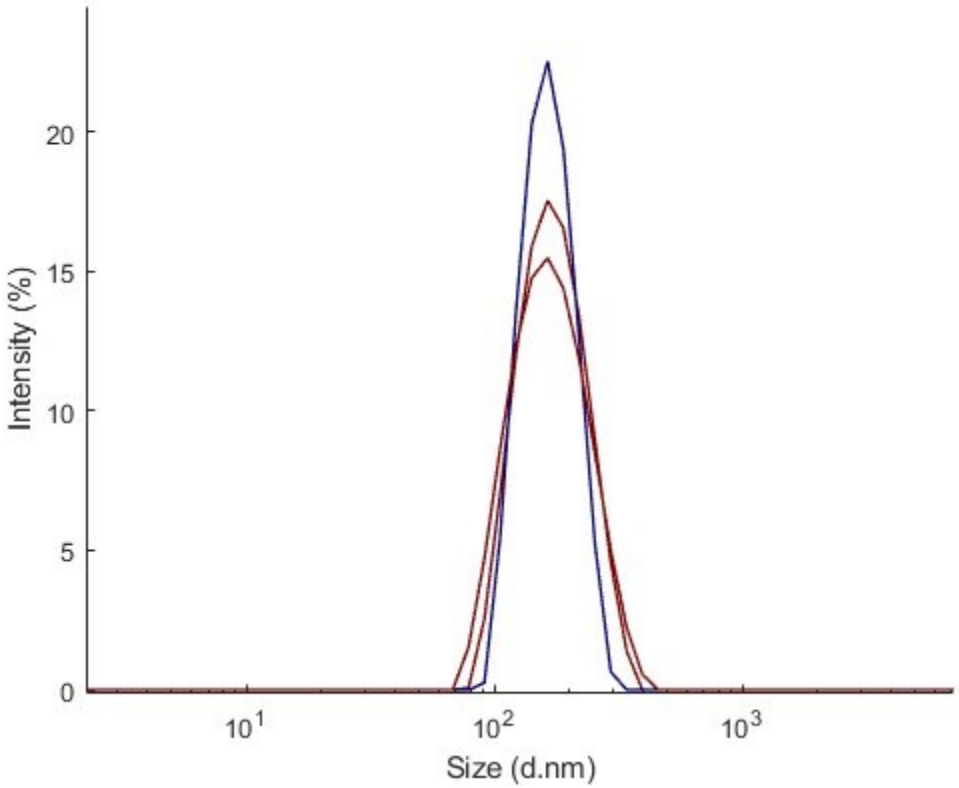

Figure B.3. Size distribution graph for empty AS1411-functionalized PLGA-PEG NPs.

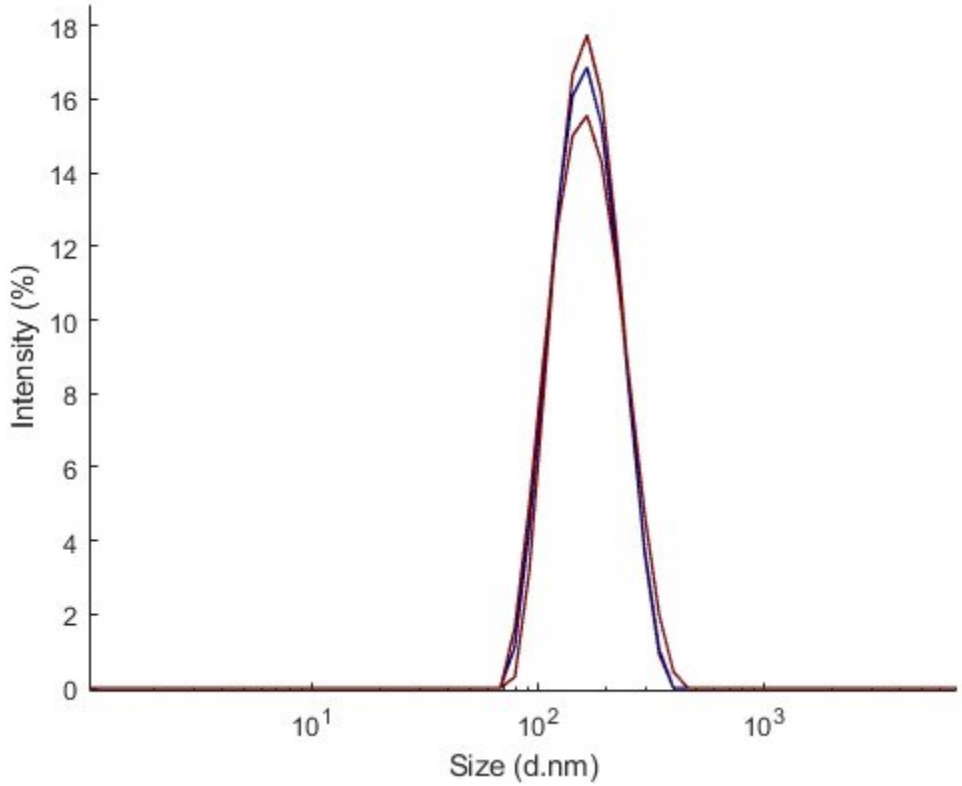

Figure B.4. Size distribution graph for non-functionalized PLGA-PEG NPs containing 2-5.

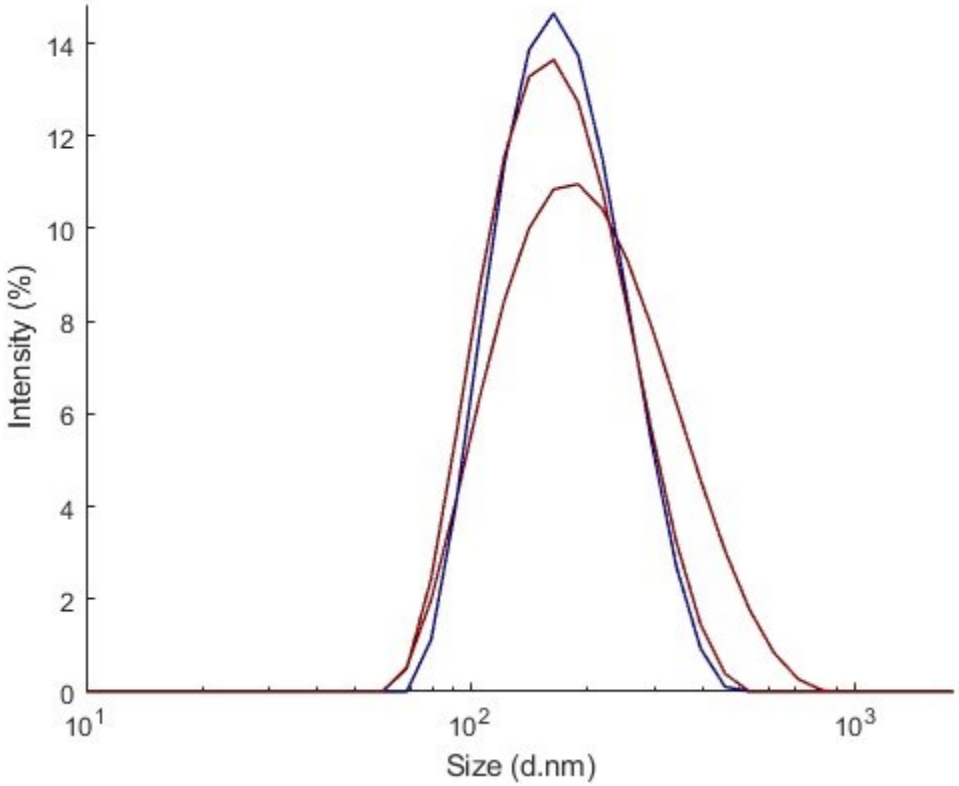

Figure B.5. Size distribution graph for non-functionalized PLGA-PEG NPs containing 2-6.

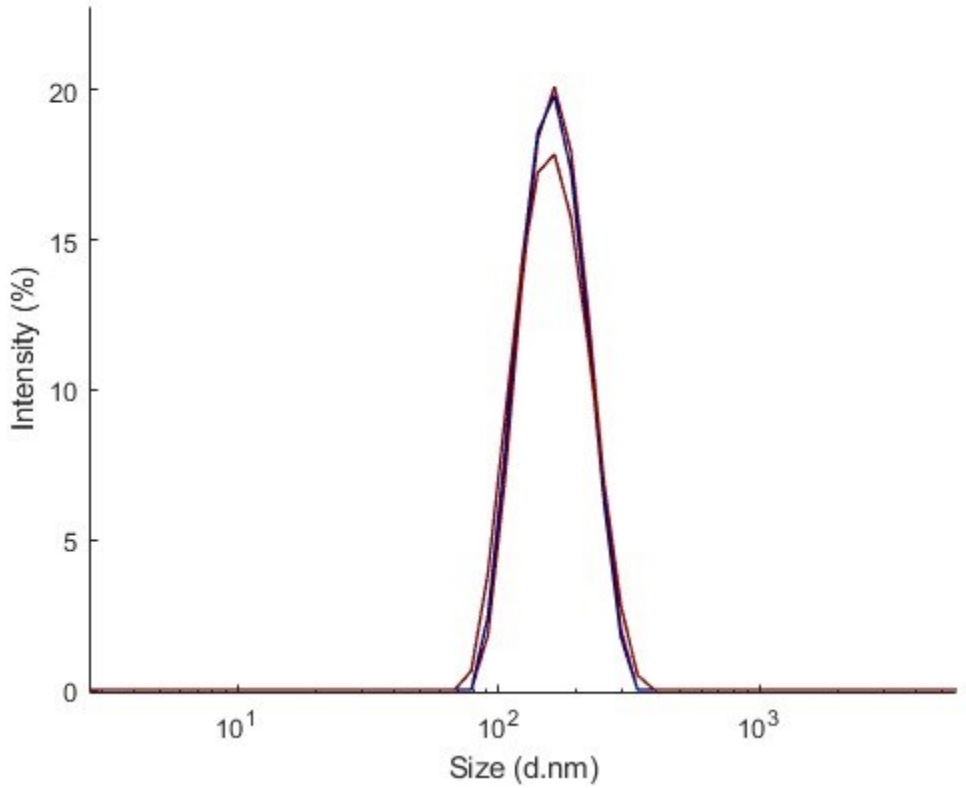

Figure B.6. Size distribution graph for AS1411-functionalized PLGA-PEG NPs containing 2-5.

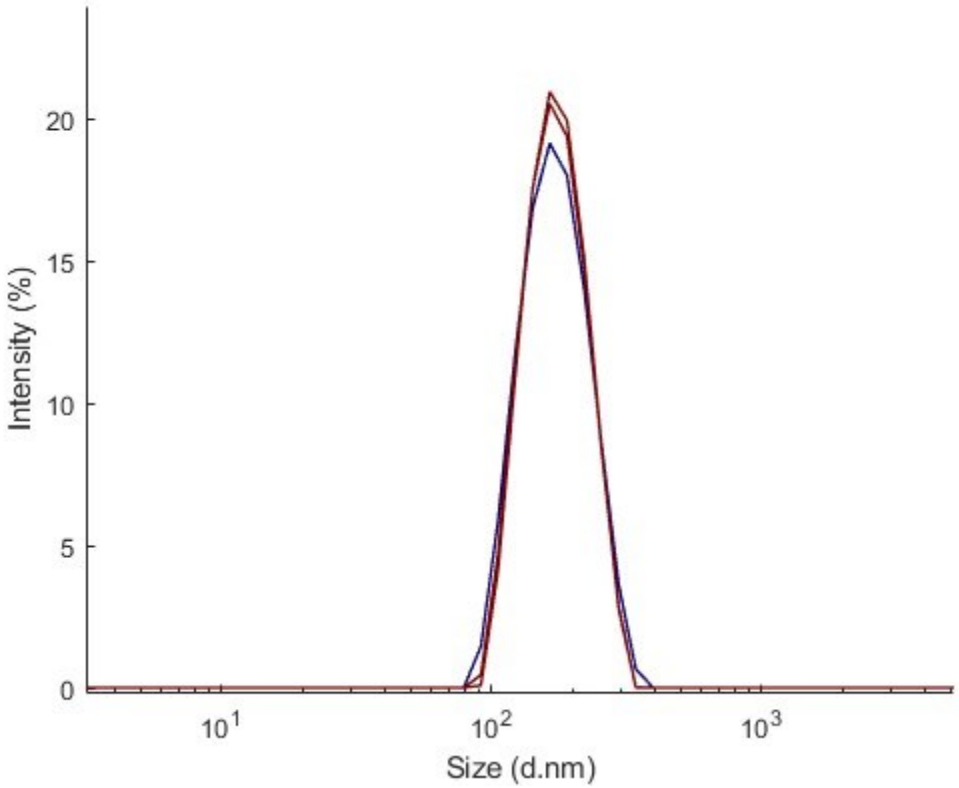

Figure B.7. Size distribution graph for AS1411-functionalized PLGA-PEG NPs containing 2-6.